学位論文

Theoretical study on mechanism of solid-state high-harmonic generation

（固体高次高調波発生のメカニズムに関する理論的研究）

平成２９年１２月博士（理学）申請

東京大学大学院理学系研究科
物理学専攻
池町　拓也

Theoretical study on mechanism of solid-state high-harmonic generation

Takuya Ikemachi

This thesis is submitted in partial fulfillment of the requirements
for the degree of Doctor of Philosophy
in
Department of Physics, Graduate School of Science,
The University of Tokyo

December 2017

Theoretical study on mechanism of solid-state high-harmonic generation

Abstract

The advent of the laser in 1960 has opened a new era of nonlinear optics in the field of optical science. In the nonlinear regime, the optical properties of materials are no longer independent of the field strength. Today, advances in ultrafast intense laser techniques have enabled us to enter a new stage beyond nonlinear optics: strong-field physics, where perturbative treatments of the field are no longer applicable. In particular, high-harmonic generation (HHG) from gas-phase atoms and molecules has been one of the main targets of research for three decades, which has led to successful applications such as attosecond pulse and coherent keV x-ray generations as well as powerful means to observe and manipulate ultrafast electron dynamics. Many features of gas-phase HHG can be intuitively and even quantitatively explained by a semiclassical three-step model. Recently, solid-state materials have emerged as a new playground for strong-field physics. In particular, since its first discovery in 2011, many experimental observations of high-harmonic generation from solid-state materials, or *solid-state high-harmonic generation,* have been reported. The extension of the concepts and methods that have been developed so far in the gas-phase HHG is expected to offer potential scientific and technological opportunities in solids. The application of spectroscopic techniques in gas-phase HHG to solid-state systems may provide new means to probe the electronic structures of insulators and semiconductors. Understanding the electron excitation process under intense electric fields would be critical to future applications in ultrafast optical current control and be important as the initial process of laser material processing. As this field is in its infancy, the radiation mechanism is still under intensive discussions. Experimentally, several features unique to solids have been discovered such as the linear cutoff-energy scaling with field strength and a sudden transition from a single- to a multiple-plateau spectral structure. These experimental results have required the theoretical development of new methods and models that incorporate intrinsic characters of solids. Along with experiments, numerical approaches have played an important role in strong-field science to reveal underlying processes. Especially in solids, which have a plethora of effects that may overshadow pure electron responses inside materials, numerical methods are indispensable for revealing essential processes underlying the phenomena. Therefore, the development of numerical approaches to describe the many-electron system in solids in the strong-field regime has been in high demand. In this dissertation, I theoretically study the mechanism of the solid-state HHG by developing numerical methods, focusing on the following topics:

(i) Independent-electron dynamics in HHG in solids

The experimentally observed unique features of the solid-state HHG require development of new methods and models that incorporate the intrinsic properties of solids. In this work, we study HHG from solids using a one-dimensional model crystal by numerically solving the time-dependent Schrödinger equation (TDSE) within the independent-electron approximation. By solving the TDSE directly on a spatial grid, which involves multiple-band contribution in a natural manner, we successfully reproduce harmonic spectra with several unique features.

Based on the simulation results, we propose and discuss a simple semiclassical model that incorporates field-induced intraband displacement, interband tunneling excitation, and recombination with the valence-band hole. We show that electrons can climb up bands by repeating the interband tunneling to an upper band and intraband acceleration within one band, based on which, we predict yet another difference from gas-phase HHG that the position of the highest cutoff energy depends on not only the wavelength and field strength of the pulse but also its duration. The cutoff positions as well as the time-frequency structure of HHG can be deduced by tracing all the trajectories starting from different initial crystal momenta.

Our trajectory analysis can be viewed as a solid-state and momentum-space counterpart with multi-band extension of the three-step model in the gas-phase HHG, which has been highly successful for HHG from gas-phase atoms and molecules. It provides a unified basis for under- standing HHG from gaseous media and solid-state materials. This offers a clear physical insight into the coherent electron dynamics of

its independent nature and serves as a benchmark to identify the effects of electron correlation, relaxation, dephasing, impurity, distortion, etc., in real experiments.

(ii) Multielectron effects on HHG in solids

Unlike the ionized electrons from isolated atoms and molecules, electrons (tunnel-)excited to a conduction band move through the background of other electrons. While most of the previous discussions are based on the independent-electron approximations, the role of multielectron effects in solids in strong-field regime is largely unexplored.

In this work, we study the effects of the electron-hole interaction on the solid-state HHG by developing the time-dependent Hartree-Fock (TDHF) simulation methods. By numerically solving the TDHF equations for a one-dimensional model crystal, we have found a qualitative change in the harmonic spectra from what is obtained with the independent-electron simulations. In particular, the second plateau appears at a field strength much smaller than for the independent-electron case. Using the accelerated Bloch states, or the Houston states, we reveal that the Coulomb interaction from the interband polarization, or electron-hole polarization, mediates excitation of distant valence-band electrons.

If we shift our eyes back to the gas-phase HHG, the influence of the Coulomb potential from the parent ion, neglected in the strong-field approximation, may somewhat correspond to that of electron-hole interaction in solids. However, it hardly affects qualitative features of harmonic spectra. Our results suggest that the solid-state HHG mechanism involves much more complicated process than the gas-phase, and hence, may offer possible opportunities to reveal correlation in ultrafast electron dynamics in solids. The present study will pave the way toward the ultimate goal of revealing correlations in ultrafast electron dynamics in solids.

Acknowledgments

I would like to begin by thanking my supervisors Prof. Junji Yumoto and Prof. Kenichi L. Ishikawa. Prof. Yumoto has allowed me to work on both theoretical and experimental projects during my Ph.D. time. Without a great deal of freedom he has offered me, I could have never spent such wonderful days. Prof. Ishikawa has offered me a great opportunity to participate in a new theoretical project of strong-field phenomena in solid-state materials. I have learned a lot through a series of discussions with him, a leading researcher in ultrafast strong-field science.

I also wish to express my deepest gratitude to my advisor Prof. Makoto Kuwata-Gonokami. I always appreciate his helpful comments based on his deep insight into the optical processes in solids. His wide personal network has also helped me meet and have valuable discussions with many experts in the field; actually, it was one of such occasions when I had the first discussion on high-harmonic generation in solids with Prof. Ishikawa.

The Ishikawa group has been a wonderful place like a salad bowl of professionals in this field. I greatly thank Dr. Takeshi Sato and Dr. Yasushi Shinohara in Ishikawa group for their overall support. Dr. Sato has given me a lot of advice and support for developing the theoretical framework and numerical simulations. Plenty of discussions with Dr. Shinohara have always offered me new knowledge and insight. For example, the Houston-basis expansion presented in Ch. 5 was inspired by the discussion with him. Their critical questions in daily discussions have always helped me brush up my ideas.

I also really thank Dr. Kuniaki Konishi and Dr. Daisuke Hirano in Gonokami group for their experimental support and a lot of discussions. Dr. Konishi has always supported me a lot both academically and socially. The idea of the solid-state momentum-space three-step model presented in Ch. 4 was inspired by the discussion with him after my presentation at a group meeting. I also learned a lot of social manners from him. Dr. Daisuke Hirano has supported me working on experimental projects. I was always inspired by his suggestion and ideas based on his deep understanding of optical processes in solids and gas-phase high-harmonic generation.

I am also very grateful to Prof. Jiro Itatani and Dr. Nobuhisa Ishii, of the Institute for Solid State Physics, the University of Tokyo, and Dr. Katsuya Oguri and Dr. Hiroki Mashiko, of the Quantum Optical Physics research group, NTT Basic Research Laboratories, who have offered me wonderful opportunities to use their outstanding light source for experiments of high-harmonic generation from our samples. I have learned a lot from them, e.g., strong-field experimental know-how and professional insights on what takes place under an intense field. Although, unfortunately, we were unable to catch any signals, these experiences with field-leading expert researchers were definitely invaluable, exciting, and highly suggestive moments in my Ph.D. life.

I also feel thanks to all of the members of Gonokami group and Ishikawa group. I appreciate a lot of advice and support from academic staff members in Gonokami group and related groups, namely, Dr. Kosuke Yoshioka, Dr. Takuro Ideguchi, Dr. Munekazu Horikoshi, Mr. Yusuke Morita, Dr. Junko Omachi, Dr. Davide Bossini, Dr. Yusuke Arashida, and Dr. Natsuki Kanda. It was also exciting and lots of fun to have interaction with brilliant students, to name just a few, Mr. Natsuki Nemoto, Mr. Hirosuke Suzuki, Mr. Haruyuki Sakurai, Mr. Yo Iida, Ms. Mizuho Matoba, and Mr. Hiroki Matsui in Gonokami group, and Dr. Ryohto Sawada, Mr. Ryoji Anzaki, Mr. Yuki Orimo, and Mr. Takuma Teramura in Ishikawa group. I'm also grateful to secretaries, Ms. Masako Shirahama, Ms. Akane Oshima, Ms. Kimiko Kowashi in Gonokami group and Ms. Yumiko Kumaoka in Ishikawa group, for their plenty of support for me. I also express my thanks to Ms. Shoko Watanabe, the former secretary of Ishikawa group.

Last but not least, I would like to thank my family for their encouragement and courtesy during my Ph.D. life. In particular, without my parents' support, it would have been impossible to pursue my curiosity in physics at university. I express my greatest gratitude to my wife Shoko for her understanding in my career and total support for me.

Contents

Science without religion is lame, religion without science is blind.

Albert Einsten

1 Introduction

The advent of the laser in 1960 marks the beginning of the new era of nonlinear optics in the field of optical science. In the nonlinear regime, the optical properties of materials are no longer independent of incident electric field strength. Today, the advances in ultrafast intense laser techniques have likewise enabled us to enter a new stage beyond nonlinear optics: strong-field physics, where perturbative treatments of the incident electric field are no longer applicable. In particular, high-harmonic generation from gas-phase atoms and molecules has been one of the main targets of research for three decades, which has led to successful applications such as attosecond pulse [1–3] and coherent keV x-ray [4] generation, as well as the enablement of powerful means to observe and manipulate ultrafast electron dynamics [5–12]. Recently, solid-state materials have been in the limelight as a new stage for strong-field physics. In particular, since its first discovery in 2011 [13], many experimental observations of high-harmonic generation from solid-state materials, or *solid-state high-harmonic generation,* have been reported. The extension of the ideas and methods that have been developed in the gas-phase high-harmonic generation should lead to new scientific and technological opportunities. At the same time, it has been found that solid-state high-harmonic generation has several unique features, which requires the development of new methods and models to understand its nature. In this chapter, I will give an overview of the state-of-the-art of this field and remark on motivations of our works. Throughout this dissertation, atomic units[1] are used unless otherwise mentioned.

1.1 Strong-field physics in atoms and molecules

The development of laser techniques over the past 50 years has made available coherent fields whose intensities are as high as, or higher than, that of the atomic unit,

$$\frac{1}{2}\epsilon_0 c\mathcal{E}_{\mathrm{a}}^2 \approx 3.509 \times 10^{16}\ \mathrm{W/cm^2}, \tag{1.1}$$

where $\mathcal{E}_{\mathrm{a}}$ is the field strength of atomic unit given by

$$\mathcal{E}_{\mathrm{a}} = \frac{e}{(4\pi\epsilon_0)a_0^2} \approx 5.142 \times 10^9\ \mathrm{V/cm}, \tag{1.2}$$

[1]The details of atomic units are given in Appendix A.

with a_0 denoting the Bohr radius of hydrogen. The available field intensity has increased year by year, which has enabled us to investigate the light-matter interaction beyond the perturbative regime.

The emergence of intense laser fields has let us enter the regime of strong-field physics. The first observation of a strong-field phenomenon was in 1979, when Agostini *et al.* measured the field-ionized photoelectron energy spectra of xenon atoms [14]. At sufficiently high intensities, they found that ionized electrons absorb one more photon than energetically required to exceed the atomic ionization energy[2]. This is known today as above-threshold ionization (ATI). Through following experiments, multi-photon ATI peaks were also observed [15, 16]. Moreover, higher-order ATI peaks were found to not follow the n-th order power law expected from perturbation theory [15, 16] (Fig. 1.1).

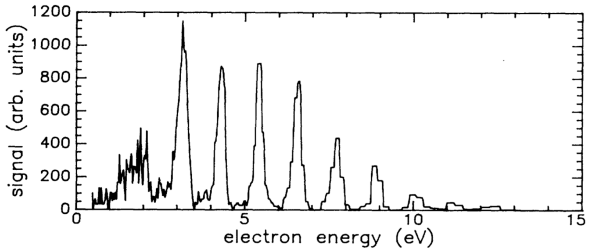

Figure 1.1: The ATI peaks observed in Ref. [15] from xenon atoms under 1064-nm field with the peak field intensity $I = 2 \times 10^{13}$ W/cm². The figure is taken from the reference.

Today, ATI can be understood in terms of the ponderomotive energy [17], which is the cycle-averaged electron kinetic energy in an oscillating electric field, given by

$$U_p \text{ (eV)} = \frac{e^2 \mathcal{E}_0^2}{4m\omega^2} = 9.337 \times 10^{-14} I(\text{W/cm}^2)\lambda^2(\mu\text{m}), \tag{1.3}$$

for an electron in vacuum. Here, $\mathcal{E}_0$ and ω denote field strength and its angular frequency, and e and m the electron charge and mass, respectively. For an infrared laser field with wavelength $\lambda = 1.06$ μm, the ponderomotive energy $U_p \approx 1.2$ eV at an intensity $I = 10^{13}$ W/cm². As the energy shift of a bound electron is negligible for nonresonant fields, the effective ionization potential becomes $I_p + U_p$, with I_p denoting the original ionization energy. This is why the ATI peaks appear at high intensities.

The nonperturbative behavior of high-energy ATI peaks is caused by tunneling ionization due to intense fields. In the case of a hydrogenic system under a quasi-static field, the tunneling rate is given by [18, 19],

$$W = \frac{4(2I_\text{p})^{5/2}}{\mathcal{E}} \exp\left(-\frac{4\sqrt{2}}{3}\frac{I_\text{p}^{3/2}}{\mathcal{E}}\right), \tag{1.4}$$

where $\mathcal{E}$ is the field strength. For sufficiently intense fields, the tunneling rate becomes large and electrons can be ionized via tunneling. Because of the exponential factor in Eq. (1.4), tunneling ionization takes place mainly at the peak of the oscillating electric field every half cycle. This temporally periodic burst of ionized electrons results in the discrete ATI peaks in the energy domain.

[2] Considering energy and momentum conservation, a free electron in vacuum cannot absorb a photon, i.e., free-free transition is forbidden. An electron can absorb a photon only when it is close to a parent ion who is able to absorb the remaining momentum difference. For such reasons, the observation of ATI was considered controversial at that time.

1.2 High-harmonic generation (HHG)

Some of the tunnel-ionized electrons return to the origin after gaining kinetic energy through the acceleration in an oscillating field and collide with the parent ion, emitting a high-energy photon, who takes away the electron energy. This phenomenon is known as the high-harmonic generation (HHG), which was first observed in the late 1980s. The spectrum of HHG light has a unique structure (Fig. 1.2): it has a *plateau* extending over the higher-energy region, in which the radiation efficiency dose not decrease with the harmonic order, and has a sharp *cutoff* at which the plateau starts to fall down. The plateau structure is a signature of the nonperturbative nature of HHG. The cutoff energy E_c is known to follow the cutoff law [20–23], given by

$$E_c \approx I_p + 3U_p. \tag{1.5}$$

This cutoff law can be verified using either a semiclassical recollision model [21, 22] or a quantum mechanical approach with strong-field approximation (SFA), known as the Lewenstein model [23].

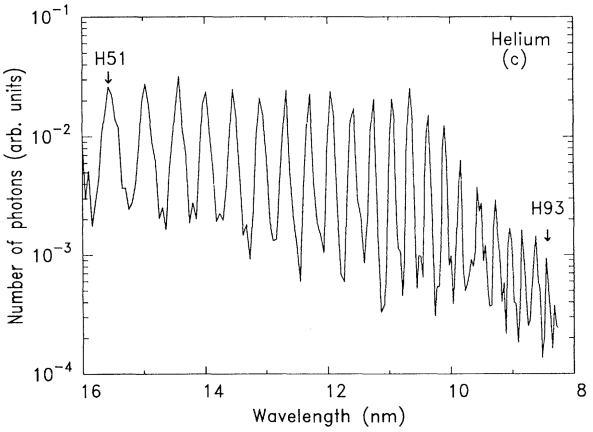

Figure 1.2: HHG spectrum from He atoms driven by high intensity laser field $\sim 10^{15}$ W/cm² in the experiment by Wahlström *et al.* [24], which shows a typical structure of harmonic spectra, with a plateau spanning over a wide energy range and a sharp cutoff at around 10 nm.

1.2.1 Semiclassical three-step model

Many features of HHG from atoms can be explained in terms of a semiclassical three-step model (TSM) [21, 22], both intuitively and even qualitatively. In the TSM, an electron is first tunnel-ionized from the parent ion to the continuum with zero kinetic energy (step 1: *tunneling*). Subsequently, the electron is accelerated by the oscillating field during its half-cycle, and then decelerated and accelerated again in the reverse direction in the next half-cycle (step 2: *acceleration*). When the electron comes back to the nuclei position, with a certain probability, the electron undergoes recombination with the parent ion, emitting a photon which takes all the electron's energy: the sum of the ionization potential I_p and the gained kinetic energy through the acceleration (step 3: recombination). In the TSM, the tunneling ionization and the recombination are treated quantum mechanically, while the acceleration is treated by classical mechanics.

The cutoff energy can be predicted from the maximum energy gained by electrons during the acceleration. Let us consider the classical motion of the ionized electron at time t_i at the nuclei position $x(t_i) = 0$ with its velocity $\dot{x}(t_i) = 0$ in an electric field $\mathcal{E}(t) = \mathcal{E}_0 \cos(\omega t)$. The electron position and its

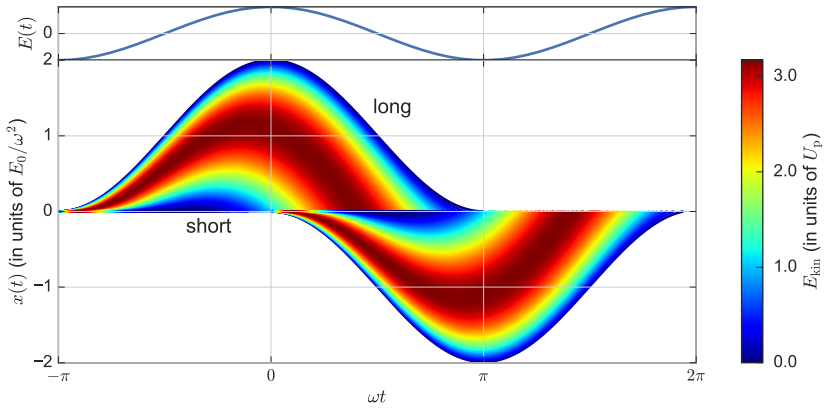

Figure 1.3: The real-space trajectory $x(t)$ of each electron that is tunnel-ionized at $t = t_i$ and returns to the original position at $t = t_r$ with kinetic energy $E_{\rm kin}$. The line color represents the final kinetic energy at the recombination. The oscillating field is shown in the upper panel.

kinetic energy at time t are given by

$$x(t,t_i) = \frac{\mathcal{E}_0}{\omega^2}\left[\cos(\omega t) - \cos(\omega t_i) + \sin(\omega t_i)(\omega t - \omega t_i)\right], \tag{1.6}$$

$$E_{\rm kin}(t,t_i) = 2U_p\left(\sin(\omega t) - \sin(\omega t_i)\right)^2, \tag{1.7}$$

respectively.

We draw the electron trajectories $x(t,t_i)$ for different birth times t_i in Fig. 1.3. The color of each trajectory represents its final kinetic energy[3] $E_{\rm kin}(t_i,t_r)$ at the recollision time t_r. $E_{\rm kin}(t_r,t_i)$ takes its maximum value $3.17U_{\rm p}$ at $\omega t_i = -0.9\times\pi$ and $\omega t_i = 0.1\pi$. Thus, the maximum harmonic energy is given by $I_{\rm p} + 3.17U_{\rm p}$, which well explains the cutoff law of Eq. (1.5). Moreover, these birth timings are close to the peak of the oscillating laser field [see Fig. 1.3], and the ionization rate given by Eq. (1.4) is quite high. For such reasons, the harmonic yield is high up to the cutoff energy.

1.2.2 Lewenstein model

The simplest quantum treatment of HHG is the Lewenstein model, which was proposed by Lewenstein *et al.* in 1994 [23]. It gives quantum mechanical grounds to the semiclassical TSM. In the Lewenstein model, we employ the SFA, namely,

- All contributions from the atomic bound excited states are negligible.
- The effects of the atomic potential $V(\boldsymbol{r})$ on the electrons in the continuum states are negligible.
- The depletion of the ground state is negligible.

Under these assumptions, we assume an electron wave function as

$$\psi(\boldsymbol{r},t) = e^{-iI_p t}\left(\phi_0(\boldsymbol{r},t) + \int d\boldsymbol{k} b(\boldsymbol{k},t)\chi_{\boldsymbol{k}}(\boldsymbol{r},t)\right), \tag{1.8}$$

[3] One can notice that there exist two trajectories that contribute to the same kinetic energy; the trajectory which recombine at the earlier timing is called the *short* trajectory, and the other which returns later is called the *long* trajectory.

where $\phi_0(\boldsymbol{r})$ is the ground state whose binding energy is I_p, and $\chi_{\boldsymbol{k}}(\boldsymbol{r},t)$ is the Gordon-Volkov wave function [17, 25], corresponding to a dressed free electron in vacuum.

The harmonic spectrum can be obtained from the Fourier transform of the dipole moment $\boldsymbol{d}(t)$, given by

$$\boldsymbol{d}(\omega) = i\int_{-\infty}^{\infty} dt \int_{-\infty}^{t} dt' \int d\boldsymbol{k}\, \langle \phi_0 |\, \boldsymbol{r}\, | \boldsymbol{k}+\boldsymbol{A}(t)\rangle \exp[i\omega t - iS(\boldsymbol{k},t,t')]\, \langle \boldsymbol{k}+\boldsymbol{A}(t')|\, \boldsymbol{r}\cdot\boldsymbol{\mathcal{E}}(t')\, |\phi_0\rangle + \text{c.c.}, \quad (1.9)$$

where $\boldsymbol{A}(t) = \int \boldsymbol{\mathcal{E}}(t)dt$ is the vector potential of the electric field $\boldsymbol{\mathcal{E}}(t)$. $\langle \phi_0 |\, \boldsymbol{r}\, | \boldsymbol{k}+\boldsymbol{A}(t)\rangle$, $\exp[-iS(\boldsymbol{k},t,t')]$, and $\langle \boldsymbol{k}+A(t')|\, \boldsymbol{r}\cdot\boldsymbol{\mathcal{E}}(t')\, |\phi_0\rangle$ correspond to the ionization amplitude at t', the quantum phase obtained during the propagation from t' to t, and the recombination amplitude at t, respectively. Equation (1.9) involves a five dimensional integral over $\boldsymbol{k}, t, t'$ and can be evaluated using the saddle-point method. The stationary conditions for $\omega t - S(\boldsymbol{k},t,t')$ with respect to $\boldsymbol{k}, t$ and t' yield

$$\int_{t'}^{t} [\boldsymbol{k}+\boldsymbol{A}(t'')]\, dt'' = 0, \quad (1.10)$$

$$\frac{(\boldsymbol{k}+\boldsymbol{A}(t))^2}{2} + I_p = \omega, \quad (1.11)$$

$$\frac{(\boldsymbol{k}+\boldsymbol{A}(t'))^2}{2} = -I_p. \quad (1.12)$$

Equation (1.10) states that the displacement of the ionized electron $\boldsymbol{r}(t,t') = \int_{t'}^{t} [\boldsymbol{k}+\boldsymbol{A}(t'')]\, dt''$ is zero, i.e., the ionization and the recombination take place at the same position. Equation (1.11) represents an energy conservation, i.e., the photon energy is given by the sum of the electron kinetic energy and the ionization potential I_p. Equation (1.12) determines the birth time t' of a free electron via tunneling.

1.2.3 Applications of HHG

Currently, HHG is viewed as a promising way to produce ultrashort coherent light. One considerable application is the generation of high-energy soft x-ray light reaching the keV regime. Popmintchev *et al.* demonstrated the generation of coherent high harmonics in the keV x-ray regime [4], which can be applied to spectroscopy of many materials of interest, whose inner shell absorption edges are in the keV regime. Another interest is the generation of an isolated attosecond pulse, which enables ultrafast spectroscopy with sub-fs time resolution. In 2008, Goulielmakis *et al.* demonstrated the generation of an isolated attosecond pulse with 80 attosecond pulse duration [1]. This was followed by the generation of a 67 attosecond isolated pulse by Zhao *et al.* in 2012 [2]. At present, the shortest isolated attosecond pulse has a 43 attosecond pulse duration, which was achieved by Gaumnitz *et al.* in 2017 [3].

Another important application of HHG is orbital tomography, demonstrated by Itatani *et al.* in 2004 [5]. The recollision process can be seen as an interferometer between a bound-state wave function Ψ_{g} and a recolliding wave function Ψ_{c}. The harmonic radiation arises from this interference, and thus, the information of the interference is encoded into the harmonic spectra. In their experiment, Itatani *et al.* measured the harmonic spectra from N_2 as a function of molecular alignment, and obtained a tomographic image of the molecular orbital of N_2 (Fig. 1.4). This molecular imaging technique has offered a powerful way to probe the ultrafast electron state and its dynamics in molecules [5, 10, 26].

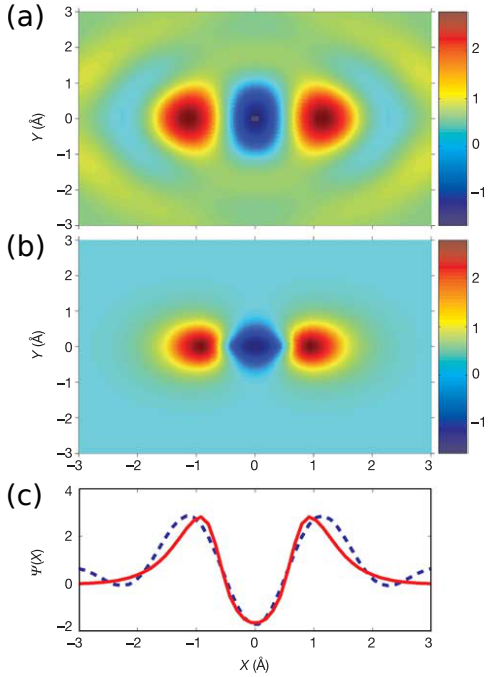

Figure 1.4: Tomographic imaging demonstrated by Itatani *et al.*. This figure is taken from Ref. [5]. (a) Reconstructed orbital of N_2 from high-harmonic spectra. (b) The orbital calculated by an *ab-initio* theory. (c) The wave function along the internuclear axis for the reconstructed (dashed blue) and calculated (solid red) orbitals.

1.3 HHG from solids

Solid-state materials have recently emerged as a new stage of strong-field and attosecond physics. In particular, since the first breakthrough by Ghimire *et al.* in 2011 [13], many experimental observations of solid-state HHG have been reported, from dielectrics [27–31] as well as semiconductors [32–39]. These experiments have revealed several unique features of solid-state HHG, such as the linear scaling of the cutoff energy with field strength [13, 27, 40] and the multiple-plateau structure in harmonic spectra [29, 38]. In contrast to gas-phase HHG, however, the underlying processes are still under intensive discussions.

In an experiment of solid-state HHG, typically, a sample is driven by an intense pulse electric field with a low central frequency significantly off-resonant to the gap energy, to suppress single- or few-photon excitation and subsequent breakdown of the material. For experiments using semiconductors, mid-infra red (MIR) or terahertz (THz) fields are often used, e.g., Ghimire *et al.* used a MIR field with wavelength $\lambda = 3.25\ \mu$m for ZnO (band gap 3.2 eV) [13] and Schubert *et al.* used a THz field with $\lambda = 10\ \mu$m for GaSe (band gap 2.0 eV) [32]. For dielectrics, visible to infra-red (IR) fields (up to a few μm) have been used, e.g., Luu *et al.* used half-cycle visible pulses with spectral range 1.1-2.5 eV (corresponding to $\lambda = 500$-1030 nm) for SiO_2 (band gap 9.0 eV) [27]. All these experiments have taken advantage of ultrashort pulses from half- to few-cycle to realize a high peak field strength of ~ 1.0 V/Å, comparable to the field strength of the atomic unit $\mathcal{E}_a$.

1.3.1 Linear scaling of cutoff energy with field strength

Several authors [13, 27, 32] have reported a linear scaling of cutoff energy with field strength. This is in marked contrast with that of gas-phase HHG which shows quadratic scaling with field strength. Ghimire *et al.* used a few-cycle MIR laser pulse with wavelength $\lambda = 3.25\ \mu$m to excite a ZnO bulk crystal, and suc-

cessfully observed HHG up to 25-th order, which showed a nonperturbative character and linear scaling of cutoff energy (Fig. 1.5).

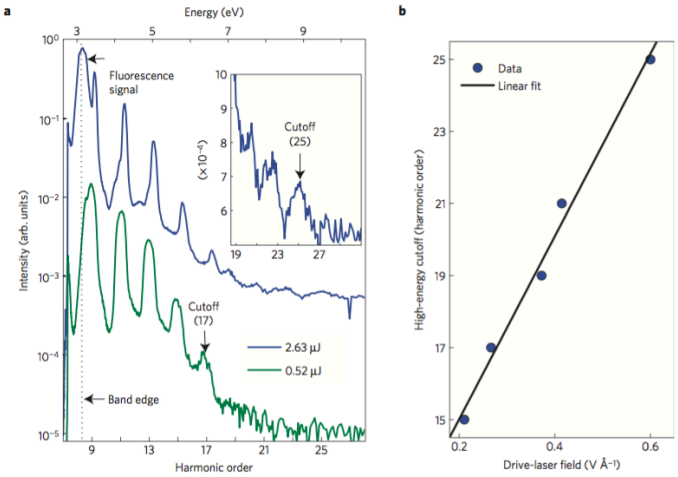

Figure 1.5: Measured HHG spectra and field dependence of the cutoff by Ghimire *et al.* [13]. The figure is taken from Ref. [13]. (a) Spectra from the ZnO crystal for field strength $0.27\ \mathrm{V/Å}$ (green) and $0.6\ \mathrm{V/Å}$ (blue). The dotted vertical line represents the band gap energy evaluated experimentally. (b) The cutoff-energy scaling with the field strength.

The linear scaling was also observed in SiO_2, a wide-gap insulator with gap energy ~ 9 eV. Luu *et al.* exposed a polycrystalline SiO_2 film to an intense optical field whose central photon energy ~ 2 eV, and observed HHG up to more than 20 eV in the extreme ultraviolet (EUV) range. They reported that the cutoff energy underwent a linear increase with the field strength (Fig. 1.6).

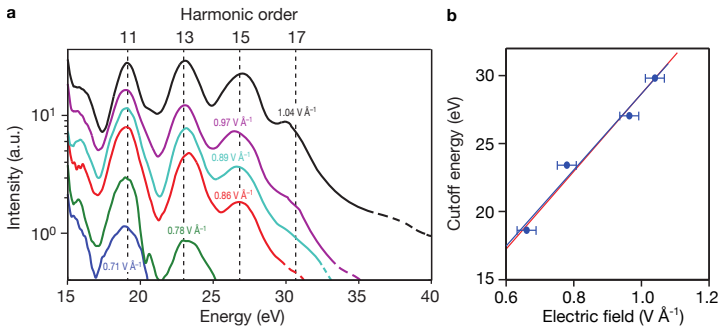

Figure 1.6: HHG from the thin SiO_2 film exposed to the 1.5-cycle optical pulse [27]. Figures are extracted from Ref. [27] and were rearranged by the author. (a) EUV harmonic spectra for several field strengths. The dashed portion of the curve represents the noise floor. (b) Cutoff energy as a function of the field strength.

The linear scaling law of the cutoff energy of solid-state HHG was also reported in Ref. [32], in which a semiconductor sample (GaSe) was driven by an intense THz field.

The linear scaling is a striking feature of HHG from solid-state materials. It indicates an underlying mechanism different from that of gas-phase HHG, which has stimulated debates on the radiation process of high harmonics in solid-state materials.

1.3.2 Multiple-plateau structure

Another example of the uniqueness of solid-state HHG can be seen in an appearance of multiple-plateau structure in harmonic spectra. In a recent experiment, Ndabashimiye *et al.* compared HHG from rare

gases in solid and gas phase [29] in order to reveal the similarities and differences between them. The experiments were performed on polycrystalline and gaseous Ar and Kr. The samples were exposed to a 50-fs, 1.3-μm IR pulse and harmonic spectra were recorded for several field strengths.

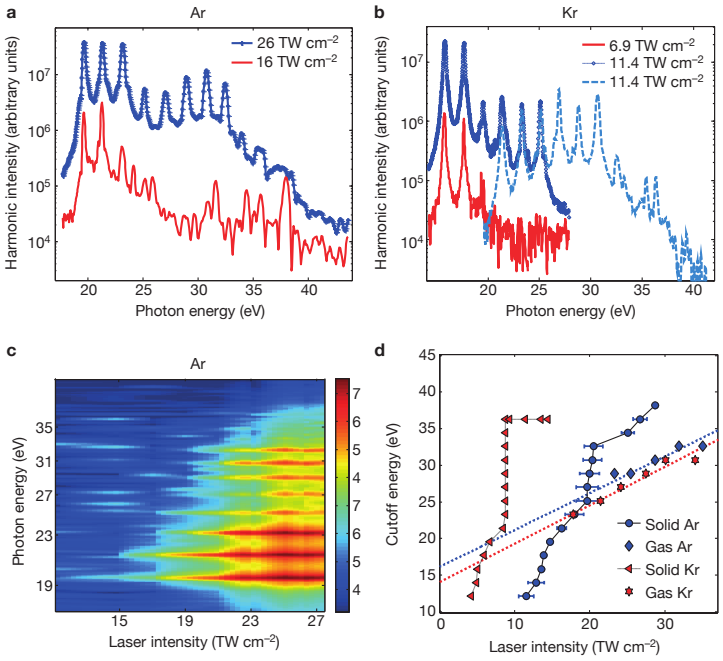

Figure 1.7: Harmonic spectra from solid Ar and Kr measured by Ndabashimiye *et al.* [29]. Figures are extracted from Ref. [29] and rearranged by the author. (a, b) HHG spectra from solid (a) Ar and (b) Kr driven by a 1.3-μm field with two intensities. (c) HHG spectra from solid Ar as a function of the laser intensity. (d) The cutoff energy positions of HHG from solid and gaseous Ar and Kr as a function of the laser intensity. The dotted straight lines are linear fits to the cutoff energy positions of gaseous Ar (blue) and Kr (red).

Figures 1.7 (a) and (b) show representative harmonic spectra from solid Ar and Kr at two intensities. Each series of the spectra shows a qualitatively similar structure: a single plateau similar to gas-phase HHG is evident at the lower intensity, whereas a second plateau with lower harmonic intensity appears at higher laser intensity at 25-33 eV for Ar and at 19-31 eV for Kr. Figure 1.7(c) shows the harmonic spectra from solid Ar as a function of the laser intensity. With increasing laser intensity, the second plateau appears at about 20 TW/cm^2. Figure 1.7(d) compares the cutoff energies of solid and gaseous Ar and Kr as functions of the laser intensity. The high-energy extent of the second plateau significantly exceeds the cutoff energy of the gas-phase at the same intensity. Similar structure of higher plateaus with lower intensity was also observed in more recent experiment with single-crystal MgO [38]. The appearance of multiple plateaus marks a strong interband coupling of higher-lying conduction band (CB)s, which is also a unique feature of HHG in solid-state materials.

1.3.3 Field polarization and crystal symmetry

The crystalline structure plays a strong role in characterizing the intrinsic properties of a solid-state material. Recently, the influence of the crystalline symmetry on HHG has attracted wide attention [35–37, 39]. For instance, Langer *et al.* have demonstrated the control of the temporal structure of HHG by crystal symmetry and field polarization. They excited a GaSe bulk crystal, which exhibits a three-fold rotational axis and a horizontal mirror plane symmetry, with linearly polarized intense few-cycle THz pulse, whose peak intensity was 47 MV/cm. They measured the harmonic spectra as functions of the crystal angle φ

with respect to the field polarization, where $\varphi = 0°$ corresponds to the direction where $\boldsymbol{e}_1 - \boldsymbol{e}_2$ is parallel to the field [Fig.1.8(a)].

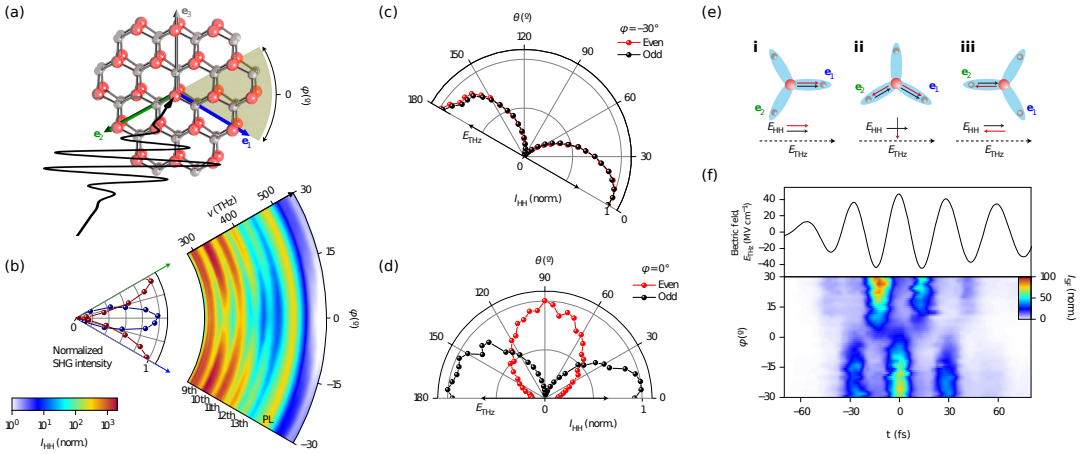

Figure 1.8: Investigation on HHG in solid-state materials for different crystal angles by Langer *et al.*. These figures are taken from Ref. [37] and rearranged by the author. (a) The crystal structure of GaSe with three axes $\boldsymbol{e}_1$, $\boldsymbol{e}_2$, and $\boldsymbol{e}_3$. The crystal angle φ is defined with respect to the field polarization. (b) High-harmonic yield I_{HH} as functions of the crystal angle φ. The label 'PL' indicates the photoluminescence peak of GaSe. (c, d) Normalized intensity of even (red) and odd (black) harmonics as functions of the polarization θ with respect to the field polarization, for $\varphi = -30°$ (c) and $\varphi = 0°$ (d). (e) Illustrative representation of the main contributing crystal directions for $\varphi = -30°$ (i), $\varphi = 0°$ (ii), and $\varphi = 30°$ (iii). (f) Temporal structure of the total high-harmonic radiation measured by recording the intensity of the sum frequency $I_{\mathrm{SF}}(t)$ between the harmonic field and an 8-fs near-infrared (NIR) gating pulse as functions of the delay time t.

The measured spectra show a clear six-fold symmetry reflecting the symmetry of the GaSe crystal [Fig. 1.8(b)]. They analyzed the polarization of even and odd harmonics by measuring each intensity as functions of θ, corresponding to the relative angle of the polarizations of the harmonics and the THz field, for $\varphi = -30°$ [Fig. 1.8(c)] and $\varphi = 0°$ [Fig. 1.8(d)]. While the odd harmonics are always polarized along the THz field, the polarization of the even harmonics changes from parallel when $\varphi = -30°$ to perpendicular when $\varphi = 0°$ to the field polarization. They attributed this results to the field induced polarizations along three crystalline axes [Fig. 1.8 (e)]. When $\varphi = -30°$ ($\boldsymbol{\mathcal{E}}_{\mathrm{THz}} \parallel \boldsymbol{e}_1$) or $\varphi = 30°$ ($\boldsymbol{\mathcal{E}}_{\mathrm{THz}} \parallel \boldsymbol{e}_2$), the polarization of both even and odd harmonics is along the THz field [Fig. 1.8(e)-**i** and **iii**]. When $\varphi = 0°$ ($\boldsymbol{\mathcal{E}}_{\mathrm{THz}} \parallel \boldsymbol{e}_1 - \boldsymbol{e}_2$), on the other hand, the polarization of even harmonics becomes perpendicular to the field [Fig. 1.8(e)-**ii**]. Applying this process, they also demonstrated a control of the temporal waveform of HHG by the crystal angle as shown in Fig. 1.8(f). Their results suggest the possibility of controlling and manipulating the polarization and temporal structure of HHG from solids by taking advantage of crystal symmetry and polarization of the incident field.

1.4 Theoretical models for solid-state HHG

The mechanism of solid-state HHG is still under intensive discussions. In general, intense electric fields are considered to be able to induce both the interband and intraband electron dynamics in the momentum space; the former refers to (usually vertical, tunneling) transitions between different bands, and the latter to displacements in the momentum space within one band. So far, a variety of modeling approaches have been proposed to explain the observed unique features of solid-state HHG.

1.4.1 Models for linear scaling of cutoff energy

The linear scaling of the cutoff energy with the driving field strength is one of the most striking features of solid-state HHG, distinguishing it from the gas-phase HHG. Here I introduce several models that have been proposed to explain this feature.

Real carrier acceleration

Historically, solid-state HHG was first discussed in terms of the Bloch oscillation, or the pure intraband motion within one band [13, 27, 32, 41]. In this intuitive picture, we consider the field-induced intraband acceleration of excited electrons in a CB, which are generated via a tunneling process. When the accelerated electrons reach an anharmonic region of the band, they emit nonlinear radiation. By considering an electron wavepacket generated at the Γ point of a CB, one can derive an analytic form for generated harmonic spectra, based on which the linear scaling law can be discussed [13].

Real-space three-step model

On the other hand, the interband dynamics can also be considered a radiation source. Some theoretical studies have shown that the interband dynamics makes a main contribution to radiation above the band gap energy [42–44]. In this context, Vampa *et al.* have proposed a real-space three-step model by analyzing the interband contribution in a similar manner as the Lewenstein model [23]. Based on the saddle-point approximation, they derived a three-step model for solid HHG:

1. Tunneling: an electron in the valence band (VB) is tunnel-ionized to the CB at the crystal momentum with the minimum bandgap energy.
2. Acceleration: subsequently, the electron and hole are accelerated by the field in opposite directions in real space.
3. Recombination: the electron-hole pair undergoes recombination accompanied by photoemission when the electron and the hole reencounter. The radiation energy is determined by the electron-hole energy difference at this timing.

In this model, the linear scaling of the cutoff energy can be explained by the linearity of the energy difference of the CB and the VB. While they showed a good agreement of this picture with their quantum-mechanical simulation results [45], the validity of the extension of the real-space picture used in gas-phase HHG is controversial because the excited states in solids are spatially delocalized over unit cells.

Wannier-Stark dressed-state approach

Higuchi *et al.* [46] have proposed a real-space picture using localized Wannier-Stark (WS) dressed states based in the strong-field limit, i.e., $|\mathcal{E}| > \Delta_{\mathrm{g}}/ae$ with Δ_{g} and a denoting the bandgap energy and lattice constant, respectively. In this picture, the energy differences of the quasienergies of WS states determine the radiation energies. The radiation yields are determined by the current matrix elements between different dressed states. Their picture can be seen as the analogue to the quantum cascade laser, in which the energy differences between minibands formed in semiconductor superlattices determine the radiation frequencies [47, 48].

1.4.2 Models for multiple-plateau structure

The appearance of the additional higher-energy plateaus with lower intensity [29, 38] also constitutes a difference between solid-state and gas-phase HHG. It implies the strong coupling among higher-lying CBs, and thus should reflect the electronic structure of solids.

Interband Bloch oscillation

McDonald *et al.* [49] have solved the semiconductor-Bloch equations (SBE) without interelectronic Coulomb interaction and reported a second plateau formation even when only a single VB and a single CB are considered. They have proposed that an electron-hole pair that undergoes Bloch oscillations leads to a cascaded nonlinearity, which forms an additional plateau beyond the maximum energy difference between the CB and the VB.

Dressed multi-level system

Starting from a narrow population on the VB, Ndabashimiye *et al.* [29, 50] have proposed that the solid-state system under an intense field can be considered as a dressed multi-level system, rather than explicitly invoking the intraband dynamics. They have also pointed out that the dressed system can be mapped onto the band structure, which leads to a semiclassical three-step model in momentum space for an electron initially located at the Γ point.

1.5 Numerical approaches for solid-state HHG

Along with experimental efforts, numerical simulation methods have played a critical role in facilitating the understanding of the physical process behind the strong-field phenomena. In general, the quantum dynamics of the many-body electron system is governed by the many-body time-dependent Schrödinger equation (TDSE). For gas-phase isolated systems, several techniques have been developed to solve the many-body time-dependent Schrödinger equation (TDSE) under a strong electric field (see, e.g., [51]). However, it is highly computationally demanding and often infeasible with current computational resources to directly solve the many-body problem for solids, and thus we must use approximate methods to describe the process. The most commonly used methods in the strong-field regime at present are the single-electron TDSE within the independent-electron approximation (IEA) [43, 46, 52–54] and the semiconductor-Bloch equations (SBE) [30, 34, 37, 42, 55], while some authors have used the time-dependent density functional theory (TDDFT) [44, 56, 57].

1.5.1 Independent electron approximation (IEA)

In the independent-electron approximation (IEA), one solves the effective single-electron TDSE for each electron orbitals in a periodic system with an effective periodic potential $v_{\text{eff}}(\boldsymbol{r})$,

$$\begin{aligned} i\frac{\partial}{\partial t}\psi_{b,\boldsymbol{k}_0}(\boldsymbol{r},t) &= \hat{h}(t)\psi_{b,\boldsymbol{k}_0}(\boldsymbol{r},t) \\ &= \left\{\frac{1}{2}\left[\hat{\boldsymbol{p}}+\boldsymbol{A}(t)\right]^2 + v_{\text{eff}}(\boldsymbol{r})\right\}\psi(\boldsymbol{r},t)_{b,\boldsymbol{k}_0}. \end{aligned} \tag{1.13}$$

The IEA has been widely used to obtain heuristic insights into the field-driven many-electron dynamics in periodic systems [43, 46, 52–54].

In previous works, the TDSE has often been solved using certain basis sets such as the Bloch basis and the Houston basis. Bloch basis $\phi_{\lambda,\boldsymbol{k}}$ are the eigenstates of the field-free single-electron Hamiltonian $\hat{h}_0 = \hat{p}^2/2 + v_{\text{eff}}(\mathrm{r})$ with eigenenergies $\varepsilon_{\lambda,\boldsymbol{k}}$, or $\hat{h}_0\phi_{\lambda,\boldsymbol{k}} = \varepsilon_{\lambda,\boldsymbol{k}}\phi_{\lambda,\boldsymbol{k}}$. Korbman *et al.* [52] have solved the TDSE numerically for a model one-dimensional (1D) system using the Bloch basis $\phi_{\lambda,\boldsymbol{k}}$. Based on the wavelet analysis, they have shown that the instantaneous high-harmonic frequency varies in time, and have analyzed it in terms of the ponderomotive energy U_p. They have pointed out that the harmonic frequency averaged over a laser cycle is larger than the bandgap energy by the ponderomotive energy U_p, unless U_p exceeds the width of the lowest CB.

The Houston basis is a set of adiabatic states of Bloch electrons under an electric field [58] defined as $\tilde{\phi}_{\lambda,\boldsymbol{k}_0} = e^{-i\boldsymbol{A}(t)\cdot\boldsymbol{r}}\phi_{\lambda,\boldsymbol{k}(t)}$, where $\boldsymbol{k}(t) = \boldsymbol{k}_0 + \boldsymbol{A}(t)$. By solving the TDSE for a model 1D system using the Houston basis [53], Hawkins *et al.* have pointed out the importance of multiple bands and transitions among them for high-harmonic spectra. When only a single CB is considered, the lack of transitions to upper CBs causes strong Bragg reflections and Bloch oscillations that result in artificial generation of high energy harmonic component, whereas including multiple CBs removes these effects.

Wu *et al.* [43] have also suggested the importance of multiple energy bands based on their TDSE simulation results using the Bloch basis. They have shown that the contributions from multiple bands can lead to the formation of additional plateaus, extending HHG to higher photon energies. Here, it should be noted that they use an initial condition which has only a small population at the Γ point on the VB, rather than a filled VB which is a more natural choice [42, 52, 53]. Although they have argued that this initial condition is to prepare a spatially delocalized wave function, and that a filled VB is meaningful only in a multielectron picture, the validity of this initial condition is unclear.

1.5.2 Semiconductor Bloch equation

An alternative way to treat the many-electron system is second-quantization approach. In particular, the semiconductor-Bloch equations (SBE), a second-quantization approach combined with the mean-field approximation, has been used to describe HHG in solid-state materials [30, 34, 37, 42, 55]. In the SBE, one solves a set of differential equations for interband polarizations $p_{\boldsymbol{k}}^{\lambda\lambda'}$ and band populations $f_{\boldsymbol{k}}^{\lambda}$ [59],

$$\begin{aligned} i\frac{\partial}{\partial t}p_{\boldsymbol{k}}^{\lambda\lambda'} &= (\tilde{\varepsilon}_{\lambda',\boldsymbol{k}} - \tilde{\varepsilon}_{\lambda,\boldsymbol{k}})p_{\boldsymbol{k}}^{\lambda\lambda'} \\ &\quad + \Omega_{\boldsymbol{k}}^{\lambda\lambda'}\left(f_{\boldsymbol{k}}^{\lambda} - f_{\boldsymbol{k}}^{\lambda'}\right) + \sum_{\mu\neq\lambda,\lambda'}\left(\Omega_{\boldsymbol{k}}^{\lambda\mu}p_{\boldsymbol{k}}^{\mu\lambda'} - p_{\boldsymbol{k}}^{\lambda\mu}\Omega_{\boldsymbol{k}}^{\mu\lambda'}\right), \end{aligned} \tag{1.14}$$

$$i\frac{\partial}{\partial t}f_{\boldsymbol{k}}^{\lambda} = -\sum_{\mu\neq\lambda}\left(\Omega_{\boldsymbol{k}}^{\lambda\mu}p_{\boldsymbol{k}}^{\mu\lambda} - p_{\boldsymbol{k}}^{\lambda\mu}\Omega_{\boldsymbol{k}}^{\mu\lambda}\right), \tag{1.15}$$

where the renormalized Rabi frequency $\Omega_{\boldsymbol{k}}^{\lambda\lambda'}$ and renormalized single particle energy $\tilde{\varepsilon}_{\lambda,\boldsymbol{k}}$ are given by

$$\Omega_{\boldsymbol{k}}^{\lambda\lambda'} = -\boldsymbol{d}_{\boldsymbol{k}}^{\lambda'\lambda}\cdot\boldsymbol{\mathcal{E}}(t) + \sum_{\boldsymbol{q}\neq\boldsymbol{k}} v_{\boldsymbol{k}-\boldsymbol{q}}p_{\boldsymbol{q}}^{\lambda\lambda'}, \tag{1.16}$$

$$\tilde{\varepsilon}_{\lambda,\boldsymbol{k}} = \varepsilon_{\lambda,\boldsymbol{k}} - \sum_{\boldsymbol{q}\neq\boldsymbol{k}} v_{\boldsymbol{k}-\boldsymbol{q}}^{\lambda\lambda'}f_{\boldsymbol{q}}^{\lambda} + \boldsymbol{\mathcal{E}}(t)\cdot\boldsymbol{d}_{\boldsymbol{k}}^{\lambda\lambda}. \tag{1.17}$$

Here, v_q denotes the spatial Fourier components of the interelectronic Coulomb potential.

The effects of the interelectronic Coulomb interaction at a mean-field level are represented by the

coupling with polarizations and populations at other crystal momentum, i.e., the second terms in the right-hand side of Eq. (1.16) and Eq. (1.17), respectively. These terms, however, have often been ignored in the previous works [30, 34, 37, 42, 55], which makes the theory just an independent-electron model without the mean-field potential.

In order to solve the SBE, one has to prepare the band dispersion $\varepsilon_{\lambda,k}$ and dipole moment $\boldsymbol{d}_{\boldsymbol{k}}^{\lambda\lambda'}$ in some way. For instance, Vampa *et al.* [42] have solved the SBE without a Coulomb interaction term for ZnO using the parameters obtained from density functional theory (DFT) in the local density approximation. They have shown that the interband current makes a dominant contribution to the radiation above the band gap energy, relative to the intraband current. They claim that the same conclusions can be deduced when they use parameters from DFT in the nonlocal empirical pseudopotential method.

Garg *et al.* [30] have recently reported that the strength of the Coulomb interaction can significantly alter the response of a system based on SBE study. Considering three VBs and nine CBs, they numerically evaluated the HHG radiation from a SiO_2 crystal along the Γ-M direction. They reported that an increase in the strength of the Coulomb interaction results in an increase in the yield of harmonic radiation.

1.5.3 Time-dependent density functional theory

Some authors have attempted to attain *ab-initio* descriptions based on a TDDFT approach [44, 56, 57]. The TDDFT formalism is based on the time-dependent Kohn-Sham equation with an exchange-correlation energy functional,

$$i\frac{\partial}{\partial t}\psi_i(\boldsymbol{r},t) = \hat{h}_{\mathrm{KS}}[n;\Psi_0]\psi_i(\boldsymbol{r},t), \tag{1.18}$$

$$\hat{h}_{\mathrm{KS}}[n;\Psi_0] = -\frac{\nabla^2}{2} + v_{\mathrm{KS}}[n;\Psi_0](\boldsymbol{r},t), \tag{1.19}$$

$$v_{\mathrm{KS}}[n;\Psi_0](\boldsymbol{r},t) = v_{\mathrm{ext}}(\boldsymbol{r},t) + \int d\boldsymbol{r}\frac{n(\boldsymbol{r}',t)}{|\boldsymbol{r}-\boldsymbol{r}'|} + v_{\mathrm{xc}}[n;\Psi_0](\boldsymbol{r},t), \tag{1.20}$$

$$n(\boldsymbol{r},t) = \sum_i |\psi_i(\boldsymbol{r},t)|^2, \tag{1.21}$$

where $\psi_i(\boldsymbol{r},t)$ is the Kohn-Sham orbital and $v_{\mathrm{xc}}[n;\Psi_0](\boldsymbol{r},t)$ is the exchange-correlation potential.

Although *in principle* TDDFT can reproduce exactly the same results as the exact many-body TDSE, the choice of the correlation functional is critical, and we currently have no guidelines for the choise. In fact, TDDFT at present, which relies on a simple adiabatic local density approximation functional, is known to be unable to reproduce excitonic features [60]. For example, in their TDDFT study within adiabatic local density approximation (ALDA), Tancogne-Dejean *et al.* [57] have reported that there are no differences between the results from a full time evolution of the Coulomb and the exchange-correlation part of v_{KS} and those from a time evolution in a static ground-state potential (i.e., independent particle). Their results suggest that it is still difficult to take into account the many electron effects in the study of solid-state HHG.

1.6 Summary and motivation

In recent years, many experimental observations of solid-state HHG [27–40] have been reported since its first discovery in 2011 [13]. The extension of spectroscopic techniques developed in gas-phase HHG into solid-state systems may provide future tools to probe the electronic structure of insulators and semiconductors [61]. As solids possess a high density of electrons, it has been shown that the conversion rate of

HHG from solids is much higher than that of gas-phase materials [27, 34]. This may enable new table-top and functional light sources.

Understanding the solid-state HHG would also reveal the fundamental process important for future technological application. The ability to control optically induced ultrafast currents in solids, which was in fact demonstrated by Schiffrin [62], might lead to new ultrafast current switching methods by light. More recently, Mashiko *et al.* reported the observation of sub-femtosecond oscillating conductivity [63], which may be utilized for petahertz signal processing.

Understanding the excitation process induced by intense electric fields is also crucial for laser material processing [64–66]. The research on the interaction of intense electric field and solid-state materials have long been motivated by this field. In general, an intense laser field excites VB electrons, whose energy are subsequently transferred to lattice vibration, which finally leads to bond breakdown. As these processes are inherently multi-scale, from ultrafast initial electron excitation to final material breakdown with timescales spanning orders of magnitudes, as well as requiring knowledge of complex multi-physics involving light-matter interaction, electron-electron interaction, and electron-ion interaction, it has turned out to be a highly difficult scientific problem to reveal [64]. Thus, it is an important first step to understand the fundamental nature of the initial electron excitation dynamics, which triggers the complex subsequent processes.

The experimentally observed unique features of solid-state HHG require development of new methods and models which incorporate the intrinsic aspects of solids. In contrast to gas-phase isolated systems, solid-state systems are extended systems with many electrons in a periodic structure. Electrons moving in a periodic potential undergo Bloch oscillations, which have been considered as a possible radiation source of solid-state HHG [13, 27]. The periodicity, moreover, gives birth to the band structure, which must be taken into account to understand the electron dynamics underlying the solid-state HHG, as the importance of multiple bands has been pointed out [43, 53].

In the gas-phase HHG, the appearance of the semiclassical three-step model [21, 22] has boosted the understanding of the phenomena and has contributed to the developments of successful applications such as attosecond pulse generation [1–3] and coherent keV x-ray sources [4]. As the solid-state HHG is in its infancy, the mechanism of the phenomena is still under intensive discussions and a variety of models have been proposed. We need to build an essential and simple model which unifies the ideas discussed so far in the pioneering works, capable of explaining the unique features.

In a solid, an electron moves through the background of other nonlocalized electrons. The high density of electrons might affect the electron dynamics and alter it from what would be expected by the active single-electron picture, which has been proved to work in the case of gas-phase HHG. Indeed, in solid-state systems, the many-body effect causes a characteristic resonance, i.e., excitons, in the linear response regime. In the strong-field regime, Garg *et al.* have recently suggested that the strength of Coulomb interactions among electrons alters harmonic yields [30]. Thus, it should also be addressed whether or not we can rely on the independent electron approximation, which has been widely used in most previous studies of solid-state HHG [13, 27, 32–34, 37, 41, 42, 50, 55, 67, 68]. At present, the linear response with excitonic features is well described by the *ab-initio* Bethe-Salpeter equation [60] based on many-body perturbation theory (MBPT). It is, however, still a formidable task to describe highly nonlinear dynamics of extended systems within the framework of MBPT except for a few pioneering works [69, 70].

1.7 Objective

The interplay among a variety of possible effects in solids under strong fields yields not only new opportunities mentioned above, but also difficulties in revealing its essential physics. This dissertation is dedicated to approach this challenging problem through theoretical and numerical methods. In particular, we set two goals: (i) revealing essential electron dynamics behind HHG in solids and (ii) investigating the multielectron effect on the HHG processes. In order to realize these goals, we have (i) developed TDSE simulation methods within IEA to discuss the single-electron dynamics under an intense field and (ii) developed time-dependent Hartree-Fock (TDHF) simulation methods to reveal the effects of electron-hole interaction on HHG in solids. For both of these, we have employed 1D model systems to obtain heuristic results. Similar 1D models have previously been used in several works [43, 46, 52, 54], yielding useful results. In the IEA study, we have proposed a semiclassical momentum-space three-step model that incorporates vector-potential-induced intraband displacement, interband tunneling, and recombination with the VB hole, which is capable of explaining various aspects of solid-state HHG. In the time-dependent Hartree-Fock (TDHF) study, we have found qualitative changes in harmonic spectra from those of IEA, which can be understood in terms of electron-hole polarization.

This dissertation is composed of 6 chapters. Chapter 2 details the theoretical concepts necessary for our studies. Chapter 3 details the numerical methods used in our simulations. Chapter 4 presents the IEA study. Based on the simulated harmonic spectra, we propose and discuss the momentum-space three-step model, which well explains many features of the solid-state HHG. Chapter 5 presents the TDHF study. After discussing observed qualitative difference between TDHF and independent-electron simulations, we analyze the electron excitation process under the influence of electron-hole interaction based on the Houston basis [58, 71]. Chapter 6 summarizes this dissertation and discuss future prospects.

2

Theoretical Concepts

This chapter details the theoretical concepts used in this dissertation. In principle, we can obtain the full quantum dynamics of the many-electron system in solids by solving the many-body time-dependent Schrödinger equation. However, in practice, the direct calculation for solids is impossible due to diverging computational cost with the number of electrons. Therefore, we need to use approximate methods to describe the electron dynamics. I introduce two single-electron treatments that will be used in this dissertation: independent-electron approximation and time-dependent Hartree-Fock methods.

We employ the velocity gauge in order to make the Bloch's theorem available. Bloch's theorem offers us a substantial reduction of the problem size. The application of Bloch's theorem to independent-electron approximation and time-dependent Hartree-Fock are discussed.

In solid-state high-harmonic generation, field-induced current density is the physically relevant obserbable. We define the current density as the temporal derivative of the dipole moment, and derive a general formula to obtain it from time-dependent electron orbitals.

To analyze electron dynamics in solids driven by an intense field, it is convenient to use a time-dependent quantum basis set that adiabatically changes along with the field. The accelerated Bloch states, known as the Houston states, are such an adiabatic basis set. Their definition and fundamental properties will be discussed.

2.1 Many-body dynamics in solids

The quantum dynamics of the many-body electron system under an electric field $\boldsymbol{E}(t)$ is governed by the many-body TDSE,

$$i\frac{\partial}{\partial t}\Psi(t) = \hat{H}(t)\Psi(t). \tag{2.1}$$

Here, the many-body time-dependent Hamiltonian $\hat{H}(t)$ is given by

$$\hat{H}(t) = \hat{H}_1(t) + \hat{H}_2, \tag{2.2}$$

where the one-electron part is given by

$$\hat{H}_1(t) = \sum_i \hat{h}_1(\boldsymbol{r}_i, t), \tag{2.3}$$

and the interelectronic interaction part by

$$\hat{H}_2 = \frac{1}{2}\sum_{i\neq j} v(\boldsymbol{r}_i - \boldsymbol{r}_j), \tag{2.4}$$

with $v(\boldsymbol{r}-\boldsymbol{r}')=v(|\boldsymbol{r}-\boldsymbol{r}'|)$ denoting the Coulomb potential. $\hat{h}_1(\boldsymbol{r},t)$ in Eq. (2.3) is given by

$$\hat{h}_1(\boldsymbol{r},t)=\frac{\hat{\boldsymbol{p}}^2}{2}-\sum_I z_I v(\boldsymbol{r}-\boldsymbol{R}_I)+\boldsymbol{r}\cdot\boldsymbol{\mathcal{E}}(t) \tag{2.5}$$

in the length gauge, and

$$\hat{h}_1(\boldsymbol{r},t)=\frac{1}{2}\left[\boldsymbol{p}+\boldsymbol{A}(t)\right]^2-\sum_I z_I v(\boldsymbol{r}-\boldsymbol{R}_I) \tag{2.6}$$

in the velocity gauge, where

$$\boldsymbol{A}(t)=-\int^t \boldsymbol{\mathcal{E}}(t')dt' \tag{2.7}$$

is the vector potential. z_I and $\boldsymbol{R}_I$ denote the charge and the position of a nuclei labeled I, respectively.

Let me make a brief remark on the choice of the gauge. According to the gauge principle, we can obtain the same result for any physical observables by solving the many-body TDSE (2.1) in either the length gauge or the velocity gauge [72]. The many-body wavefunction $\Psi_L(t)$ in the length gauge and Ψ_V in the velocity gauge and the corresponding Hamiltonian can be converted into each other through the gauge transformation,

$$\Psi_V(t)=\hat{U}(t)\Psi_L(t), \tag{2.8}$$

$$\hat{H}_V(t)=\hat{U}(t)\hat{H}_L\hat{U}^\dagger(t)+i\frac{d\hat{U}(t)}{dt}\hat{U}^\dagger(t), \tag{2.9}$$

where

$$\hat{U}(t)=\exp\left(-i\boldsymbol{A}(t)\cdot\sum_i \boldsymbol{r}_i\right) \tag{2.10}$$

is the unitary transform operator. Although the length gauge has often been used in gas-phase strong-field calculations, it breaks the spatial periodicity of the Hamiltonian. The velocity gauge, on the other hand, preserves the spatial periodicity at any given time. This is a very preferable nature, as it allows us to employ Bloch's theorem. Hence, we adopt the velocity gauge in our calculations.

It should be also noted here that, in general, the electric field $\boldsymbol{E}(t)$ (and the corresponding vector potential $\boldsymbol{A}(t)$) can be a function of position $\boldsymbol{r}$, i.e., spatially inhomogeneous. In this thesis, however, we employ a dipole approximation to simplify the problem, assuming that the electron dynamics at macroscopically different positions are not coupled with each other [73].

For gas-phase isolated systems, several methods have been developed to solve the many-body TDSE (2.1) [51]. However, it is still a formidable task to solve the many-body TDSE (2.1) for many-electron systems in solids. The simplest approach is to treat a single electron in a potential that takes into consideration the interactions among electrons in some way.

We employ the IEA to reveal the independent electron processes underlying HHG (Ch. 4). In the IEA, one solves the effective single-electron TDSE for each electron orbital in a periodic system with an effective periodic potential $v_{\text{eff}}(\boldsymbol{r})$ which takes into account the potential from nuclei as well as some effects from other electrons. The IEA has been widely employed in the previous works [42, 43, 46, 50, 52–55] to describe HHG in solid-state materials.

In order to investigate the effects of electron-hole interaction, we need to go beyond the independent-electron picture. To attain this goal, we employ the TDHF method to describe HHG in solid-state materials from an interacting many-electron system in a solid. The TDHF method is considered as the minimal theory to deal with the electron-hole correlation, and thus serves as a benchmark for studies seeking to reveal many-body effects in ultrafast electron dynamics in solids.

2.1.1 Time-dependent Schrödinger equation within IEA

In the IEA, each electron orbital obeys the effective one-body TDSE

$$\begin{aligned} i\frac{\partial}{\partial t}\psi_i(\boldsymbol{r},t) &= \hat{h}(t)\psi_i(\boldsymbol{r},t) \\ &= \left\{\frac{1}{2}\left(\frac{\nabla}{i}+\boldsymbol{A}(t)\right)^2 + v_{\text{eff}}(\boldsymbol{r})\right\}\psi_i(\boldsymbol{r},t), \end{aligned} \tag{2.11}$$

where $v_{\text{eff}}(\boldsymbol{r})$ is a single-electron effective periodic potential which takes into account the potential from nucleus as well as some effects of interelectronic interaction. $\psi_i(\boldsymbol{r},t)$ is the time-dependent single-electron orbital whose initial state is $\phi_i(\boldsymbol{r})$, an eigenstate of the field-free Hamiltonian

$$\hat{h}_0 = -\frac{\nabla^2}{2} + v_{\text{eff}}(\boldsymbol{r}), \tag{2.12}$$

with eigenenergy ε_i. The ground state is found by occupying the lowest energy eigenstates $\phi_i(\boldsymbol{r})$ with obeying the Pauli exclusion principle. As the eigenstates of the effective single-electron Hamiltonian $\hat{h}_0$ are orthogonal, and the time evolution governed by the TDSE (2.11) preserves the orthogonality among orbitals, the antisymmetric many-body wavefunction can be constructed as a determinant of the orbitals.

2.1.2 Time-dependent Hartree-Fock (TDHF) theory

The TDHF theory assumes that the time-dependent many-body wavefunction $\Psi(t)$ is a single Slater determinant of time-dependent electron orbitals $\psi_i(t)$ at every instant in time [71]. The equation of motion (EoM) for each of the orbitals can be obtained via the time-dependent variational principle [74, 75],

$$\delta\left[\int dt\,\langle\Psi|\left(\hat{H} - i\frac{\partial}{\partial t}\right)|\psi\rangle\right] = 0. \tag{2.13}$$

The spin-restricted TDHF equations in the velocity gauge for an electron orbital ψ_i can be obtained as,

$$\begin{aligned} i\frac{\partial}{\partial t}\psi_i(\boldsymbol{r},t) &= \hat{h}(t)\psi_i(\boldsymbol{r},t) \\ &= \left[\frac{1}{2}\left(\frac{\nabla}{i}+\boldsymbol{A}(t)\right)^2 + v_1(\boldsymbol{r}) + \hat{w}[\rho(t)]\right]\psi_i(\boldsymbol{r},t), \end{aligned} \tag{2.14}$$

where $v_1(\boldsymbol{r})$ represents the periodic potential from the crystal nuclei,

$$v_1(\boldsymbol{r}) = -\sum_I z_I v(\boldsymbol{r}-\boldsymbol{R}_I), \tag{2.15}$$

$\rho(t)$ the density matrix,

$$\rho(\boldsymbol{r},\boldsymbol{r}',t) = 2\sum_i \psi_i(\boldsymbol{r},t)\,\psi_i^*(\boldsymbol{r}',t), \tag{2.16}$$

and the operator $\hat{w}[\rho]$ the contribution from the interelectronic Coulomb interactions, composed of the Hartree and exchange terms,

$$w[\rho](\boldsymbol{r},\boldsymbol{r}') = v_{\mathrm{H}}[\rho](\boldsymbol{r})\delta(\boldsymbol{r}-\boldsymbol{r}') + v_{\mathrm{x}}[\rho](\boldsymbol{r},\boldsymbol{r}'), \tag{2.17}$$

$$v_{\mathrm{H}}[\rho](\boldsymbol{r}) = \int d\boldsymbol{r}''\rho(\boldsymbol{r}'',\boldsymbol{r}'')v(\boldsymbol{r}-\boldsymbol{r}''), \tag{2.18}$$

$$v_{\mathrm{x}}[\rho](\boldsymbol{r},\boldsymbol{r}') = -\frac{1}{2}\rho(\boldsymbol{r},\boldsymbol{r}')v(\boldsymbol{r}-\boldsymbol{r}'). \tag{2.19}$$

Note that the operation of the operator $\hat{w}[\rho]$ on an orbital $\psi_i(\boldsymbol{r},t)$ is represented as matrix operation in the spatial basis:

$$\left[\hat{w}[\rho]\psi_i(t)\right](\boldsymbol{r}) = \int w[\rho](\boldsymbol{r},\boldsymbol{r}')\psi_i(\boldsymbol{r}',t)d\boldsymbol{r}'. \tag{2.20}$$

The initial state of $\psi_i(\boldsymbol{r})$ is given by the self-consistent eigenstate $\phi_i(\boldsymbol{t},t)$ of the field-free Hartree-Fock Hamiltonian,

$$\hat{h}_0 = -\frac{\nabla^2}{2} + v_1(\boldsymbol{r}) + \hat{w}[\rho_0] \tag{2.21}$$

with $\rho_0(\boldsymbol{r},\boldsymbol{r}') = 2\sum_i \phi_i(\boldsymbol{r})\phi_i^*(\boldsymbol{r}')$.

2.2 Bloch's theorem

Here, let us see how we can take advantage of Bloch's theorem possible due to our employment of the velocity gauge. As seen above, we treat a time-dependent Schrödinger-like equation,

$$i\frac{\partial}{\partial t}\psi_i(\boldsymbol{r},t) = \hat{h}(t)\psi_i(\boldsymbol{r},t) = \int d\boldsymbol{r}' h(\boldsymbol{r},\boldsymbol{r}',t)\psi_i(\boldsymbol{r}',t), \tag{2.22}$$

$$\begin{aligned} &h(\boldsymbol{r},\boldsymbol{r}',t) \\ &= \left[\frac{1}{2}\left(\frac{\nabla}{i} + \boldsymbol{A}(t)\right)^2 + v_{\mathrm{l}}(\boldsymbol{r})\right]\delta(\boldsymbol{r}-\boldsymbol{r}') + v_{\mathrm{nl},\boldsymbol{A}(t)}(\boldsymbol{r},\boldsymbol{r}') + v_{\mathrm{x}}[\rho(t)](\boldsymbol{r},\boldsymbol{r}'), \end{aligned} \tag{2.23}$$

where $v_{\mathrm{l}}(\boldsymbol{r})$ and $v_{\mathrm{nl},\boldsymbol{A}(t)}(\boldsymbol{r},\boldsymbol{r}')$ are general spatially local and nonlocal potentials in the velocity gauge, respectively. $v_{\mathrm{x}}[\rho(t)](\boldsymbol{r},\boldsymbol{r}')$ is the exchange potential defined in Eq. (2.17). By representing the Hamiltonian operation as a form of matrix operation in the coordinate space like Eq. (2.22), we can deal with both the local and nonlocal potential at the same time. I note that the nonlocal potential $v_{\mathrm{nl},\boldsymbol{A}(t)}(\boldsymbol{r},\boldsymbol{r}')$ has a dependency on the vector potential $\boldsymbol{A}(t)$ due to the gauge transformation from the length gauge; if a nonlocal potential in the length gauge is given by

$$v_{\mathrm{nl}}(\boldsymbol{r},\boldsymbol{r}'), \tag{2.24}$$

then it is transformed into

$$v_{\mathrm{nl},\boldsymbol{A}(t)}(\boldsymbol{r},\boldsymbol{r}') = e^{-i\boldsymbol{A}(t)\cdot\boldsymbol{r}}v_{\mathrm{nl}}(\boldsymbol{r},\boldsymbol{r}')e^{i\boldsymbol{A}(t)\cdot\boldsymbol{r}'}, \tag{2.25}$$

in the velocity gauge[1]. Finally, we normalize each of the electron orbitals as

$$\int d\boldsymbol{r}|\psi_i(\boldsymbol{r},t)|^2 = 1. \tag{2.26}$$

Because the velocity gauge preserves the spatial periodicity of the Hamiltonian, if all of the local, nonlocal, and exchange operators are spatially periodic, we can generalize Bloch's theorem for time-dependent wave functions. Precisely speaking, the spatial periodicity of the operators is defined as that each of the operators in the length gauge is invariant under a globally spatial translation with an arbitrary lattice vector $\boldsymbol{T}$,

$$v_{\mathrm{l}}(\boldsymbol{r}+\boldsymbol{T}) = v_{\mathrm{l}}(\boldsymbol{r}), \tag{2.27}$$
$$v_{\mathrm{nl}}(\boldsymbol{r}+\boldsymbol{T},\boldsymbol{r}'+\boldsymbol{T}) = v_{\mathrm{nl}}(\boldsymbol{r},\boldsymbol{r}'), \tag{2.28}$$
$$v_{\mathrm{x}}[\rho(t)](\boldsymbol{r}+\boldsymbol{T},\boldsymbol{r}'+\boldsymbol{T}) = v_{\mathrm{x}}[\rho(t)](\boldsymbol{r},\boldsymbol{r}'). \tag{2.29}$$

If they are spatially periodic in the length gauge, they also keep their periodicity in the velocity gauge. The local potential $v_{\mathrm{l}}(\boldsymbol{r})$ and the exchange potential $v_{\mathrm{x}}[\rho(t)](\boldsymbol{r},\boldsymbol{r}')$ retain their global periodicity in the velocity gauge. Moreover, the nonlocal potential $v_{\mathrm{nl},\boldsymbol{A}(t)}(\boldsymbol{r},\boldsymbol{r}')$ also keeps its periodicity in the velocity gauge, because

$$v_{\mathrm{nl},\boldsymbol{A}(t)}(\boldsymbol{r}+\boldsymbol{T},\boldsymbol{r}'+\boldsymbol{T}) = e^{-i\boldsymbol{A}(t)\cdot(\boldsymbol{r}+\boldsymbol{T})}v_{\mathrm{nl}}(\boldsymbol{r},\boldsymbol{r}')e^{i\boldsymbol{A}(t)\cdot(\boldsymbol{r}'+\boldsymbol{T})} = v_{\mathrm{nl},\boldsymbol{A}(t)}(\boldsymbol{r},\boldsymbol{r}'). \tag{2.30}$$

Therefore, if all of the local, nonlocal, and exchange operators are spatially periodic, the Hamiltonian in the velocity gauge is invariant under the global translation with lattice vector $\boldsymbol{T}$,

$$h(\boldsymbol{r}+\boldsymbol{T},\boldsymbol{r}'+\boldsymbol{T},t) = h(\boldsymbol{r},\boldsymbol{r}',t), \tag{2.31}$$

at any time t.

According to Bloch's theorem, an electron orbital function can be decomposed into the product of a plain wave and a lattice periodic function,

$$\psi_i(\boldsymbol{r},t) \to \psi_{\lambda,\boldsymbol{k}}(\boldsymbol{r},t) = \frac{1}{\sqrt{N_k}}e^{i\boldsymbol{k}\cdot\boldsymbol{r}}u_{\lambda,\boldsymbol{k}}(\boldsymbol{r},t), \tag{2.32}$$

where N_k denotes the total number of k-points and $u_{\lambda,\boldsymbol{k}}(\boldsymbol{r},t)$ satisfies

$$u_{\lambda,\boldsymbol{k}}(\boldsymbol{r}+\boldsymbol{T},t) = u_{\lambda,\boldsymbol{k}}(\boldsymbol{r},t). \tag{2.33}$$

Here, λ and $\boldsymbol{k}$ represent the band index and the crystal momentum, respectively. The factor $1/\sqrt{N_k}$ is introduced to normalize $u_{\lambda,\boldsymbol{k}}(\boldsymbol{r},t)$ in a unit cell,

$$\int_\Omega d\boldsymbol{r}|u_{\lambda,\boldsymbol{k}}(\boldsymbol{r},t)|^2 = 1, \tag{2.34}$$

where hereafter $\int_\Omega d\boldsymbol{r}$ represents an integral within a unit cell. Inserting this ansatz (2.32) into the TDSE

[1] Although the exchange operator $v_{\mathrm{x}}[\rho(t)](\boldsymbol{r},\boldsymbol{r}')$ is also a nonlocal operator, it does not need the factors $e^{-i\boldsymbol{A}(t)\cdot\boldsymbol{r}}$ and $e^{i\boldsymbol{A}(t)\cdot\boldsymbol{r}'}$ because they are canceled out by the factors from the density matrix $\rho(\boldsymbol{r},\boldsymbol{r}',t)$ in the gauge transformation.

(2.22) yields the EoM for $u_{\lambda,\boldsymbol{k}}(\boldsymbol{r},t)$

$$\begin{aligned} i\frac{\partial}{\partial t}u_{\lambda,\boldsymbol{k}}(\boldsymbol{r},t) &= \int_\Omega d\boldsymbol{r}' h_{\boldsymbol{k}}(\boldsymbol{r},\boldsymbol{r}',t)u_{\lambda,\boldsymbol{k}}(\boldsymbol{r}',t) \\ &= \left[\frac{1}{2}\left(\frac{\nabla}{i}+\boldsymbol{k}+\boldsymbol{A}(t)\right)^2 + v_{\text{l}}(\boldsymbol{r})\right]u_{\lambda,\boldsymbol{k}}(\boldsymbol{r},t) \\ &\quad + \int_\Omega [v^\Omega_{\text{nl},\boldsymbol{k}+\boldsymbol{A}(t)}(\boldsymbol{r},\boldsymbol{r}') + v^\Omega_{\text{x},\boldsymbol{k}}[\rho(t)](\boldsymbol{r},\boldsymbol{r}')]u_{\lambda,\boldsymbol{k}}(\boldsymbol{r}',t)d\boldsymbol{r}', \end{aligned} \tag{2.35}$$

where,

$$\begin{aligned} &h_{\boldsymbol{k}}(\boldsymbol{r},\boldsymbol{r}',t) \\ &= \left[\frac{1}{2}\left(\frac{\nabla}{i}+\boldsymbol{k}+\boldsymbol{A}(t)\right)^2 + v_{\text{l}}(\boldsymbol{r})\right]\delta(\boldsymbol{r}-\boldsymbol{r}') + v^\Omega_{\text{nl},\boldsymbol{k}+\boldsymbol{A}(t)}(\boldsymbol{r},\boldsymbol{r}') + v^\Omega_{\text{x},\boldsymbol{k}}[\rho(t)](\boldsymbol{r},\boldsymbol{r}'), \end{aligned} \tag{2.36}$$

$$v^\Omega_{\text{nl},\boldsymbol{k}+\boldsymbol{A}(t)}(\boldsymbol{r},\boldsymbol{r}') = \sum_{\boldsymbol{T}} e^{-i(\boldsymbol{k}+\boldsymbol{A}(t))\cdot\boldsymbol{r}} v_{\text{nl}}(\boldsymbol{r},\boldsymbol{r}'+\boldsymbol{T})e^{i(\boldsymbol{k}+\boldsymbol{A}(t))\cdot(\boldsymbol{r}'+\boldsymbol{T})}, \tag{2.37}$$

$$v^\Omega_{\text{x},\boldsymbol{k}}[\rho(t)](\boldsymbol{r},\boldsymbol{r}') = \sum_{\boldsymbol{T}} e^{-i\boldsymbol{k}\cdot\boldsymbol{r}} v_{\text{x}}(\boldsymbol{r},\boldsymbol{r}'+\boldsymbol{T})e^{i\boldsymbol{k}\cdot(\boldsymbol{r}'+\boldsymbol{T})}. \tag{2.38}$$

Equations (2.35) and (2.36) are the fundamental equations to be solved. As calculations take place in a single unit cell, it can be seen that the problem size has been substantially reduced.

2.2.1 Bloch's theorem for IEA

As the single-electron effective potential $v_{\text{eff}}(\boldsymbol{r})$ in the TDSE within IEA Eq. (2.11) is periodic, we can apply Bloch's theorem. Then, the time-dependent orbital can be labeled by the band λ and the crystal momentum $\boldsymbol{k}$, i.e., $\psi_i(\boldsymbol{r},t) \to \psi_{\lambda,\boldsymbol{k}}(\boldsymbol{r},t)$, and we have

$$\begin{aligned} i\frac{\partial}{\partial t}\psi_{b,\boldsymbol{k}_0}(\boldsymbol{r},t) &= \hat{h}(t)\psi_{b,\boldsymbol{k}_0}(\boldsymbol{r},t) \\ &= \left\{\frac{1}{2}\left(\frac{\nabla}{i}+\boldsymbol{A}(t)\right)^2 + v_{\text{eff}}(\boldsymbol{r})\right\}\psi_{b,\boldsymbol{k}_0}(\boldsymbol{r},t), \end{aligned} \tag{2.39}$$

for an electron which initially lies in band b with a crystal momentum $\boldsymbol{k}_0$. The initial state is the Bloch function $\phi_{b,\boldsymbol{k}_0}(\boldsymbol{r})$, an eigenstate of the field-free Hamiltonian $\hat{h}_0$,

$$\hat{h}_0\phi_{b,\boldsymbol{k}_0} = \varepsilon_{b,\boldsymbol{k}_0}\phi_{b,\boldsymbol{k}_0}, \tag{2.40}$$

with $\varepsilon_{b,\boldsymbol{k}_0}$ being its energy eigenvalue. By decomposing the orbital into the product of a plain wave and a lattice periodic function, i.e., $\psi_{\lambda,\boldsymbol{k}}(\boldsymbol{r},t) = e^{i\boldsymbol{k}\cdot\boldsymbol{r}}u_{\lambda,\boldsymbol{k}}(\boldsymbol{r},t)$, and applying the discussion above, we have

$$i\frac{\partial}{\partial t}u_{b,\boldsymbol{k}_0}(\boldsymbol{r},t) = \left\{\frac{1}{2}\left[\frac{\nabla}{i}+\boldsymbol{k}_0+\boldsymbol{A}(t)\right]^2 + v_{\text{eff}}(\boldsymbol{r})\right\}u_{b,\boldsymbol{k}_0}(\boldsymbol{r},t). \tag{2.41}$$

Because the Hamiltonian $\hat{h}(t)$ retains the lattice periodicity at each time due to the choice of the velocity gauge, the initial crystal momentum $\boldsymbol{k}_0$ is always a good quantum number. Therefore, one can solve the TDSE (2.41) for each $\boldsymbol{k}_0$ independently.

2.2.2 Bloch's theorem for TDHF

The TDHF Hamiltonian also possesses a global spatial periodicity, so we can apply Bloch's theorem. The spin-restricted TDHF equations in the velocity gauge for an electron orbital $\psi_{b,\boldsymbol{k}_0}$ that *initially* lies in band b with crystal momentum $\boldsymbol{k}_0$ can be obtained as,

$$\begin{aligned} i\frac{\partial}{\partial t}\psi_{b,\boldsymbol{k}_0}(\boldsymbol{r},t) &= \hat{h}(t)\psi_{b,\boldsymbol{k}_0}(\boldsymbol{r},t) \\ &= \left[\frac{1}{2}\left(\frac{\nabla}{i}+\boldsymbol{A}(t)\right)^2 + v_1(\boldsymbol{r}) + \hat{w}[\rho(t)]\right]\psi_{b,\boldsymbol{k}_0}(\boldsymbol{r},t), \end{aligned} \tag{2.42}$$

where the density matrix is given by

$$\rho(\boldsymbol{r},\boldsymbol{r}',t) = 2\sum_{b\in\mathrm{VB},\ \boldsymbol{k}_0}\psi_{b,\boldsymbol{k}_0}(\boldsymbol{r},t)\,\psi^*_{b,\boldsymbol{k}_0}(\boldsymbol{r}',t). \tag{2.43}$$

The initial state of $\psi_{b,\boldsymbol{k}_0}(\boldsymbol{r},t)$ is the VB Bloch function $\phi_{b,\boldsymbol{k}_0}(\boldsymbol{r})$, obtained as a self-consistent eigenstate of the field-free Hartree-Fock Hamiltonian Eq. (2.21) with an energy eigenvalue $\varepsilon_{b,\boldsymbol{k}_0}$.

When we decompose the time-dependent orbital $\psi_{b,\boldsymbol{k}}(\boldsymbol{r},t) = e^{i\boldsymbol{k}\cdot\boldsymbol{r}}u_{b,\boldsymbol{k}}(\boldsymbol{r},t)$, the EoM for the lattice periodic function $u_{b,\boldsymbol{k}}(\boldsymbol{r},t)$ is given by

$$\begin{aligned} i\frac{\partial}{\partial t}u_{b,\boldsymbol{k}_0}(\boldsymbol{r},t) = &\left[\frac{1}{2}\left(\frac{\nabla}{i}+\boldsymbol{k}_0+\boldsymbol{A}(t)\right)^2 + v_1(\boldsymbol{r}) + v_{\mathrm{H}}[\rho(t)](\boldsymbol{r})\right]u_{\lambda,\boldsymbol{k}_0}(\boldsymbol{r},t) \\ &+\int_\Omega v^\Omega_{\mathrm{x},\boldsymbol{k}_0}[\rho(t)](\boldsymbol{r},\boldsymbol{r}')u_{\lambda,\boldsymbol{k}_0}(\boldsymbol{r}',t). \end{aligned} \tag{2.44}$$

Here, the Hartree term $v_{\mathrm{H}}[\rho(t)](\boldsymbol{r})$ is given by

$$\begin{aligned} v_{\mathrm{H}}[\rho(t)](\boldsymbol{r}) &= \int d\boldsymbol{r}'\rho(\boldsymbol{r}',\boldsymbol{r}',t)v(\boldsymbol{r}-\boldsymbol{r}') \\ &= \frac{2}{N_k}\sum_{b',\boldsymbol{k}'_0}\int d\boldsymbol{r}'|u_{b',\boldsymbol{k}'_0}(\boldsymbol{r}',t)|^2 v(\boldsymbol{r}-\boldsymbol{r}') \\ &= \frac{2}{N_k}\sum_{b',\boldsymbol{k}'_0}\sum_{\boldsymbol{T}}\int_\Omega d\boldsymbol{r}'|u_{b',\boldsymbol{k}'_0}(\boldsymbol{r}'+\boldsymbol{T},t)|^2 v(\boldsymbol{r}-\boldsymbol{r}'-\boldsymbol{T}) \\ &= 2\sum_{b',\boldsymbol{k}'_0}\int_\Omega d\boldsymbol{r}'|u_{b',\boldsymbol{k}'_0}(\boldsymbol{r}',t)|^2 v^\Omega_0(\boldsymbol{r}-\boldsymbol{r}'), \end{aligned} \tag{2.45}$$

and the reduced exchange term $v^\Omega_{\mathrm{x},\boldsymbol{k}}[\rho(t)](\boldsymbol{r},\boldsymbol{r}')$ by,

$$\begin{aligned} v^\Omega_{\mathrm{x},\boldsymbol{k}}[\rho(t)](\boldsymbol{r},\boldsymbol{r}') &= -\frac{1}{2}\sum_{\boldsymbol{T}}e^{-i\boldsymbol{k}\cdot\boldsymbol{r}}\rho(\boldsymbol{r},\boldsymbol{r}'+\boldsymbol{T},t)v(\boldsymbol{r}-\boldsymbol{r}'-\boldsymbol{T})e^{i\boldsymbol{k}\cdot(\boldsymbol{r}'+\boldsymbol{T})} \\ &= -\frac{1}{N_k}\sum_{b',\boldsymbol{k}'}\sum_{\boldsymbol{T}}u_{b',\boldsymbol{k}'}(\boldsymbol{r},t)u^*_{b',\boldsymbol{k}'}(\boldsymbol{r}'+\boldsymbol{T},t)e^{-i(\boldsymbol{k}-\boldsymbol{k}')\cdot(\boldsymbol{r}-\boldsymbol{r}'-\boldsymbol{T})}v(\boldsymbol{r}-\boldsymbol{r}'-\boldsymbol{T}) \\ &= -\sum_{b',\boldsymbol{k}'}u_{b',\boldsymbol{k}'}(\boldsymbol{r},t)u^*_{b',\boldsymbol{k}'}(\boldsymbol{r}',t)v^\Omega_{\boldsymbol{k}-\boldsymbol{k}'}(\boldsymbol{r}-\boldsymbol{r}'), \end{aligned} \tag{2.46}$$

where $v^\Omega_{\boldsymbol{k}}(\boldsymbol{r})$ is defined as

$$v^\Omega_{\boldsymbol{k}}(\boldsymbol{r}) = \frac{1}{N_k}\sum_{\boldsymbol{T}}v(\boldsymbol{r}+\boldsymbol{T})e^{-i\boldsymbol{k}\cdot(\boldsymbol{r}+\boldsymbol{T})}. \tag{2.47}$$

2.3 Current

We calculate the HHG spectrum as the modulus square of the Fourier transform of the induced current $\boldsymbol{j}(t)$. The current is defined as the temporal derivative of the expectation value of the position operator

$$\boldsymbol{j}(t) = \frac{1}{V}\frac{d}{dt}\langle\hat{\boldsymbol{r}}\rangle = \frac{1}{V}\frac{1}{i}\langle[\hat{\boldsymbol{r}}, \hat{h}]\rangle\,, \tag{2.48}$$

where $\hat{h}$ is the Hamiltonian considered at present, and V denotes the volume of the system. If the Hamiltonian consists of only a kinetic operator $\hat{\boldsymbol{p}} + \boldsymbol{A}(t)$ and a spatially local operator $v_{\mathrm{l}}(\boldsymbol{r})$, Eq. (2.48) leads to a familiar form

$$\boldsymbol{j}_{\mathrm{l}}(t) = \frac{1}{V}\langle\hat{\boldsymbol{p}} + \boldsymbol{A}(t)\rangle\,. \tag{2.49}$$

If $\hat{h}$ contains a spatially non-local operator $v_{\mathrm{nl}}(\boldsymbol{r}, \boldsymbol{r}')$, however, the formula needs an additional term,

$$\boldsymbol{j}(t) = \boldsymbol{j}_{\mathrm{l}}(t) + \frac{1}{V}\frac{1}{i}\langle[\hat{\boldsymbol{r}}, \hat{v}_{\mathrm{nl}}]\rangle\,. \tag{2.50}$$

One should be careful when evaluating $\boldsymbol{j}(t)$ when the Hamiltonian includes the non-local operators due to its noncommutative nature with the position operator.

2.3.1 Current in the IEA

In the IEA, the current is given by

$$\boldsymbol{j}(t) = \frac{1}{V}\langle\hat{\boldsymbol{p}} + \boldsymbol{A}(t)\rangle = \frac{2}{V}\sum_{b,\boldsymbol{k}_0}\boldsymbol{j}_{b,\boldsymbol{k}_0}(t), \tag{2.51}$$

where

$$\boldsymbol{j}_{b,\boldsymbol{k}_0}(t) = \int \psi^*_{b,\boldsymbol{k}_0}(\boldsymbol{r})\left(\frac{\nabla}{i} + \boldsymbol{A}(t)\right)\psi_{b,\boldsymbol{k}_0}(\boldsymbol{r})d\boldsymbol{r} \tag{2.52}$$

$$= \int_\Omega u^*_{b,\boldsymbol{k}_0}(\boldsymbol{r})\left(\frac{\nabla}{i} + \boldsymbol{k}_0 + \boldsymbol{A}(t)\right)u_{b,\boldsymbol{k}_0}(\boldsymbol{r})d\boldsymbol{r} \tag{2.53}$$

represents the contribution from each orbital.

2.3.2 Current in the TDHF

As the exchange operator in the TDHF Hamiltonian is spatially non-local, its contribution to the current may not be trivial. It can be shown that, however, its contribution vanishes in the TDHF theory. Let us consider the expectation value of the commutation of the position operator and the exchange operator $v_{\mathrm{x}}(\boldsymbol{r}, \boldsymbol{r}') = -\rho(\boldsymbol{r}, \boldsymbol{r}')v(\boldsymbol{r} - \boldsymbol{r}')/2$:

$$\begin{aligned}&\langle[\hat{\boldsymbol{r}}, \hat{v}_{\mathrm{x}}]\rangle \\ &= -\frac{1}{2}\int d\boldsymbol{r}'\int d\boldsymbol{r}\rho(\boldsymbol{r}', \boldsymbol{r}, t)[\boldsymbol{r}\rho(\boldsymbol{r}, \boldsymbol{r}', t)v(\boldsymbol{r} - \boldsymbol{r}') - \rho(\boldsymbol{r}, \boldsymbol{r}', t)v(\boldsymbol{r} - \boldsymbol{r}')\boldsymbol{r}']\end{aligned} \tag{2.54}$$

Using the invariant properties of the Coulomb potential $v(\boldsymbol{r}-\boldsymbol{r}')$ in regards to the exchange of $\boldsymbol{r}$ and $\boldsymbol{r}'$, namely, $v(\boldsymbol{r}-\boldsymbol{r}')=v(\boldsymbol{r}'-\boldsymbol{r})$,

$$\begin{aligned}&\langle[\hat{\boldsymbol{r}},\hat{v}_{\mathrm{x}}]\rangle\\&=-\frac{1}{2}\int d\boldsymbol{r}'\int d\boldsymbol{r}\left[\rho(\boldsymbol{r}',\boldsymbol{r},t)\boldsymbol{r}\rho(\boldsymbol{r},\boldsymbol{r}',t)v(\boldsymbol{r}-\boldsymbol{r}')-\rho(\boldsymbol{r}',\boldsymbol{r},t)\rho(\boldsymbol{r},\boldsymbol{r}',t)v(\boldsymbol{r}-\boldsymbol{r}')\boldsymbol{r}\right]\\&=0.\end{aligned} \tag{2.55}$$

The contribution from the exchange operator is always zero. As a consequence, we obtain the same form of current as in the IEA,

$$\boldsymbol{j}(t)=\frac{1}{V}\langle\hat{\boldsymbol{p}}+\boldsymbol{A}(t)\rangle=\frac{2}{V}\sum_{b,\boldsymbol{k}_0}\boldsymbol{j}_{b,\boldsymbol{k}_0}(t), \tag{2.56}$$

$$\boldsymbol{j}_{b,\boldsymbol{k}_0}(t)=\int\psi^*_{b,\boldsymbol{k}_0}(\boldsymbol{r})\left(\frac{\nabla}{i}+\boldsymbol{A}(t)\right)\psi_{b,\boldsymbol{k}_0}(\boldsymbol{r})d\boldsymbol{r} \tag{2.57}$$

$$=\int_\Omega u^*_{b,\boldsymbol{k}_0}(\boldsymbol{r})\left(\frac{\nabla}{i}+\boldsymbol{k}_0+\boldsymbol{A}(t)\right)u_{b,\boldsymbol{k}_0}(\boldsymbol{r})d\boldsymbol{r}. \tag{2.58}$$

2.4 General aspects of field-induced electron dynamics in solids

In this section, let us consider the general properties of electron dynamics in a periodic potential under a strong electric field, governed by a single-electron TDSE,

$$i\frac{\partial}{\partial t}\psi_{b,\boldsymbol{k}_0}(\boldsymbol{r},t)=\left[\frac{1}{2}\left(\frac{\nabla}{i}+\boldsymbol{A}(t)\right)^2+v_1(\boldsymbol{r})\right]\psi_{b,\boldsymbol{k}_0}(\boldsymbol{r},t). \tag{2.59}$$

It is convenient to use the instantaneous eigenstates as a basis, that is, a time-dependent basis of electron states that adiabatically follows the electric field. In the velocity gauge, the accelerated Bloch states play this role, which is also known as the Houston states [58, 71].

Let's start from a Bloch state, the eigenstate of a field-free Hamiltonian,

$$\left[-\frac{\nabla^2}{2}+v_1(\boldsymbol{r})\right]\phi_{\lambda,\boldsymbol{k}_0}=\varepsilon_{\lambda,\boldsymbol{k}_0}\phi_{\lambda,\boldsymbol{k}_0}(\boldsymbol{r}), \tag{2.60}$$

where $\phi_{\lambda,\boldsymbol{k}_0}(\boldsymbol{r})$ can be decomposed as $\phi_{\lambda,\boldsymbol{k}_0}(\boldsymbol{r})=e^{i\boldsymbol{k}_0\cdot\boldsymbol{r}}u^0_{\lambda,\boldsymbol{k}_0}(\boldsymbol{r})$. Let's consider the instantaneous eigenstate under an electric field,

$$\left[\frac{1}{2}\left(\frac{\nabla}{i}+\boldsymbol{A}(t)\right)^2+v_1(\boldsymbol{r})\right]\tilde{\phi}_{\lambda,\boldsymbol{k}_0}(\boldsymbol{r},t)=\tilde{\varepsilon}_{\lambda,\boldsymbol{k}_0}(t)\tilde{\phi}_{\lambda,\boldsymbol{k}_0}(\boldsymbol{r},t). \tag{2.61}$$

The solution of Eq. (2.61) under periodic boundary conditions, or the Born-von Kàrmàn boundary conditions, is given by,

$$\tilde{\phi}_{\lambda,\boldsymbol{k}_0}(\boldsymbol{r},t)=e^{-i\boldsymbol{A}(t)\cdot\boldsymbol{r}}\phi_{\lambda,\boldsymbol{k}(t)}(\boldsymbol{r}),\quad\tilde{\varepsilon}_{\lambda,\boldsymbol{k}_0}(t)=\varepsilon_{\lambda,\boldsymbol{k}(t)}, \tag{2.62}$$

where the time-dependent crystal momentum $\boldsymbol{k}(t)$ is defined as,

$$\boldsymbol{k}(t)=\boldsymbol{k}_0+\boldsymbol{A}(t). \tag{2.63}$$

Note that $\boldsymbol{k}(t)$ satisfies the acceleration theorem $\dot{\boldsymbol{k}} = -\boldsymbol{\mathcal{E}}(t)$ [71, 76]. This state $\tilde{\phi}_{\lambda,\boldsymbol{k}_0}(\boldsymbol{r},t)$ is called the accelerated Bloch state or the Houston state[2] [58, 71].

2.4.1 Electron dynamics in a strong field

We expand a time-dependent electron orbital initially at $\boldsymbol{k}_0$ with the Houston basis

$$\psi_{b,\boldsymbol{k}_0}(\boldsymbol{r},t) = \sum_{\mu} a^{\mu}_{b,\boldsymbol{k}_0}(t) e^{-i\int_0^t \varepsilon_{\mu,\boldsymbol{k}(t')}dt'} \tilde{\phi}_{\mu,\boldsymbol{k}_0}(\boldsymbol{r},t), \tag{2.64}$$

with the initial condition

$$a^{\lambda}_{b,k_0}(t=0) = \begin{cases} 1 & (\lambda = b) \\ 0 & (\lambda \neq b). \end{cases} \tag{2.65}$$

Inserting Eq. (2.64) into Eq. (2.59) yields the set of differential equations for the complex amplitudes:

$$i\frac{\partial}{\partial t} a^{\lambda}_{b,\boldsymbol{k}_0}(t) = \sum_{\mu} \boldsymbol{\mathcal{E}}(t)\cdot\boldsymbol{\xi}_{\lambda\mu}(\boldsymbol{k}(t)) e^{i\int_0^t \Delta\varepsilon_{\lambda\mu}(\boldsymbol{k}(t'))dt'} a^{\mu}_{b,\boldsymbol{k}_0}(t). \tag{2.66}$$

We define

$$\Delta\varepsilon_{\lambda\lambda'}(\boldsymbol{k}) = \varepsilon_{\lambda,\boldsymbol{k}} - \varepsilon_{\lambda',\boldsymbol{k}} \tag{2.67}$$

as the energy difference between band λ and λ' at crystal momentum $\boldsymbol{k}$, and

$$\begin{aligned} \boldsymbol{\xi}_{\lambda\lambda'}(\boldsymbol{k}) &= i\langle u^0_{\lambda,\boldsymbol{k}} | \nabla_{\boldsymbol{k}} u^0_{\lambda',\boldsymbol{k}} \rangle \\ &= i\int_{\Omega} u^{0*}_{\lambda,\boldsymbol{k}}(\boldsymbol{r}) \nabla_{\boldsymbol{k}} u^0_{\lambda',\boldsymbol{k}}(\boldsymbol{r}) d\boldsymbol{r}. \end{aligned} \tag{2.68}$$

Note that the relationship between $\boldsymbol{\xi}_{\lambda\lambda'}(\boldsymbol{k})$ and the matrix elements of the momentum operator $\boldsymbol{p}^{\lambda\lambda'}_{\boldsymbol{k}}$ is given by [77]

$$\boldsymbol{\xi}_{\lambda\neq\lambda'}(\boldsymbol{k}) = \frac{i\boldsymbol{p}^{\lambda\lambda'}_{\boldsymbol{k}}}{\Delta\varepsilon_{\lambda\lambda'}(\boldsymbol{k})}. \tag{2.69}$$

This formula is valid as long as $\Delta\varepsilon_{\lambda\lambda'}(\boldsymbol{k})$ in the denominator is not zero.

Intraband acceleration

It is trivial that the right-hand side of Eq. (2.66) is zero when $\boldsymbol{\mathcal{E}}(t) = 0$, the case of no field. Moreover, it is also zero in the free electron case, because $\boldsymbol{\xi}_{\lambda\lambda'}(\boldsymbol{k}) = 0$. Thus, without the periodic lattice potential of the crystal, the electron continues to stay within the initial band, and dose not undergo interband transitions. The solution for the free electron case is reduced to the Volkov states [25].

Even if neither of $\boldsymbol{\mathcal{E}}(t)$ nor $\boldsymbol{\xi}_{\lambda\lambda'}(\boldsymbol{k})$ are zero, as long as their product is small, the right-hand side of Eq. (2.66) remains quite small and excitation from the populated band to the upper band is suppressed: $a^{\lambda}_{b,k_0}(t) \approx a^{\lambda}_{b,k_0}(t=0)$. In that case, the electron state starting from $\phi_{b,\boldsymbol{k}_0}$ is given by

$$\psi_{b,\boldsymbol{k}_0}(\boldsymbol{r},t) = e^{-i\int_0^t \varepsilon_{b,\boldsymbol{k}(t')}dt'} \tilde{\phi}_{b,\boldsymbol{k}_0}(\boldsymbol{r},t) = e^{-i\int_0^t \varepsilon_{b,\boldsymbol{k}(t')}dt'} e^{-i\boldsymbol{A}(t)\cdot\boldsymbol{r}} \phi_{b,\boldsymbol{k}_0+\boldsymbol{A}(t)}(\boldsymbol{r}). \tag{2.70}$$

[2] It is interesting to see the analogy between the accelerated Bloch states and the Volkov states [25], or the adiabatic electron states in vacuum under an electric field, which are often used to discuss the field-driven acceleration of ionized electrons from atoms and molecules [17].

The electron stays in the initial band b while keeping its crystal momentum $\boldsymbol{k}_0$, but its other properties are changed to those of $\phi_{b,\boldsymbol{k}_0+\boldsymbol{A}(t)}$. In other words, the electron looks like it is being accelerated within the same band according to the EoM,

$$\frac{d}{dt}\boldsymbol{k} = -\boldsymbol{\mathcal{E}}(t), \tag{2.71}$$

which corresponds to what is called the adiabatic *acceleration theorem* [71, 76].

Interband excitation

When the electron reaches the vicinity of the minimum band gap (MBG), $\boldsymbol{\xi}_{\lambda\lambda'}(\boldsymbol{k})$ can be large, because $\Delta\varepsilon_{\lambda\lambda'}(\boldsymbol{k})$ becomes small and $|\boldsymbol{p}_{\boldsymbol{k}}^{\lambda\lambda'}|$ large. Therefore, in the vicinity of MBG, interband transition can take place between adjacent bands. Let us consider interband excitation from an initial VB b to the first CB c, assuming the frozen VB approximation, where the wave function is given by

$$\psi_{b,\boldsymbol{k}_0}(\boldsymbol{r},t) \approx e^{-i\int_0^t \varepsilon_{b,\boldsymbol{k}(t')}dt'}\tilde{\phi}_{b,\boldsymbol{k}_0}(\boldsymbol{r},t) + a^c_{b,\boldsymbol{k}_0}(t)e^{-i\int_0^t \varepsilon_{c,\boldsymbol{k}(t')}dt'}\tilde{\phi}_{c,\boldsymbol{k}_0}(\boldsymbol{r},t), \tag{2.72}$$

with $a^c_{b,\boldsymbol{k}_0}(t) \ll 1$. The EoM is mainly governed by the excitation from VB b to CB c,

$$i\frac{d}{dt}a^c_{b,\boldsymbol{k}_0}(t) = \boldsymbol{\mathcal{E}}(t)\cdot\boldsymbol{\xi}_{cb}(\boldsymbol{k}(t))e^{i\int_0^t \Delta\varepsilon_{cb}(\boldsymbol{k}(t'))dt'}, \tag{2.73}$$

or,

$$a^c_{b,\boldsymbol{k}_0}(t) = \frac{1}{i}\int_0^t dt'\boldsymbol{\mathcal{E}}(t')\cdot\boldsymbol{\xi}_{cb}(\boldsymbol{k}(t'))e^{i\int_0^{t'} \Delta\varepsilon_{cb}(\boldsymbol{k}(t''))dt''}. \tag{2.74}$$

In a similar manner to the Lewenstein model for the gas-phase HHG [23], Eq. (2.74) can be evaluated using the saddle-point method. A similar discussion has been made by Vampa *et al.* using a two-band model [45]. If we define the classical action $S^{\lambda\lambda'}_{\boldsymbol{k}_0}(t) = \int_0^t dt'\Delta\varepsilon_{\lambda\lambda'}(\boldsymbol{k}(t'))$, the major contribution comes from the saddle point t_s which satisfies

$$\frac{d}{dt'}S^{cb}_{\boldsymbol{k}_0}(t')|_{t'=t_s} = 0 \Leftrightarrow \Delta\varepsilon_{cb}(\boldsymbol{k}(t'))|_{t'=t_s} = 0. \tag{2.75}$$

For a direct gap system which has its MBG at the Γ point $\boldsymbol{k} = 0$, $\Delta\varepsilon_{cb}(\boldsymbol{k})$ can be approximated as a (isotropic) parabolic band,

$$\Delta\varepsilon_{cb}(\boldsymbol{k}) = \varepsilon_g + \frac{k^2}{2m_r}, \tag{2.76}$$

where ε_g and m_r are the band gap energy and the effective reduced mass, respectively. Note that m_r can be approximated as [78]

$$\frac{1}{m_r} = \frac{4|\boldsymbol{p}^{cb}_{\boldsymbol{k}=0}|^2}{\varepsilon_g}. \tag{2.77}$$

Equation (2.75) cannot be satisfied for a real t_s and we have to introduce a complex time. The imaginary part of t_s is usually interpreted as the tunneling time. In the classical approximation, where $\varepsilon_g = 0$, we have a real value solution,

$$\boldsymbol{k}(t_d) = 0 \Leftrightarrow \boldsymbol{k}_0 + A(t_d) = 0, \tag{2.78}$$

which determines the timing of the tunneling at the MBG. By expanding the complex time t_s around the real time t_d, we obtain (see Appendix B for detail),

$$a^c_{b,\boldsymbol{k}_0}(t) = 2\pi e^{iS^{cb}_{\boldsymbol{k}_0}(t_d)}e^{-\frac{\sqrt{2\varepsilon_g}}{3|\boldsymbol{\mathcal{E}}(t_d)\cdot\boldsymbol{\xi}^{cb}_0|}}\boldsymbol{\mathcal{E}}(t_d)\cdot\boldsymbol{p}^{cb}_{k(t_d)}. \tag{2.79}$$

We can see that the tunneling process in solids has a similar exponential factor to that in gas-phase tunneling given by Eq. (1.4), which becomes large for intense fields.

2.4.2 Field-induced current

Another advantage of using the Houston basis is that it allows us to have a physically intuitive interpretation of the current density $\boldsymbol{j}(t)$. Inserting the expansion of the electron orbital with the Houston states (2.64), into the formula of current density Eq. (2.51) yields

$$\boldsymbol{j}_{b,\boldsymbol{k}_0}(t) = \sum_{\mu\nu} a^{\mu*}_{b,\boldsymbol{k}_0}(t) a^{\nu}_{b,\boldsymbol{k}_0}(t) e^{i\int_0^t \Delta\varepsilon_{\mu\nu}(\boldsymbol{k}(t'))dt'} \boldsymbol{p}^{\mu\nu}_{\boldsymbol{k}(t)}. \tag{2.80}$$

The *intraband* current, or the diagonal components in Eq. (2.80) is given by

$$\boldsymbol{j}^{\text{intra}}_{b,\boldsymbol{k}_0}(t) = \sum_{\mu} |a^{\mu}_{b,\boldsymbol{k}_0}(t)|^2 \boldsymbol{p}^{\mu\mu}_{\boldsymbol{k}(t)} = \sum_{\mu} |a^{\mu}_{b,\boldsymbol{k}_0}(t)|^2 v_{\mu}(\boldsymbol{k}(t)), \tag{2.81}$$

where

$$v_{\lambda}(\boldsymbol{k}(t)) = \left.\frac{\partial\varepsilon_{\lambda,\boldsymbol{k}}}{\partial\boldsymbol{k}}\right|_{\boldsymbol{k}=\boldsymbol{k}(t)} = p^{\lambda\lambda}_{\boldsymbol{k}(t)} \tag{2.82}$$

is the group velocity in band λ. The intraband current (2.81) represents the ballistic motion of charge carriers.

The *interband current* is the off-diagonal components of Eq. (2.80),

$$\boldsymbol{j}^{\text{inter}}_{b,\boldsymbol{k}_0}(t) = \sum_{\mu\neq\nu} a^{\mu*}_{b,\boldsymbol{k}_0}(t) a^{\nu}_{b,\boldsymbol{k}_0}(t) e^{i\int_0^t \Delta\varepsilon_{\mu\nu}(\boldsymbol{k}(t'))dt'} \boldsymbol{p}^{\mu\nu}_{\boldsymbol{k}(t)}. \tag{2.83}$$

The interband current corresponds to the radiation from interband coherence between bands, or photon emission upon interband transition.

3
Numerical Methods

In this chapter, the numerical methods are summarized. In general, we numerically solve the equation of motion Eq. (2.35) for the periodic part of time-dependent electron orbitals $\psi_{b,\boldsymbol{k}}(\boldsymbol{r},t)$,

$$i\frac{\partial}{\partial t}u_{\lambda,\boldsymbol{k}}(\boldsymbol{r},t)=\int_{\Omega}d\boldsymbol{r}'h_{\boldsymbol{k}}(\boldsymbol{r},\boldsymbol{r}',t)u_{\lambda,\boldsymbol{k}}(\boldsymbol{r}',t),$$

on a real-space basis, with

$$h_{\boldsymbol{k}}(\boldsymbol{r},\boldsymbol{r}',t)=\left[\frac{1}{2}\left(\frac{\nabla}{i}+\boldsymbol{k}+\boldsymbol{A}(t)\right)^2+v_{\mathrm{l}}(\boldsymbol{r})\right]\delta(\boldsymbol{r}-\boldsymbol{r}')+v^{\Omega}_{\mathrm{nl},\boldsymbol{k}+\boldsymbol{A}(t)}(\boldsymbol{r},\boldsymbol{r}')+v^{\Omega}_{\mathrm{x},\boldsymbol{k}}[\rho(t)](\boldsymbol{r},\boldsymbol{r}').$$

Instead of expanding the wave functions with a basis function [27, 33, 34, 42, 43, 45, 46, 49, 52, 53, 55], we solve these equation of motion Eq. (2.35) directly on a spatial grid; it has previously been reported that the real-space basis calculations have better convergence than that done with the Bloch basis [79]. Moreover, it naturally supports interband transitions among all the bands realized by the Hamiltonian. The importance of including multiple bands has been pointed out by several authors [43, 53]

3.1 Overview

The main algorithm for the numerical implementation of the EoM (2.35) is shown in Algorithm 1. After loading an input file (line 2), which contains parameters that determine the physical system details, incident electric filed, and time propagation, the spatially and temporally discretized Hamiltonian and wave function are generated (line 3-4). In numerical simulations, we have to (1) prepare the initial (ground) state, (2) calculate the real-time propagation of the wave function, and (3) obtain physically relevant observable quantities from the wave function. The initial state preparation is achieved in line 6, in which the ground state wave function is calculated using the imaginary-time propagation method. The real-time propagation is calculated in line 7, starting from the prepared initial state. Parallel to this, time-dependent physically relevant quantities are computed and outputted.

Algorithm 1 The main algorithm in our simulation

```
1: procedure MAIN
2:     input()                          ▷ input parameters from file
3:     make_grid()                      ▷ generate discretized coordinates
4:     make_wfun()                      ▷ generate discretized orbital
5:
6:     init()                           ▷ imaginary-time propagation
7:     tdse()                           ▷ real-time propagation
```

Here, I will give a general formalism for multidimensional system to be useful as a future reference. Although we use 1D systems in our works presented in the following chapters, the discussion introduced here can be easily reduced to a 1D system.

3.2 Periodic boundary condition and momentum-space sampling

We assume that we have N_i unit cells in the $\boldsymbol{a}_i$ direction, which forms a large periodic system, or what we call a super cell. Here $\boldsymbol{a}_i$, $i = 1, \ldots, d$ are the primitive lattice vectors and d denotes the system dimension. The volume Ω of the unit cell is given by

$$\Omega = |\det(\boldsymbol{a})|. \tag{3.1}$$

N_i is a finite but large integer. The total number of unit cells N_{cell} in the supercell is given by $N_{\text{cell}} = \prod_{i=1}^{d} N_i$.

We employ the periodic boundary conditions for the supercell, or the Born-von Kàrmàn boundary conditions, so that the wave function at an edge of the supercell is equal to that at the opposite edge, namely,

$$\psi_{\lambda,\boldsymbol{k}}(\boldsymbol{r} + N_i\boldsymbol{a}_i, t) = \psi_{\lambda,\boldsymbol{k}}(\boldsymbol{r}, t), \quad i = 1, \ldots, d. \tag{3.2}$$

From Eq. (2.32) and the periodic boundary condition (3.2),

$$\psi_{\lambda,\boldsymbol{k}}(\boldsymbol{r} + N_i\boldsymbol{a}_i, t) = e^{i\boldsymbol{k}\cdot N_i\boldsymbol{a}_i}\psi_{\lambda,\boldsymbol{k}}(\boldsymbol{r}, t) = \psi_{\lambda,\boldsymbol{k}}(\boldsymbol{r}, t), \tag{3.3}$$

or,

$$e^{i\boldsymbol{k}\cdot N_i\boldsymbol{a}_i} = 1. \tag{3.4}$$

As a consequence, $\boldsymbol{k}$ must follow the following condition,

$$\boldsymbol{k} = \frac{n_1}{N_1}\boldsymbol{b}_1 + \frac{n_2}{N_2}\boldsymbol{b}_2 + \cdots = \sum_{i=1}^{d}\frac{n_i}{N_i}\boldsymbol{b}_i, \tag{3.5}$$

where $\boldsymbol{b}_i$ is the usual reciprocal lattice vector satisfying $\boldsymbol{b}_i \cdot \boldsymbol{a}_i = 2\pi\delta_{ij}$ and n_i is an arbitrary integer $\in [0, N_i - 1]$. Hereafter, we will denote the first Brillouin zone (BZ) simply as BZ. The number of k-point N_k within a BZ is given by $N_k = \prod_{i=1}^{d} N_i = N_{\text{cell}}$. Note that the total number of k-point within a BZ is equal to the total number of unit cells in the supercell.

3.2.1 Momentum-space sampling

In the implementation, it is better to employ a symmetric k-point sampling in terms of simulation convergence. In order to achieve this requirement, we take $N_i = 2m_i + 1$ in an odd number with m_i being an integer, and sample a k-point with

$$\boldsymbol{k} = \sum_{i=1}^{3}\frac{n_i}{N_i}\boldsymbol{b}_i = \sum_{i=1}^{3}\frac{n_i}{2m_i + 1}\boldsymbol{b}_i, \tag{3.6}$$

and

$$n_i = -m_i, -m_i + 1, \ldots, 0, \ldots, m_i \quad (i = 1, \ldots, d), \tag{3.7}$$

which results in a symmetric sampling around the origin, as shown in Fig. 3.1.

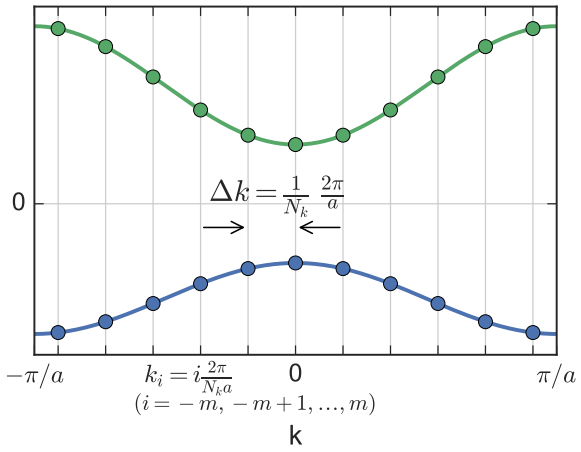

Figure 3.1: Schematic diagram for the k-space sampling for a one-dimensional system.

3.3 Discretization of real-space coordinates

We discretize the spatial coordinate as

$$\boldsymbol{r}_{\boldsymbol{l}} = \frac{l_1}{N_1^\Omega}\boldsymbol{a}_1 + \frac{l_2}{N_2^\Omega}\boldsymbol{a}_2 + \cdots = \sum_i^d \frac{l_i}{N_i^\Omega}\boldsymbol{a}_i, \tag{3.8}$$

where N_i^Ω denotes the total number of grid points in a unit cell along $\boldsymbol{a}_i$ direction and

$$l_i = 0, 1, \ldots, N_i^\Omega N_i - 1. \tag{3.9}$$

The total number of grid points N_Ω in a unit cell is given by $N_\Omega = \prod_i^d N_i^\Omega$. Then, a function of $\boldsymbol{r}$ is discretized as

$$f(\boldsymbol{r}) \to f_{\boldsymbol{l}} = f(\boldsymbol{r}_{\boldsymbol{l}}), \tag{3.10}$$

as shown in Fig. 3.2(b), and the spatial integral is transformed as

$$\int d\boldsymbol{r} f(\boldsymbol{r}) \to \sum_{\boldsymbol{l}} f_{\boldsymbol{l}} \frac{\Omega}{N_\Omega}. \tag{3.11}$$

The differential is calculated by using the Fourier expansion of the periodic function $f(\boldsymbol{r})$,

$$\begin{aligned} \nabla f(\boldsymbol{r}) = \nabla \sum_{\boldsymbol{G}} f_{\boldsymbol{G}} e^{i\boldsymbol{G}\cdot\boldsymbol{r}} = \sum_{\boldsymbol{G}} f_{\boldsymbol{G}} (i\boldsymbol{G}) e^{i\boldsymbol{G}\cdot\boldsymbol{r}}, \quad f_{\boldsymbol{G}} = \frac{1}{\Omega}\int_\Omega d\boldsymbol{r} f(\boldsymbol{r}) e^{-i\boldsymbol{G}\cdot r} \\ \to \nabla f_{\boldsymbol{l}} = \sum_{\boldsymbol{G}} f_{\boldsymbol{G}} i\boldsymbol{G} e^{i\boldsymbol{G}\cdot\boldsymbol{r}_{\boldsymbol{l}}}, \quad f_{\boldsymbol{G}} = \frac{1}{N_\Omega}\sum_{\boldsymbol{l}} f_{\boldsymbol{l}} e^{-i\boldsymbol{G}\cdot\boldsymbol{r}_{\boldsymbol{l}}}. \end{aligned} \tag{3.12}$$

$\boldsymbol{G}$ is a reciprocal lattice vector whose total number $N_{\boldsymbol{G}}$ is equal to N_Ω. By taking N_i^Ω as an odd number, we employ a symmetric sampling of $\boldsymbol{G}$.

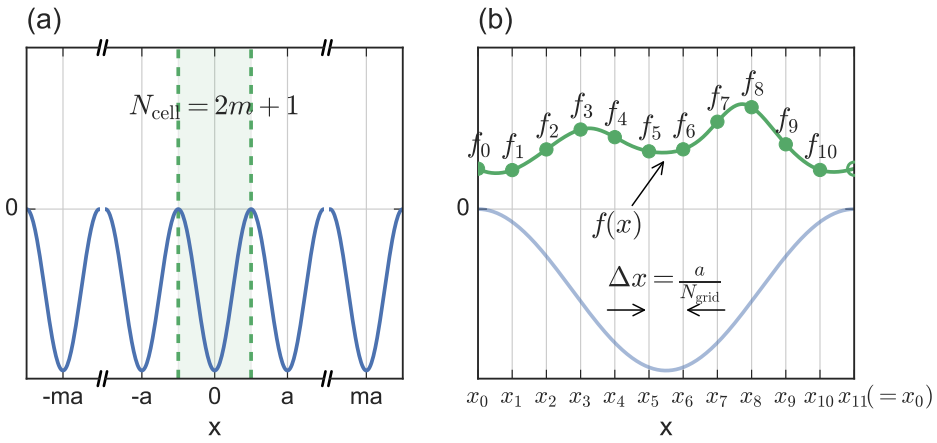

Figure 3.2: Schematic diagram for the real-space discretization for a one-dimensional system.

3.3.1 Hamiltonian operation in the discretized coordinate-space

Following the discretizing recipe above, we discretize the periodic part of the electron orbital as

$$u_{\lambda,\boldsymbol{k}}(\boldsymbol{r},t) \to u_{\lambda,\boldsymbol{k},\boldsymbol{l}}(t) = u_{\lambda,\boldsymbol{k}}(\boldsymbol{r}_{\boldsymbol{l}},t), \tag{3.13}$$

and its EoM as

$$\begin{aligned} i\frac{\partial}{\partial t}u_{\lambda,\boldsymbol{k}}(\boldsymbol{r},t) &= \int_{\Omega} d\boldsymbol{r} h_{\boldsymbol{k}}(\boldsymbol{r},\boldsymbol{r}',t)u_{\lambda,\boldsymbol{k}}(\boldsymbol{r}',t) \\ \to i\frac{\partial}{\partial t}u_{\lambda,\boldsymbol{k},\boldsymbol{l}}(t) &= \sum_{l'_1=0}^{N_1^{\Omega}-1}\cdots\sum_{l'_d=0}^{N_d^{\Omega}-1}\frac{\Omega}{N_{\Omega}}h_{\boldsymbol{k},\boldsymbol{l},\boldsymbol{l}'}(t)u_{\lambda,\boldsymbol{k},\boldsymbol{l}'}(t), \end{aligned} \tag{3.14}$$

where the discretized Hamiltonian $h_{\boldsymbol{k},\boldsymbol{l},\boldsymbol{l}'}(t)$ is given by

$$h_{\boldsymbol{k},\boldsymbol{l},\boldsymbol{l}'}(t) = h_{\boldsymbol{k}}(\boldsymbol{r}_{\boldsymbol{l}},\boldsymbol{r}_{\boldsymbol{l}'},t). \tag{3.15}$$

The Hamiltonian operation can be decomposed into the following terms:

1. kinetic term $(\nabla/i + \boldsymbol{k} + \boldsymbol{A}(t))^2 u_{\lambda,\boldsymbol{k}}(\boldsymbol{r})/2$
2. local potential term $v_{\mathrm{l}}(\boldsymbol{r})u_{\lambda,\boldsymbol{k}}(\boldsymbol{r})$
3. nonlocal potential term $\int_{\Omega} d\boldsymbol{r}' v^{\Omega}_{\mathrm{nl},\boldsymbol{k}+\boldsymbol{A}(t)}(\boldsymbol{r},\boldsymbol{r}')u_{\lambda,\boldsymbol{k}}(\boldsymbol{r}')$.
4. exchange term $\int_{\Omega} d\boldsymbol{r}' v^{\Omega}_{\mathrm{x},\boldsymbol{k}}(\boldsymbol{r},\boldsymbol{r}')u_{\lambda,\boldsymbol{k}}(\boldsymbol{r}')$.

We compute each of these terms in the following manner:

The operation of kinetic term

As the kinetic term includes the differentiation operator, we conduct this operation using the Fourier expansion and the formula (3.12),

$$\left[\frac{1}{2}\left(\frac{\nabla}{i}+\boldsymbol{k}+\boldsymbol{A}(t)\right)^2 u_{\lambda,\boldsymbol{k}}(\boldsymbol{r})\right]_{\boldsymbol{l}} = \sum_{\boldsymbol{G}}\frac{1}{2}\left(\boldsymbol{G}+\boldsymbol{k}+\boldsymbol{A}(t)\right)^2 u_{\lambda,\boldsymbol{k},\boldsymbol{G}}e^{i\boldsymbol{G}\cdot\boldsymbol{r}_{\boldsymbol{l}}}, \tag{3.16}$$

where $u_{\lambda,\boldsymbol{k},\boldsymbol{G}}$ is the Fourier transform of $u_{\lambda,\boldsymbol{k},\boldsymbol{l}}$,

$$u_{\lambda,\boldsymbol{k},\boldsymbol{G}} = \frac{1}{N_\Omega}\sum_{\boldsymbol{l}} u_{\lambda,\boldsymbol{k},\boldsymbol{l}} e^{-i\boldsymbol{G}\cdot\boldsymbol{r}_{\boldsymbol{l}}}. \tag{3.17}$$

In the implementation, both of the inverse and forward Fourier transform are computed by fast Fourier transform (FFT) using the FFTW[1] library [80].

The operation of local potential term

The operation of a local potential can be easily obtained as a product of the discretized potential and wave function,

$$[v_{\mathrm{l}}(\boldsymbol{r})u_{\lambda,\boldsymbol{k}}(\boldsymbol{r})]_{\boldsymbol{l}} = v_{\mathrm{l}}(\boldsymbol{r}_{\boldsymbol{l}})u_{\lambda,\boldsymbol{k},\boldsymbol{l}}. \tag{3.18}$$

As for the Hartree potential $v_{\mathrm{H}}[\rho(t)](\boldsymbol{r})$ in the TDHF equations, we need to update the density matrix at each step as

$$v_{\mathrm{H}}[\rho(t)](\boldsymbol{r}_{\boldsymbol{l}}) = 2\sum_{b',\boldsymbol{k}'_0,\boldsymbol{l}'} \frac{\Omega}{N_\Omega}|u_{b',\boldsymbol{k}'_0,\boldsymbol{l}'}(t)|^2 v_0^\Omega(\boldsymbol{r}_{\boldsymbol{l}} - \boldsymbol{r}_{\boldsymbol{l}'}), \tag{3.19}$$

where

$$v_0^\Omega(\boldsymbol{r}_{\boldsymbol{l}}) = \frac{1}{N_k}\sum_{\boldsymbol{T}} v(\boldsymbol{r}_{\boldsymbol{l}} + \boldsymbol{T}) \tag{3.20}$$

is prepared in advance.

The operation of nonlocal potential term

For the operation of a nonlocal potential, we have to compute the summation over the discretized coordinates,

$$\left[\int_\Omega d\boldsymbol{r}' v^\Omega_{\mathrm{nl},\boldsymbol{k}+\boldsymbol{A}(t)}(\boldsymbol{r},\boldsymbol{r}')u_{\lambda,\boldsymbol{k}}(\boldsymbol{r}',t)\right]_{\boldsymbol{l}} = \sum_{l'_1=0}^{N_1^\Omega-1}\cdots\sum_{l'_d=0}^{N_d^\Omega-1}\frac{\Omega}{N_\Omega}v^\Omega_{\mathrm{nl},\boldsymbol{k}+\boldsymbol{A}(t)}(\boldsymbol{r}_{\boldsymbol{l}},\boldsymbol{r}_{\boldsymbol{l}'})u_{\lambda,\boldsymbol{k},\boldsymbol{l}'}(t). \tag{3.21}$$

As the nonlocal potential changes with the field vector potential, it needs to be updated at each time step following Eq. (2.37) as

$$v^\Omega_{\mathrm{nl},\boldsymbol{k}+\boldsymbol{A}(t)}(\boldsymbol{r}_{\boldsymbol{l}},\boldsymbol{r}_{\boldsymbol{l}'}) = \sum_{\boldsymbol{T}} e^{-i(\boldsymbol{k}+\boldsymbol{A}(t))\cdot\boldsymbol{r}_{\boldsymbol{l}}} v_{\mathrm{nl}}(\boldsymbol{r}_{\boldsymbol{l}},\boldsymbol{r}_{\boldsymbol{l}'}+\boldsymbol{T})e^{i(\boldsymbol{k}+\boldsymbol{A}(t))\cdot(\boldsymbol{r}_{\boldsymbol{l}'}+\boldsymbol{T})}. \tag{3.22}$$

The operation of the exchange term

The operation of the exchange potential is given by

$$\left[\int_\Omega d\boldsymbol{r}' v^\Omega_{\mathrm{x},\boldsymbol{k}}(\boldsymbol{r},\boldsymbol{r}',t)u_{\lambda,\boldsymbol{k}}(\boldsymbol{r}',t)\right]_{\boldsymbol{l}} = \sum_{l'_1=0}^{N_1^\Omega-1}\cdots\sum_{l'_d=0}^{N_d^\Omega-1}\frac{\Omega}{N_\Omega}v^\Omega_{\mathrm{x},\boldsymbol{k}}[\rho(t)](\boldsymbol{r}_{\boldsymbol{l}},\boldsymbol{r}_{\boldsymbol{l}'})u_{\lambda,\boldsymbol{k},\boldsymbol{l}'}(t). \tag{3.23}$$

[1] FFTW is an abbreviation for the *Fastest Fourier Transform in the West*. The FFTW library was developed at MIT by Matteo Frigo and Steven G. Johnson. The manual can be refereed at `http://www.fftw.org/`.

As the density matrix changes in time, the exchange potential $v_{\mathrm{x},\boldsymbol{k}}[\rho(t)](\boldsymbol{r}_{\boldsymbol{l}}, \boldsymbol{r}_{\boldsymbol{l}'})$ is updated at each time step,

$$v_{\mathrm{x},\boldsymbol{k}}[\rho(t)](\boldsymbol{r}_{\boldsymbol{l}}, \boldsymbol{r}_{\boldsymbol{l}'}) = -\sum_{b',\boldsymbol{k}'} u_{b',\boldsymbol{k}',\boldsymbol{l}}(t) u^{*}_{b',\boldsymbol{k}',\boldsymbol{l}'}(t) v^{\Omega}_{\boldsymbol{k}-\boldsymbol{k}'}(\boldsymbol{r}_{\boldsymbol{l}} - \boldsymbol{r}_{\boldsymbol{l}'}), \tag{3.24}$$

where

$$v^{\Omega}_{\boldsymbol{k}}(\boldsymbol{r}_{\boldsymbol{l}}) = \frac{1}{N_k} \sum_{\boldsymbol{T}} v(\boldsymbol{r}_{\boldsymbol{l}} + \boldsymbol{T}) e^{-i\boldsymbol{k}\cdot(\boldsymbol{r}_{\boldsymbol{l}'} + \boldsymbol{T})} \tag{3.25}$$

is prepared in advance.

3.4 Initial state preparation

The real-time simulation starts from the ground state of the field-free Hamiltonian $\hat{h}_{0,\boldsymbol{k}}$,

$$h_{0,\boldsymbol{k}}(\boldsymbol{r}, \boldsymbol{r}') = \left[\frac{1}{2}\left(\frac{\nabla}{i} + \boldsymbol{k}\right) + v_{\mathrm{l}}(\boldsymbol{r})\right] \delta(\boldsymbol{r} - \boldsymbol{r}') + v_{\mathrm{nl}}(\boldsymbol{r}, \boldsymbol{r}') + v_{\mathrm{x},\boldsymbol{k}}(\boldsymbol{r}, \boldsymbol{r}'). \tag{3.26}$$

In our study, we obtain the ground state using the imaginary-time propagation (ITP) method. In the ITP method, we consider the TDSE in *imaginary time*; namely, we make a substitution $t \to i\tau$ with τ being a real number. With this substitution, we have

$$\frac{\partial}{\partial t} u(\boldsymbol{r}, \tau) = -\hat{h}_{0,\boldsymbol{k}} u(\boldsymbol{r}, \tau). \tag{3.27}$$

Let us express the wave function at $\tau = 0$ as a superposition of the eigenstates $u^{0}_{\lambda,\boldsymbol{k}}(\boldsymbol{r})$ of the Hamiltonian $\hat{h}_{0,\boldsymbol{k}}$ with eigenenergy $\varepsilon_{\lambda,\boldsymbol{k}}$,

$$u(\boldsymbol{r}, \tau = 0) = \sum_{\mu} a_{\mu,\boldsymbol{k}} u^{0}_{\mu,\boldsymbol{k}}(\boldsymbol{r}). \tag{3.28}$$

Inserting Eq. (3.28) into Eq. (3.27) yields the (imaginary) time-evolution of the wave function,

$$u(\boldsymbol{r}, \tau) = \sum_{\mu} e^{-\varepsilon_{\mu,\boldsymbol{k}}\tau} a_{\mu,\boldsymbol{k}} u^{0}_{\mu,\boldsymbol{k}}(\boldsymbol{r}). \tag{3.29}$$

For simplicity, we assume that the eigenenergies are non-degenerate and $\varepsilon_{0,\boldsymbol{k}} < \varepsilon_{1,\boldsymbol{k}} < \cdots$. In the limit $\tau \to \infty$, we get $u(\boldsymbol{r}, \tau) \to e^{-\varepsilon_{0,\boldsymbol{k}}\tau} u^{0}_{0,\boldsymbol{k}}(\boldsymbol{r})$ because the exponential factor $e^{-\varepsilon_{\lambda,\boldsymbol{k}}\tau}$ for $\lambda > 0$ decays more quickly than for $\lambda = 0$. Note that we have to prepare the initial wave function so that $a_{0,\boldsymbol{k}} \neq 0$ at $\tau = 0$. We prepare the initial wave function as a localized state that has a gaussian shape whose central position is located at a point in a unit cell. The eigenstates with higher eigenenergies can be also obtained by propagating other wave functions simultaneously while orthonormalizing the wave functions with each other using the Gram-Schmidt orthonormalization. In the implementation, we also diagonalize the overlap matrix in order to obtain a quick convergence of the wave functions. The convergence of the ITP is checked by monitoring the residuals of $|\hat{h}_{0,\boldsymbol{k}} u(\tau) - \langle u(\tau)|\hat{h}_{0,\boldsymbol{k}}|u(\tau)\rangle\,|$, which is to go to zero in the limit of $\tau \to \infty$. The time propagation is evaluated using a fourth-order Runge-Kutta method, which will be explained in detail in the next section.

3.5 Real-time propagation

Starting from the initial ground state $u^0_{b,\boldsymbol{k}_0}(\boldsymbol{r})$ obtained by the ITP, we evaluate the time-evolution of an electron orbital $u_{b,\boldsymbol{k}_0}(\boldsymbol{r},t)$ based on the discretized EoM (3.14). We also use a fourth-order Runge-Kutta method for the time propagation as follows. We want to solve an EoM, whose form is given by

$$i\frac{\partial}{\partial t}u_{b,\boldsymbol{k}_0,\boldsymbol{l}}(t) = f(\{u_{b,\boldsymbol{k}_0,\boldsymbol{l}}(t)\},t), \tag{3.30}$$

where $f(\dot{})$ denotes the Hamiltonian operation. Let us define a temporal step size Δt and i-th time $t_i = i\Delta t_i$. According to the fourth-order Runge-Kutta method, we have

$$u_{b,\boldsymbol{k}_0,\boldsymbol{l}}(t_{i+1}) = u_{b,\boldsymbol{k}_0,\boldsymbol{l}}(t_i) + \frac{\Delta t}{6}(f_1 + 2f_2 + 2f_3 + f_4), \tag{3.31}$$

where

$$f_1 = f(\{u_{b,\boldsymbol{k}_0,\boldsymbol{l}}(t_i)\},t_i), \tag{3.32}$$

$$f_2 = f(\{u_{b,\boldsymbol{k}_0,\boldsymbol{l}}(t_i) + \frac{f_1}{2}\Delta t\},t_i + \frac{\Delta t}{2}), \tag{3.33}$$

$$f_3 = f(\{u_{b,\boldsymbol{k}_0,\boldsymbol{l}}(t_i) + \frac{f_2}{2}\Delta t\},t_i + \frac{\Delta t}{2}), \tag{3.34}$$

$$f_4 = f(\{u_{b,\boldsymbol{k}_0,\boldsymbol{l}}(t_i) + f_3\Delta t\},t_i + \Delta t). \tag{3.35}$$

In the implementation, we define N_{step} as the total number of time steps in one cycle time T_l of the electric field. Thus the time step Δt is given by T_l/N_{step}. We compute the real-time propagation for $t \in [0, N_{\text{cyc}}T_l]$, where N_{cyc} is the parameter which determines the temporal length of the simulation.

3.6 Current calculation

We calculate the HHG spectrum as the modulus square of the Fourier transform of the induced current $\boldsymbol{j}(t)$, defined by Eq. (2.48). Figure 3.3 shows a representative data of the electric field and induced current as a function of time t from our 1D simulation. After obtaining the real-time data of $\boldsymbol{j}(t)$, we calculate the harmonic spectra by taking a temporal Fourier transform. Before applying the Fourier transform, we multiply $\boldsymbol{j}(t)$ by a mask function $W(t)$ which has the same form of the field envelop function in order to suppress the remaining current after the pulse, and to analyze the coherent current that is generated during the electric field applied [43] (Fig. 3.4).

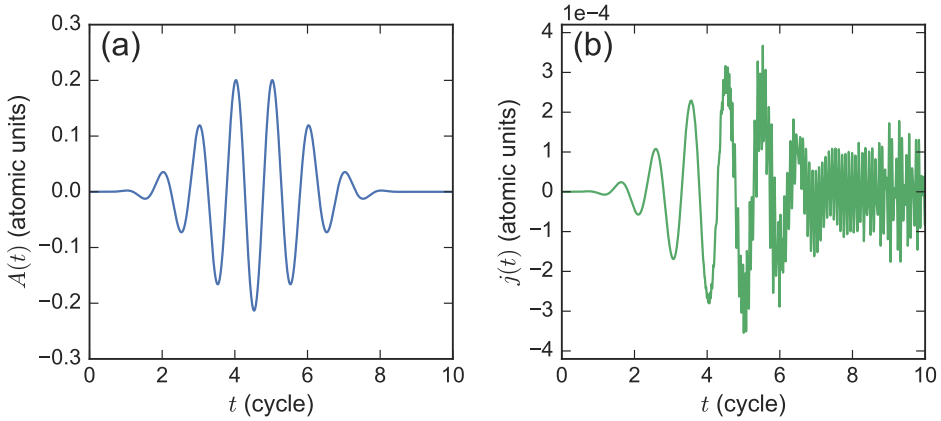

Figure 3.3: (a) A representative waveform of the vector potential used in our 1D simulations. (b) A representative waveform of real-time current $j(t)$ obtained in our 1D simulations.

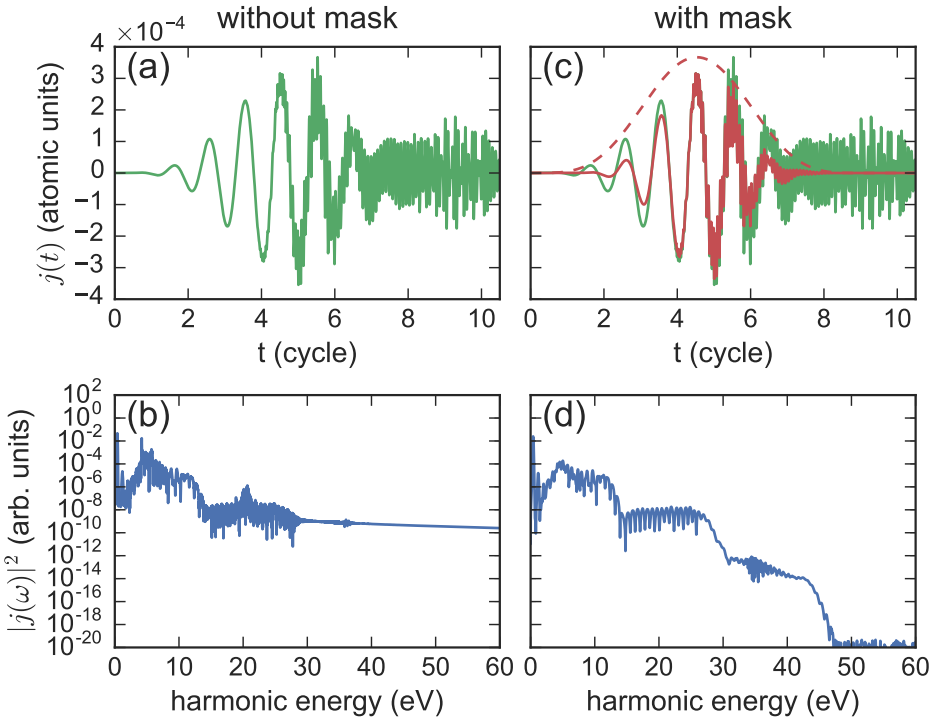

Figure 3.4: The real-time data of $j(t)$ (a, c) and corresponding harmonic spectra calculated by taking Fourier transform (b) without and (d) with multiplying the mask function $W(t)$ beforehand. The red dashed line and red waveform in (c) show the mask function $W(t)$ and waveform of $W(t)j(t)$, the current multiplied by the mask function.

4

Independent Electron Study on HHG in Solids

As the study on high-harmonic generation in solid-state materials is in its infancy, the underlying mechanism is still under intensive discussions. Historically, high-harmonic generation from solid-state materials was first discussed in terms of Bloch oscillation, or the pure intraband current [13, 27, 32, 41]. From another point of view considering the interband contribution, Vampa *et al.* [45] have proposed a real-space three-step model analogous to its counterpart for gas-phase high-harmonic generation.

With regard to simulation methods, although the pioneering works have often considered a two-band model with a single valence band and the first conduction band [42, 45, 46], the importance of the effects of multiple bands has been recently pointed out by several authors [29, 43, 49, 50, 53]. Wu *et al.* [43] have shown that the contributions from multiple bands can lead to the formation of additional plateaus, extending high-harmonic generation to higher photon energies.

Here, we show that many aspects of the solid-state high-harmonic generation can be deduced by considering electron trajectories in the momentum space across multiple bands. We study high-harmonic generation from a one-dimensional model crystal by numerically solving the time-dependent Schrödinger equation within the independent-electron approximation (Sec. 2.1.1). Discretizing the electron orbital directly on a spatial grid, we naturally include the contribution from all the bands supported by the grid. Based on the simulation results, we propose and discuss a simple model which incorporates intraband displacement, interband tunneling, and recombination with the valence band hole.

This chapter is largely reprinted from the author's published work [67]. Reprinted excerpt with permission from Takuya Ikemachi, Yasushi Shinohara, Takeshi Sato, Junji Yumoto, Makoto Kuwata-Gonokami, Kenichi L. Ishikawa, Physical Review A **95**, 043416 (2017).

4.1 Model

We consider many-electron dynamics in a 1D model crystal along laser polarization with initially VBs fully occupied across the whole BZ, typical of wide-band-gap semiconductors. Within IEA, we solve the effective TDSE for each electron in the velocity gauge, given by Eq. (2.11), but in one dimension,

$$\begin{aligned} i\frac{\partial}{\partial t}\psi_{b,k_0}(x,t) &= \hat{h}(t)\psi_{b,k_0}(x,t) \\ &= \left\{\frac{1}{2}\left[\frac{\nabla}{i}+A(t)\right]^2 + v_{\text{eff}}(x)\right\}\psi_{b,k_0}(x,t), \end{aligned} \tag{4.1}$$

for the electron that initially lies in band b with a crystal momentum k_0. Here, $A(t)$ is the vector potential, related to the laser electric field $\mathcal{E}(t)$ by $A(t) = -\int_{-\infty}^{t}\mathcal{E}(t')dt'$, and $v_{\text{eff}}(x)$ the periodic single-electron effective potential of the crystal with lattice constant a, i.e., $v_{\text{eff}}(x+a) = v_{\text{eff}}(x)$. $\psi_{b,k_0}(x,t)$ is the time-

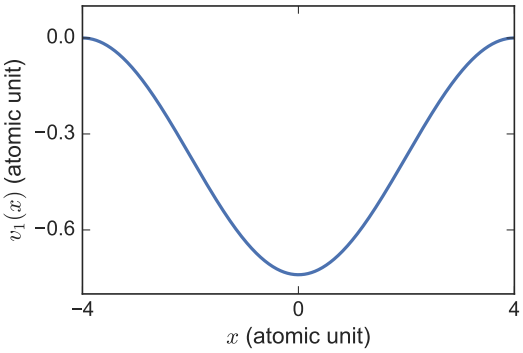

Figure 4.1: The single-electron effective potential within a unit cell.

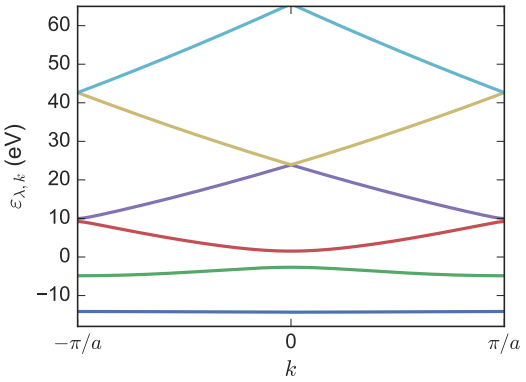

Figure 4.2: Band energy structure $\varepsilon_{\lambda,k}$ as a function of k within the first BZ.

dependent wave function whose initial state is the Bloch function ϕ_{b,k_0}, the eigenstate of the field-free Hamiltonian $\hat{h}_0 = -\nabla^2/2 + v_{\text{eff}}(x)$:

$$\hat{h}_0 \phi_{b,k_0} = \varepsilon_{b,k_0} \phi_{b,k_0}, \tag{4.2}$$

with $\varepsilon_{\lambda,k}$ being the energy eigenvalues.

Following Ref. [43], we use the Mathieu-type potential given by

$$v_{\text{eff}}(x) = -v_0 \left[1 + \cos(2\pi x/a)\right], \tag{4.3}$$

with $v_0 = 0.37$ and $a = 8$ (Fig. 4.1). I show a portion of the band structure $\varepsilon_{\lambda,k}$ in Fig. 4.2, two VBs ($\lambda = 0, 1$) and four CBs ($\lambda = 2, \ldots, 5$) from the bottom. The minimum band gap 4.2 eV between the highest VB and the lowest CB is located at $k = 0$, while the first and second CBs approach each other at the Bragg plane ($k = \pm\pi/a$). Note that, although only six bands are shown in Fig. 4.2, the bands taken into account in our calculation are not limited to these, due to our choice of the real-space basis.

Applying Bloch's theorem discussed in Ch. 2, we decompose the time-dependent orbital as $\psi_{b,k_0}(x,t) = \frac{1}{\sqrt{N_k}} e^{ik_0 x} u_{b,k_0}(x,t)$ and solve the EoM given by Eq. (2.41),

$$i\frac{\partial}{\partial t} u_{b,k_0}(x,t) = \left\{ \frac{1}{2}\left[\frac{\nabla}{i} + k_0 + A(t)\right]^2 + v_{\text{eff}}(x) \right\} u_{b,k_0}(x,t), \tag{4.4}$$

where $u_{b,k_0}(x,t)$ satisfies $u_{b,k_0}(x+a,t) = u_{b,k_0}(x,t)$. This is to be solved only within the unit cell $x \in [0,a]$, which enables substantial reduction of the problem size. We assume that the two VBs ($\lambda = 0, 1$ in Fig. 4.2) are initially filled across the whole BZ. For a given pair of (b, k_0), the initial Bloch functions are obtained using ITP. Then we numerically integrate the equation of motion (4.4), using the forth-order Runge-Kutta method with the grid spacing 0.53 atomic unit, time step size 2.67×10^{-4} fs $= 1.10 \times 10^{-2}$ atomic unit, and the number of k-points $N_k = 141$. The convergence properties are discussed in the next section.

We consider a laser pulse with electric field $\mathcal{E}(t) = \mathcal{E}_0 \sin^4(t/\tau)\sin[\omega(t - \pi\tau/2)]$ for $t \in [0, \pi\tau]$ and $\mathcal{E}(t) = 0$ for $t \notin [0, \pi\tau]$, where $\mathcal{E}_0, \tau, \omega$ denote the peak electric field amplitude, a measure of pulse width, and central angular frequency, respectively (Fig. 4.3). The central angular frequency is given by $\omega = 2\pi c/\lambda$, where c and λ denote the light velocity and the central wavelength, respectively, and the central wavelength is assumed to be $\lambda = 3200$ nm. Finally, we calculate the current using Eq. (2.51-2.53).

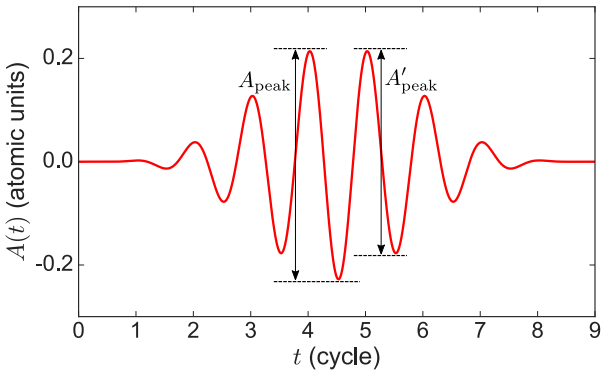

Figure 4.3: The waveform of the vector potential $A(t)$ of the laser pulse with $\mathcal{E}_0 = 1.65$ V/nm and $\tau = 96.66$ fs. The maximum and the second maximum peak-to-valley amplitude A_{peak} and $A_{peak}{}'$ are defined as depicted in the figure.

4.1.1 Convergence properties

In order to check the convergence of the real-time calculation, we have compared the simulation results for $\tau = 96.66$ fs with relevant parameters. Here, as we are interested in general aspects of harmonic spectra such as multiple-plateau structures and cutoff energy positions, we don't need a convergence in detail but in qualitative structures of harmonic spectra for several typical field strength. Figure 4.4 shows comparison of the harmonic spectra for several numbers of the spatial grid $N_{\rm grid}$, with one that is sufficiently converged ($N_{\rm grid} = 19$). We have sufficient convergence with $N_{\rm grid} = 15$, which corresponds to the grid spacing $\Delta x = a/N_{\rm grid} = 0.53$.

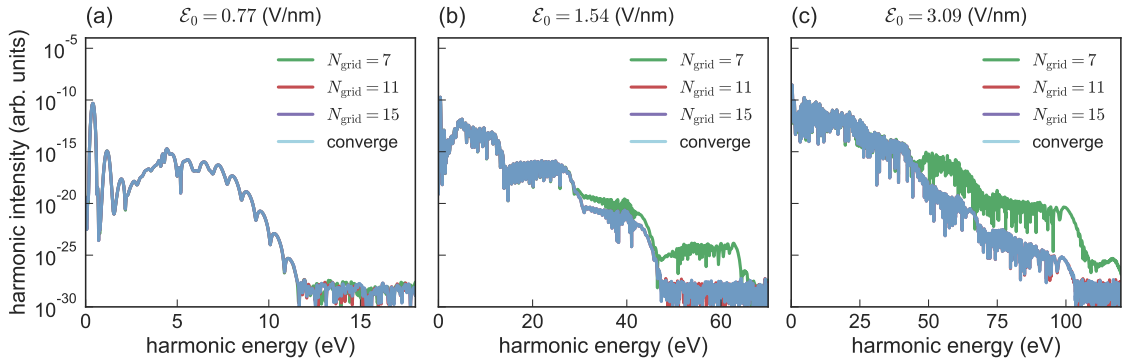

Figure 4.4: Harmonic spectra for (a) $\mathcal{E}_0 = 0.77$ V/nm, (b) $\mathcal{E}_0 = 1.54$ V/nm and (c) $\mathcal{E}_0 = 3.09$ V/nm with number of real-space grid $N_{\rm grid} = 7, 11, 15$ and $N_{\rm grid} = 19$ (labeled as convergence). In these simulations, we use $N_k = 161$ and $N_{\rm step} = 4 \times 10^4$.

We have also checked the convergence with respect to the number of temporal steps in a cycle (Fig. 4.5). From these results, we have sufficient convergence with $N_{\rm step} = 4 \times 10^4$, or a temporal step size of $\Delta t = 1.1 \times 10^{-2}$.

Figure 4.6 shows the convergence of harmonic spectra with respect to the number of k-points N_k. Although each of the spectra for various field strengths $\mathcal{E}_0$ converges qualitatively with N_k as few as 81, we have used $N_k = 141$ to make sure of sufficient convergence.

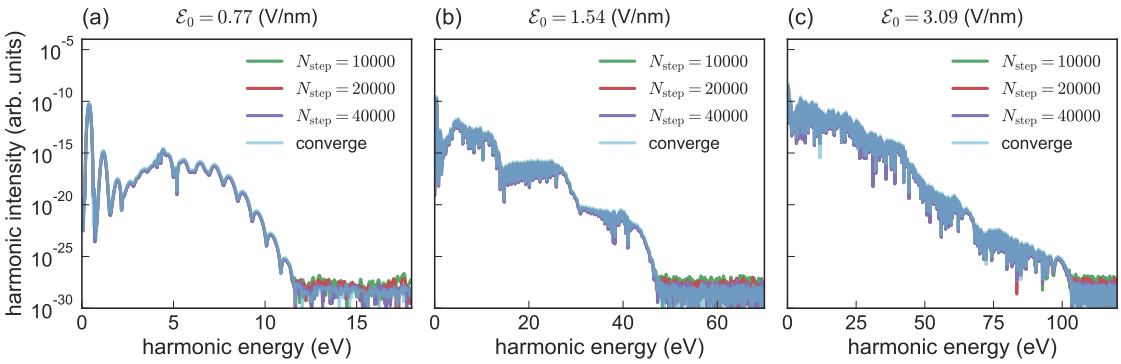

Figure 4.5: Harmonic spectra for (a) $\mathcal{E}_0 = 0.77$ V/nm, (b) $\mathcal{E}_0 = 1.54$ V/nm and (c) $\mathcal{E}_0 = 3.09$ V/nm with number of time steps in a cycle $N_{\rm step} = 1 \times 10^4, 2 \times 10^4, 4 \times 10^4$ and $N_{\rm step} = 1 \times 10^5$ (labeled as convergence). In these simulations, we use $N_k = 161$ and $N_{\rm grid} = 15$.

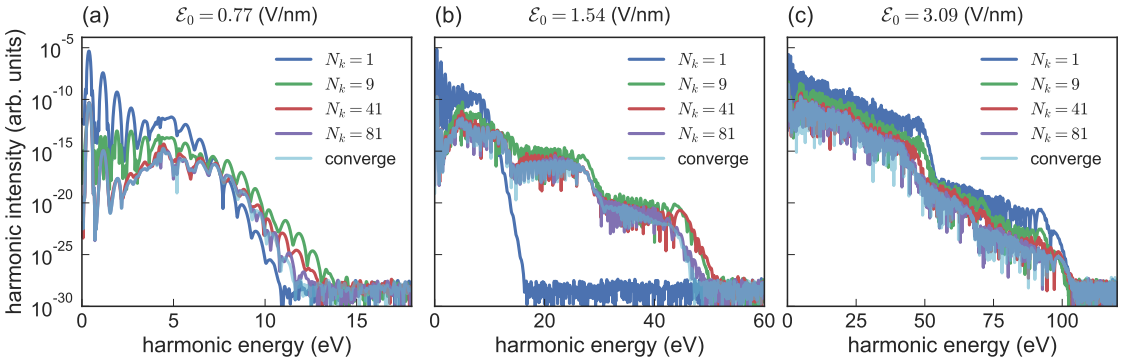

Figure 4.6: Harmonic spectra for (a) $\mathcal{E}_0 = 0.77$ V/nm, (b) $\mathcal{E}_0 = 1.54$ V/nm and (c) $\mathcal{E}_0 = 3.09$ V/nm with $N_k = 0, 9, 41, 81$ and $N_k = 201$ (labeled as convergence). In these simulations, we use $N_{\rm grid} = 15$ and $N_{\rm step} = 4 \times 10^4$.

4.2 Simulation results and discussions

The high harmonic spectra for $\tau = 96.66$ fs, which corresponds to three cycles, are shown for several field amplitudes in Fig. 4.7 (a). While the spectrum for $\mathcal{E}_0 = 0.87$ V/nm has a single plateau and cutoff similarly to atomic HHG, those for $\mathcal{E}_0 = 1.65$ and 2.11 V/nm have two additional plateaus of lower intensity, for example, for $\mathcal{E}_0 = 1.65$ V/nm, the second plateau lies at $\approx$ 15-30 eV and the third $\approx$ 30-50 eV. In Fig. 4.7(b), we show the harmonic spectra as functions of $\mathcal{E}_0$ (bottom axis). The transition from the single- to multiple-plateau structure takes place not gradually but suddenly at $\mathcal{E}_0 \approx 1.4$ V/nm. Thus, our simulations reproduce the unique features of solid-state HHG previously reported both theoretically and experimentally [29, 43, 49].

Let us now take a closer look at Fig. 4.7(b). While the cutoff energy increases smoothly with $\mathcal{E}_0$ up to 1.4 V/nm, second and third plateaus suddenly appear, and the cutoff jumps up from 15 eV to 45 eV at $\mathcal{E}_0 \approx 1.4$ V/nm. Moreover, another cutoff jump is seen at $\mathcal{E}_0 \approx 2.8$ V/nm, from 60 eV. If we let A_{peak} denote the maximum peak-to-valley amplitude of $A(t)$ (see Fig. 4.3) and show it on the top axis of Fig. 4.7(b), we notice that, the jump-up positions well coincide with the condition that $A_{peak} = \frac{\pi}{a} = 0.393$ a.u. and $\frac{2\pi}{a} = 0.786$ a.u. [vertical white dashed lines in Fig. 4.7(b)]. Note that $\frac{\pi}{a}$ is the distance from the Γ point to the first-BZ edge (Fig. 4.2). Although A_{peak} may be approximated by $2A_0$, with A_0 being the amplitude of the vector potential, in many practical situations, we use A_{peak} in the present study, since it directly characterizes the largest crystal momentum gain in the intraband dynamics, as we will see in the next

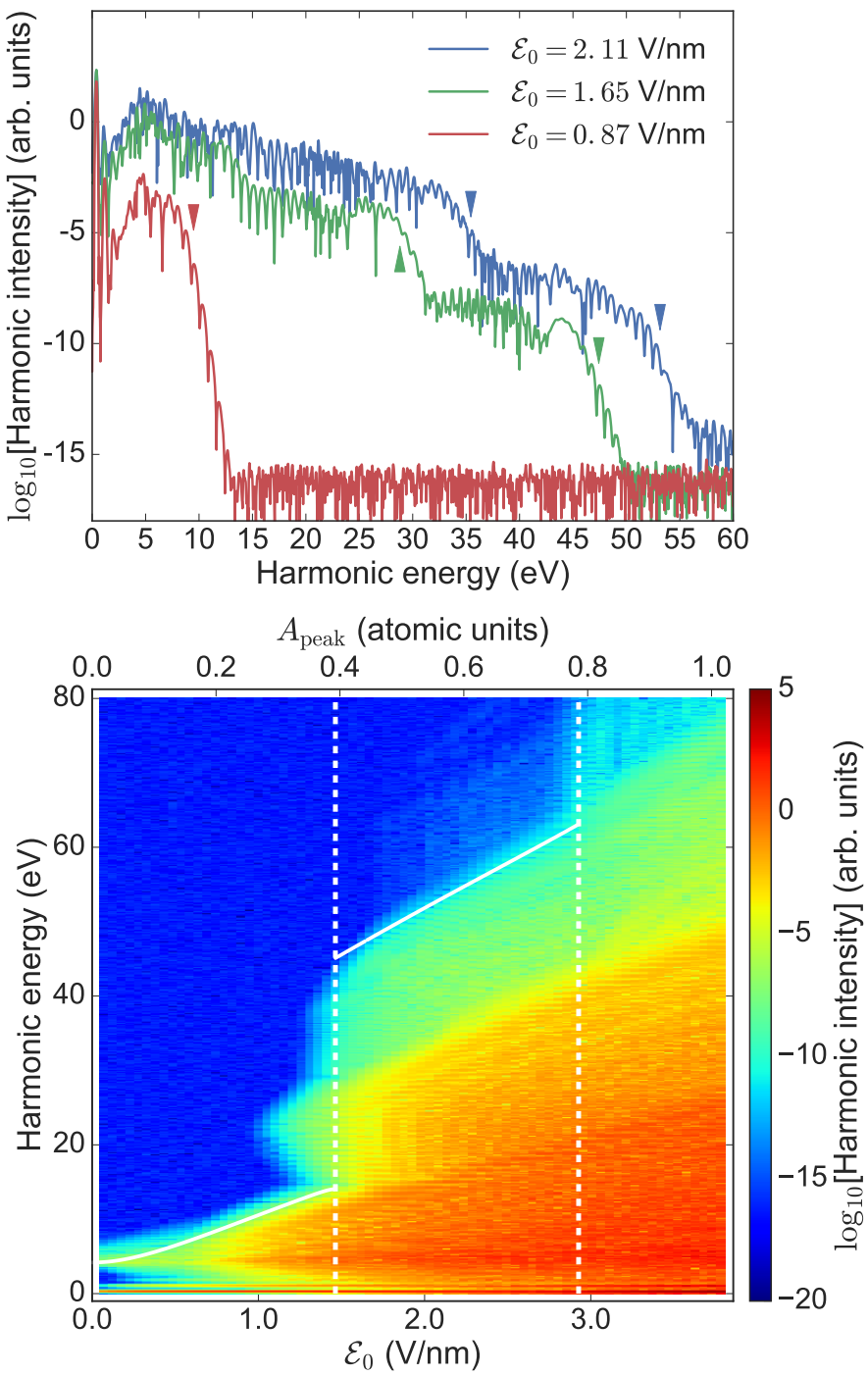

Figure 4.7: (a) High harmonic spectra for $\mathcal{E}_0 = 0.87$ V/nm (red (lower) line), $\mathcal{E}_0 = 1.65$ V/nm (green (middle) line), and $\mathcal{E}_0 = 2.11$ V/nm (blue (upper) line). Arrowheads indicate the positions given by Eq. (4.6) for $\mathcal{E}_0 = 0.87$ V/nm (red), and Eqs. (4.9) and (4.11) for $\mathcal{E}_0 = 1.65$ (green) and 2.11 (blue) V/nm. (b) False-color representation of the harmonic spectra as functions of $\mathcal{E}_0$. A_{peak} corresponding to $\mathcal{E}_0$ is shown on the top axis in atomic units. The two vertical white dashed lines represent $A_{\mathrm{peak}} = \frac{\pi}{a}$ and $\frac{2\pi}{a}$. The two white solid lines represent the cutoff energy positions given by Eq. (4.6) for $0 < A_{peak} < \frac{\pi}{a}$, and Eq. (4.9) for $\frac{\pi}{a} < A_{peak} < \frac{2\pi}{a}$.

section.

Whereas the first cutoff at $0 < A_{peak} < \frac{\pi}{a}$ and the third at $\frac{\pi}{a} < A_{peak} < 2\frac{\pi}{a}$ appear to increase quasi-linearly with the field strength [13, 27], it seems that they are closely related with the particle-hole energy, defined by Eq. (2.67),

$$\Delta\varepsilon_{\lambda\lambda'}(k) := \varepsilon_{\lambda,k} - \varepsilon_{\lambda',k}, \tag{4.5}$$

between bands λ and λ' at a crystal momentum k[1]. At $A_{peak} < \frac{\pi}{a}$, the cutoff energy agrees well with

$$\Delta\varepsilon_{21}(A_{peak}), \tag{4.6}$$

[white solid line at $\mathcal{E}_0 < 1.4$ V/nm in Fig. 4.7(b)], consistent with the formula proposed by Vampa *et al.* [45] for a two-band system. The multiple cutoff positions at $A_{peak} > \frac{\pi}{a}$, on the other hand, cannot be explained by Eq. (4.6).

4.3 Trajectory analysis

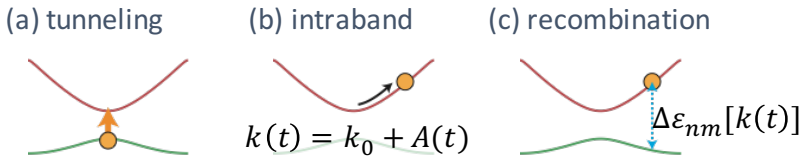

Figure 4.8: Three main processes of an electron in the momentum space; (a) tunneling excitation at the minimum band gap; (b) adiabatic intraband displacement expressed by $\dot{k} = -\mathcal{E}(t)$ or $k(t) = k_0 + A(t)$; (c) photon emission upon the interband recombination to the initial VB.

In this section, we propose a simple model to explain the above findings as well as cutoff positions for $A_{peak} > \frac{\pi}{a}$ and the time-frequency structure of HHG. Its essential ingredients are summarized as follows (Fig. 4.8):

(i) Each electron is tunnel ionized to an upper band predominantly at the MBG, e.g., from band 1 to 2 at $k = 0$ and from 2 to 3 at the BZ edge. It should, however, be noted that this is a first approximation and that the interband excitation can also take place in the vicinity of the MBG, as discussed below.

(ii) the laser-driven intraband dynamics is expressed by a displacement in the momentum space as $k(t) = k_0 + A(t)$ where k_0 denotes the initial crystal momentum [2] (this is known as the acceleration theorem [71, 76]).

(iii) Each electron emits a photon when it undergoes an interband transition to the initial band. The photon energy is given by the particle-hole energy $\Delta\varepsilon_{\lambda(t)\lambda_0}[k(t)]$ between the band $\lambda(t)$ where the electron is located at t and the initial band λ_0.

Interestingly, (i)-(iii) are reminiscent of tunneling ionization, acceleration, and recombination, respectively, in the TSM [21, 22] of gas-phase HHG. Whereas such an analogy has been suggested also in Refs. [42, 45], several remarks are in order:

[1] Given that the band structure is periodic with reciprocal lattice vector $\frac{2\pi}{a}$, we allow $k(t)$ beyond the first BZ. Alternatively, one can confine it to the first BZ by rewriting, e.g., Eq. (4.10) as $E_{31} = \Delta\varepsilon_{31}(A_{peak} - \frac{2\pi}{a})$.

[2] In situations relevant with HHG, $A(t)$ is comparable with or even larger than the BZ width.

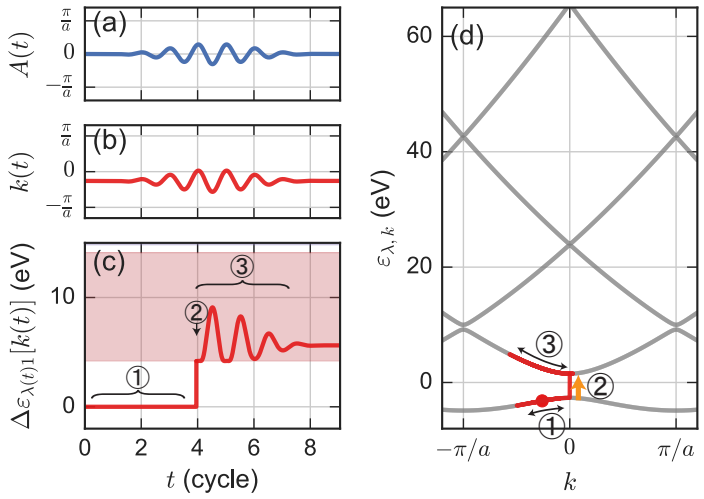

Figure 4.9: Momentum-space trajectory of an electron excited from a VB ($\lambda = 1$) to the first CB ($\lambda = 2$) at $t = 4$ cycles, drawn based on the solid-state three-step model when $\mathcal{E}_0 = 0.87$ V/nm or $A_{peak} = 0.23 < \frac{\pi}{a}$, for which $k_0 = -0.26 \times \frac{\pi}{a}$. (a) waveform of $A(t)$ (b) instantaneous crystal momentum $k(t)$ (c) temporal evolution of the particle-hole energy, i.e., emitted photon energy (d) pictorial representation of the momentum-space electron trajectory in the band diagram.

- Our solid-state TSM follows electron dynamics (and trajectories) in the momentum space whereas the gas-phase TSM considers it in the coordinate space; the momentum-space analysis is more natural and convenient for Bloch electrons in a periodic potential.
- All the electrons in the VB undergo intraband acceleration (ii) together [81, 82] even before the first tunneling. Thus, VB electrons starting from not only $k_0 = 0$ (as assumed in Refs. [29, 43]) but also any arbitrary values of k_0 should be considered [3].
- The electron can climb up to higher and higher bands by repeating (i) and (ii).
- Unlike in the gas phase, (ii) also contributes to harmonic generation [27, 41–43, 83].
- (iii) can take place at any time in a trajectory, in contrast to the atomic case where the electron can recombine with the parent ion only when it returns to the nuclear position.

4.4 HHG and electron trajectories in momentum space

In the case of gas-phase TSM, one can trace a classical electron trajectory in the coordinate space for each ionization time, which explains the cutoff law and the time-frequency structure. In the solid case, analogously, using the above-mentioned recipes, we can trace an electron trajectory in the band diagram for each time t_0 of interband tunneling at the Γ point from a VB to a CB. We present an example when $A_{peak} = 0.23 < \frac{\pi}{a}$ ($A_{peak} = 0.44 > \frac{\pi}{a}$) in Fig. 4.9 (Fig. 4.10). Note that, once given a waveform of $A(t)$ [Fig. 4.9(a) and Fig. 4.10(a)], the crystal momentum displacement can be fully described as $k(t) = k_0 + A(t)$ with $k_0 = -A(t_0)$ as shown in Fig. 4.9(b) and Fig. 4.10(b).

First, we discuss the electron dynamics when $A_{peak} < \frac{\pi}{a}$ [Fig. 4.9(d)]. Electrons initially in the valence band are accelerated (①), and excited to the CB at $k = 0$ at $t = t_0$ (②). The subsequent momentum change is given by

$$k(t) = k_0 + A(t) = A(t) - A(t_0), \tag{4.7}$$

[3]This does not violate the Pauli exclusion principle, since all the electrons in the VB move uniformly together [81, 82], and thus, no (n, k) point is occupied simultaneously by more than one electron at any time.

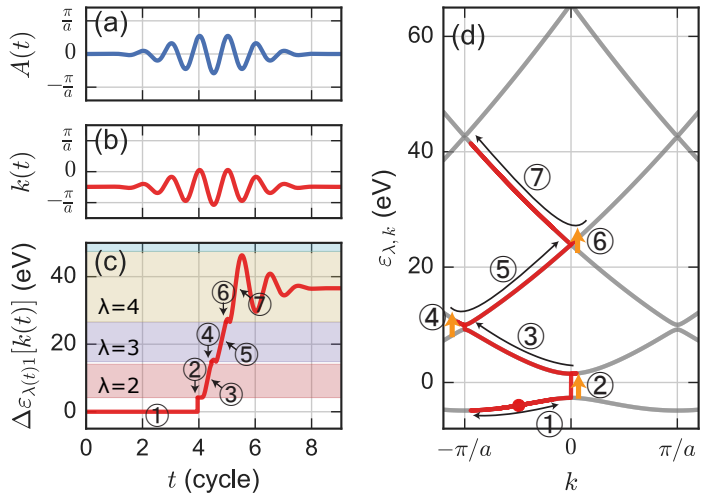

Figure 4.10: Same as Fig. 4.9, but when $\mathcal{E}_0 = 1.65$ V/nm or $A_{peak} = 0.44 > \frac{\pi}{a}$, for which $k_0 = -0.49 \times \frac{\pi}{a}$.

and hence, $|k(t)| < A_{peak}$. Thus, the maximum displacement in the first CB is A_{peak}. Now that $A_{peak} < \frac{\pi}{a}$, no electrons can reach the BZ edge, but they oscillate in the first CB without further excitation (③). Hence, the emitted photon energy is given as a function of recombination time t by $\Delta\varepsilon_{21}[k(t)]$ [Fig. 4.9(c)], and, the highest energy of the photon is given by

$$\Delta\varepsilon_{21}(A_{peak}), \tag{4.8}$$

which agrees with the cutoff position in Fig. 4.7(b) and Eq. (4.6).

Next, let us turn to the case $A_{peak} > \frac{\pi}{a}$ [Fig. 4.10(d)]. After excitation to the first CB (① - ②), part of the electrons can now be accelerated to reach the BZ edge (③), and open a channel to climb up to the upper CB (④) within a half cycle. The promoted electrons then undergo intraband displacement to the reversed direction in the second CB ($n = 3$) in the next half cycle, enabling photon emission of higher energy (⑤), which neatly explains why multiple plateaus appear at $A_{peak} \approx \frac{\pi}{a}$ [Fig. 4.7(b)]. Whereas we have assumed interband transitions precisely at the MBGs, they can also take place in their vicinities in reality. This explains the appearance of some high-energy components even before A_{peak} reaches $\frac{\pi}{a}$ in Fig. 4.7(b), from $\mathcal{E}_0 \sim 1.1$ V/nm.

Every time the electrons reach the MBG to the next CB each half cycle, they can undergo successive interband excitation (⑤ - ⑦) (or pass through it). If the second maximum peak-to-valley amplitude is denoted by $A_{peak}{}'$ (Fig. 4.3), they can climb up to the third CB ($n = 4$) if $A_{peak}{}' < \frac{\pi}{a}$ and the fourth CB ($n = 5$) if $A_{peak}{}' > \frac{\pi}{a}$ at $t \approx 5.5T$ with T being the optical cycle. From this scenario, we can estimate the maximum energy gain as

$$E_c = \begin{cases} \Delta\varepsilon_{41}(A_{peak}{}') & (A_{peak}{}' < \frac{\pi}{a}) \\ \Delta\varepsilon_{51}(A_{peak}{}') & (\frac{\pi}{a} < A_{peak}{}'), \end{cases} \tag{4.9}$$

which reproduces the highest harmonic energy in Fig. 4.7(b). It should be noted that the highest cutoff energy can exceed that seen in the gas phase for the same laser parameters and ionization potential (band gap energy in the solid case), as has been recently observed [29].

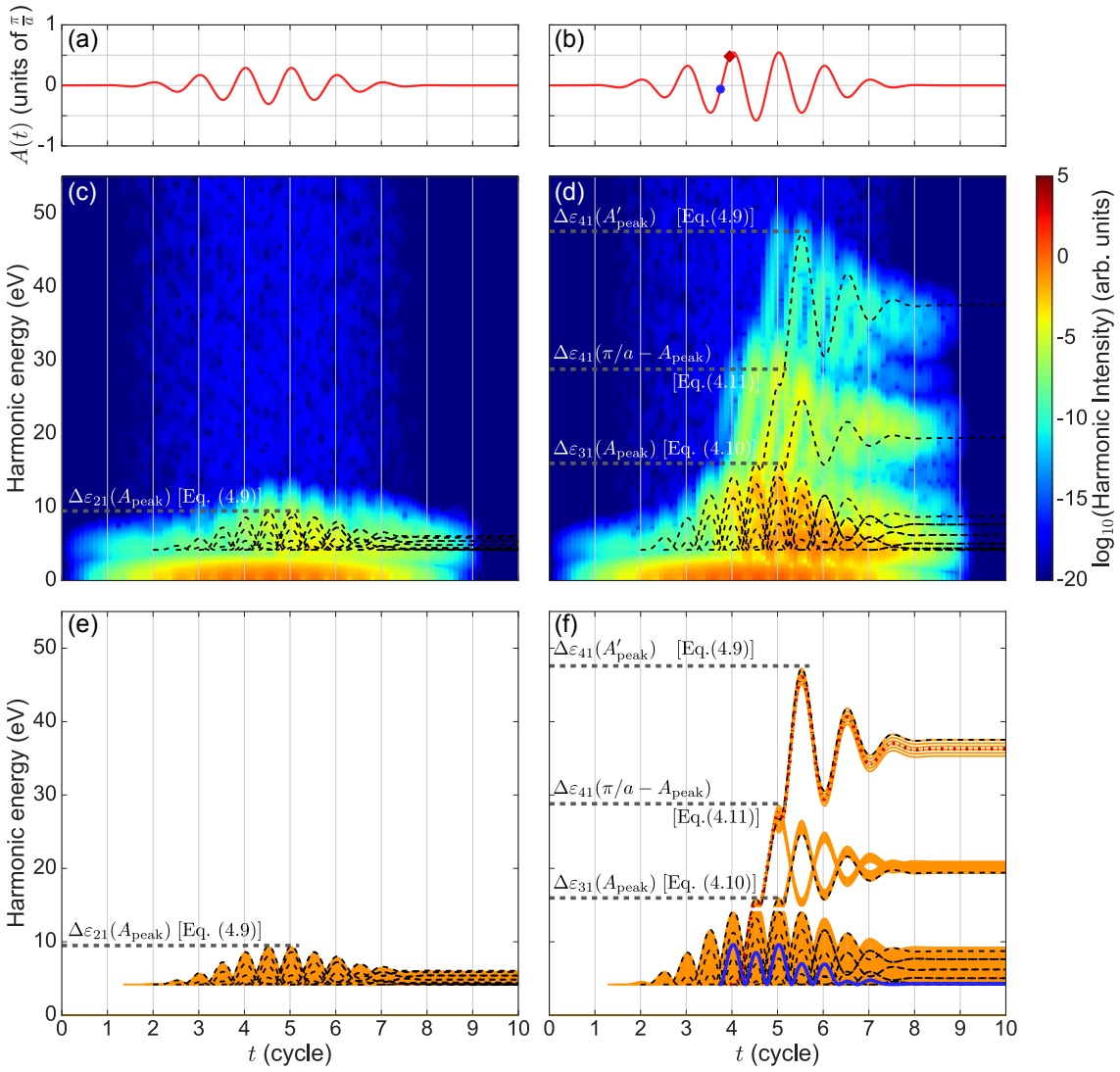

Figure 4.11: The temporal evolution of high harmonic generation. (a), (c), and (e) are for $\mathcal{E}_0 = 0.87$ V/nm or $A_{peak} = 0.23 < \frac{\pi}{a}$, while (b), (d), and (f) are for $\mathcal{E}_0 = 1.65$ V/nm or $A_{peak} = 0.44 > \frac{\pi}{a}$. (a) and (b):vector potential normalized to π/a. (c) and (d):time-frequency analysis of HHG. Gabor transform of the TDSE simulation results with a temporal window having a FWHM of 1.78 fs, i.e., 2.3 eV in energy. (e) and (f): orange solid lines denote electron energy trajectories that first tunnel from the VB to the first CB at $k = 0$ at different momenta (not necessarily at the first approach) and then climb to upper bands as soon as the electron reaches the minimum band gaps. The blue solid line in (f) represents the trajectory of an electron which is first tunnel-ionized at $A(t) \sim 0$ [blue circle in (b)], whereas the red dash-dotted line in the vicinity of the peak of $A(t)$ [red diamond in (b)]. In (c) and (d) we show by black dashed lines the trajectories corresponding to the black dashed lines in (e) and (f), respectively, to facilitate comparison. The horizontal gray dashed lines in (c), (d), (e), and (f) show the predicted cutoff energy positions, i.e., $\Delta\varepsilon_{21}(A_{peak})$ for (c) and (e) ($A_{peak} = 0.23$), and $\Delta\varepsilon_{31}(A_{peak})$, $\Delta\varepsilon_{41}(\frac{\pi}{a} - A_{peak})$, and $\Delta\varepsilon_{41}(A_{peak}{}')$ from the bottom for (d) and (f) ($A_{peak} = 0.44$), respectively.

4.4.1 Temporal structures of HHG

The temporal profile of the photon energy emitted from the trajectory in Fig. 4.9(d) [Fig. 4.10(d)] is given by Fig. 4.9(c) [Fig. 4.10(c)], since the electron can recombine with the VB hole at any time, as prescribed. By accumulating similar curves for all possible values of t_0 and climb-up-or-pass-through branchings, one can deduce the time-frequency structure of HHG, as displayed in Fig. 4.11(e) and (f). They indeed capture the main features of the HHG temporal structure, extracted from The TDSE simulation results through Gabor transformation, above the band gap energy 4.2 eV [Fig. 4.11(c) and (d)]. The below-band-gap harmonics are emitted through the intraband dynamics.

The temporal structure under $A_{peak} < \frac{\pi}{a}$ shown in Fig. 4.11(c) is consistent with that previously discussed by Vampa *et al.* [45]. It is also noteworthy that these electron dynamics are conceptually similar to that in harmonic generation from graphene [84–86]. For $A_{peak} > \frac{\pi}{a}$, in contrast, Fig. 4.11(d) and (f) contain step-like features, stemming from the band-climbing process [4] unique to solid-state materials; they manifest themselves as multiple plateaus and cutoffs seen in Fig. 4.7. Some step heights indicated with the horizontal dashed lines in Fig. 4.11(f) are characterized by

$$E_{31} = \Delta\varepsilon_{31}(A_{peak}), \tag{4.10}$$

$$E_{41} = \Delta\varepsilon_{41}(\frac{\pi}{a} - A_{peak}), \tag{4.11}$$

which well agree with the TDSE simulation results [horizontal dashed lines in Fig. 4.11(d) and arrowheads in Fig. 4.7(a)]. The remaining difference between Fig. 4.11(d) and (f) can be accounted for again by interband transition not just precisely at the minimum band gap but also in its vicinity. Note that $-\frac{\pi}{a} < \frac{\pi}{a} - A_{peak} < 0$, and therefore, that E_{41} increases with increasing A_{peak}.

Electrons starting from $k_0 \sim 0$ are excited when $A(t) \approx 0$, or, at an extremum of $\mathcal{E}(t)$ [the blue circle in Fig. 4.11(b)], which favors tunneling transition. On this basis, one might argue that they would make a main contribution to HHG [45]. It should, however, be noticed that they cannot reach the BZ edge and are confined to the first CB [blue line in Fig. 4.11(f)] unless $A_{peak} \geq \frac{2\pi}{a}$. As a consequence, their contributions are limited to the range below E_{31}. In contrast, the harmonic components above E_{31} including the highest cutoff are dominated by the electrons [red line in Fig. 4.11(f)] that are initially far from the Γ point and first excited in the vicinity of a peak of $A(t)$ [the red circle in Fig. 4.11(b)] or $\mathcal{E}(t) \approx 0$, thus with smaller probability. This may be one of the reasons why higher plateaus are weaker in intensity.

4.4.2 Pulse duration and HHG spectra

An intriguing prediction of the present model is that the number of plateaus and the highest cutoff energy depend not only on wavelength and electric field amplitude (or vector potential amplitude) but also on pulse width or number of cycles, in marked contrast to gas-phase HHG. This is confirmed by Fig. 4.12, which compares harmonic spectra for single-cycle ($\tau = 42.70$ fs) and multi-cycle ($\tau = 192.14$ fs) driving fields. One can clearly see that the third plateau is missing at $0.39 < A_{peak} < 0.79$ for the shorter pulse.

[4] This somewhat reminds us of *Donkey Kong*, an arcade game released by Nintendo (https://en.wikipedia.org/wiki/Donkey_Kong_(video_game))

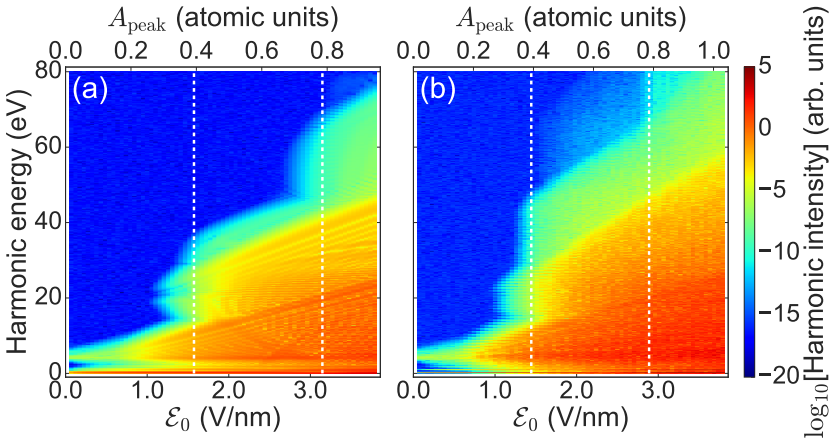

Figure 4.12: False-color representation of HHG spectra as functions of $\mathcal{E}_0$ for (a) single-cycle driving field ($\tau = 42.70$ fs) and (b) multi-cycle field ($\tau = 192.14$ fs). The corresponding A_{peak} is shown on the top axis in the atomic unit. The vertical white dashed lines represent $A_{peak} = \frac{\pi}{a}$ and $\frac{2\pi}{a}$.

4.5 Experimentally observed multiple plateau

In this section, let us look into the multiple-plateau harmonic spectra experimentally observed in Ref. [29] (see also Fig. 1.7 in Ch. 1), focusing on the field strength at which the higher plateau appears. We use the experimental data[5] used in Fig. 1.7(c), harmonic spectra from solid Ar as functions of laser intensity ($\lambda = 1333$ nm).

The values of $A_{\rm peak}$ inside the sample are estimated from the laser intensities $I_{\rm vac}$ in vacuum given in the experimental data, which were calibrated using the measured spectral cutoff energy positions of HHG in the Ar and Kr gases [29]. First, we convert the field intensities $I_{\rm vac}$ into the field strengths $\mathcal{E}_{\rm vac}$ in vacuum using the relation

$$I_{\rm vac} = \mathcal{E}_{\rm vac}^2, \tag{4.12}$$

in atomic units. These field strengths $\mathcal{E}_{\rm vac}$ in vacuum are converted into the field strengths $\mathcal{E}_0$ inside the sample using

$$\mathcal{E}_0 = \frac{2}{1+n}\mathcal{E}_{\rm vac}, \tag{4.13}$$

with $n \approx 1.3$ denoting the refractive index of solid Ar [87]. Next, the field strengths $\mathcal{E}_0$ are converted into the amplitude of vector potential A_0 inside the crystal using

$$A_0 \approx \frac{\mathcal{E}_0}{\omega}, \tag{4.14}$$

where $\omega = 2\pi c/\lambda$ denotes the angular frequency of the field. Finally, the values of $A_{\rm peak}$ are approximated as

$$A_{\rm peak} \approx 2A_0, \tag{4.15}$$

assuming an ordinal waveform whose pulse duration is more than few cycles. The harmonic spectra are shown as functions of $\mathcal{E}_0$ and $A_{\rm peak}$ in Fig. 4.13[6].

Solid Ar has a face-centered cube (fcc) crystal structure, that is, a conventional cubic cell of edge length

[5] The source data is available in the online version of Ref. [29].

[6] It should be noted here that the values of harmonic intensities of the data offered in the online version of Ref. [29] are inconsistent with those of the corresponding figure in the paper.

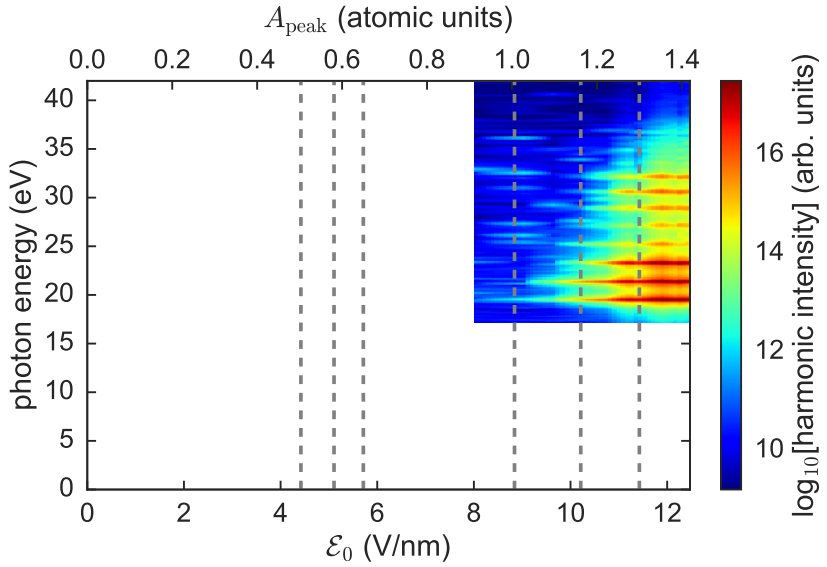

Figure 4.13: False-color representation of HHG spectra of solid Ar using 1333-nm driving field as functions of $\mathcal{E}_0$ and $A_{\rm peak}$ reported in Ref. [29]. The dashed vertical lines represents the positions of $A_{\rm peak} = |\Gamma X|, |\Gamma L|, |\Gamma W|$ (left three lines) and $A_{\rm peak} = 2|\Gamma X|, 2|\Gamma L|, 2|\Gamma W|$ (right three lines).

a with atoms at the corners and at the center of the faces [Fig. 4.14(a)] [77]. The lattice constant $a = 5.62$ for Ar [77]. The primitive lattice vectors are given by $\boldsymbol{a}_1 = \frac{a}{2}(0,1,1)$, $\boldsymbol{a}_2 = \frac{a}{2}(1,0,1)$, and $\boldsymbol{a}_3 = \frac{a}{2}(1,1,0)$. Figure 4.14(b) shows the BZ for the fcc lattice. Some high symmetry points are denoted as $\Gamma = (0,0,0)$, $X = \frac{2\pi}{a}(1,0,0)$, $L = \frac{2\pi}{a}(\frac{1}{2},\frac{1}{2},\frac{1}{2})$, and $W = \frac{2\pi}{a}(\frac{1}{2},1,0)$. Therefore, the condition that corresponds to $A_{\rm peak} = \frac{\pi}{a}$ in 1D system would be represented by

$$A_{\rm peak} = |\Gamma X| = 0.581, \tag{4.16}$$

$$A_{\rm peak} = |\Gamma L| = 0.503, \tag{4.17}$$

$$A_{\rm peak} = |\Gamma W| = 0.650, \tag{4.18}$$

which are shown by vertical dashed lines in Fig. 4.13.

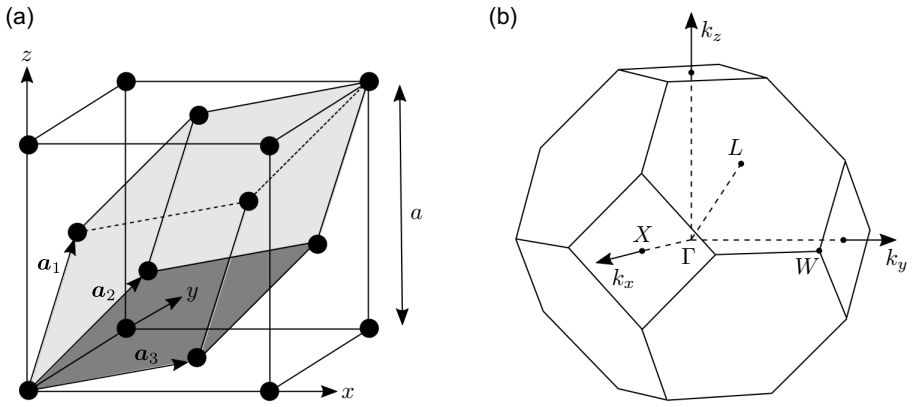

Figure 4.14: (a) Face-centered cubic crystal structure.

Unfortunately, as their experimental data does not cover the area $A_{\text{peak}} = |\Gamma X|, |\Gamma L|, |\Gamma W|$, we cannot check the multiple-plateau appearance at those field strengths. Solid Ar has a large band gap energy of ~ 14 eV [88]. This is expected to make the electron tunneling probability at the Γ point significantly small, and consequently, the HHG signal undetectable until the field strength becomes more intense. This may be why their data starts at $\mathcal{E}_0 \sim 8$ V/nm.

In general, electrons starting from the vicinity of the Γ point are expected to make the most dominant contribution for radiation, and thus their signal are expected to be easier to detect. For these electrons, the conditions to reach the BZ edge are given by

$$A_{\text{peak}} = 2|\Gamma X| = 1.162, \tag{4.19}$$

$$A_{\text{peak}} = 2|\Gamma L| = 1.006, \tag{4.20}$$

$$A_{\text{peak}} = 2|\Gamma W| = 1.300, \tag{4.21}$$

which are shown as vertical dashed lines in Fig. 4.13. The multiple-plateau appearance seems to coincide with these conditions. As there is no other data that has observed the multiple-plateau structure with series of spectra as functions of field strengths, more experimental investigation is needed to discuss the applicability of our trajectory analysis based on the momentum-space three-step model of solid electrons.

4.6 Conclusions

We have proposed a simple model to describe HHG spectra from periodic crystalline solids, based on intraband displacement driven by the vector potential, tunneling between multiple bands, and interband recombination to the valence band. Our model can be viewed as a solid-state and momentum-space counterpart of the familiar TSM for the gas phase [21, 22]. If the intraband dynamics allows the electron to reach the BZ edge, repeated tunneling and intraband displacement lead to multiple plateaus, which is one of the recently observed unique features of solid-state HHG [29, 43, 49]. Our model can successfully reproduce the laser intensity at which the multiple-plateau structure appears, cutoff energy positions, and temporal structure of HHG calculated through the single-electron TDSE. Moreover, it predicts that the cutoff energy depends on not only laser intensity and wavelength but also pulse width.

It may be useful to briefly mention the similarity and difference between our model and the recently proposed model of a strongly driven (or dressed) multi-level system [29, 50]. Assuming that the dressed state ultimately reproduces the band structure, their model appears to describe the physics similar to that in our model, in principle. It should be, however, emphasized that whereas their model considers the contribution only from the VB electron initially located at $k = 0$, we properly take the contribution from all the VB electrons into account. Moreover, by treating the intraband dynamics explicitly as the crystal momentum displacement induced by the vector potential of the laser pulse, our model can directly connect the emergence of multiple plateaus and cutoff energies with the band structure in a clear-cut manner.

Thus, our model will offer a new way to investigate and control the electronic state in solid materials with intense laser fields, such as the reconstruction of band structure from high-harmonic spectra and control of excited electron population via waveform.

5

TDHF Study of Electron-Hole Interaction Effects on HHG in Solids

While most of the previous works [13, 27, 32–34, 37, 41, 42, 50, 55, 67, 68] have used the independent-electron approximation, the role of electron-hole interactions in solids in the strong-field regime is largely unexplored. Although the independent-electron picture has worked very well to describe the high-harmonic generation processes in atoms and molecules [21–23], its applicability in solids is questionable, as tunnel-excited electrons in solids move through a sea of other spatially spread electrons. Garg *et al.* have recently suggested that electron-hole interaction affects harmonic yields from silicon dioxide using semiconductor-Bloch equations incorporating the interelectronic interaction [30]. It is required to investigate the interplay between strong-field-driven individual electron dynamics and dynamical electron-hole interaction effects in an ultrafast time-scale beyond the independent-electron picture.

In this work, we study the effects of the electron-hole interaction on solid-state high-harmonic generation by numerically solving the time-dependent Hartree-Fock theory (Sec. 2.1.2). Our results for a one-dimensional model crystal show that electron-hole interaction qualitatively modifies harmonic spectra from what is expected with the independent-electron approximation simulations. Using the Houston basis, we reveal its origin in terms of the electron-hole polarization. This chapter is largely reprinted from our recent submitted work [89]. Reprinted excerpt from Takuya Ikemachi, Yasushi Shinohara, Takeshi Sato, Junji Yumoto, Makoto Kuwata-Gonokami, Kenichi L. Ishikawa, arXiv:1709.08153 [physics.optics] (2017).

5.1 Model

5.1.1 TDHF theory

We consider a 1D system spanning $x \in [-ma, ma]$, which contains $N_{\text{cell}} = 2m + 1$ unit cells, with a denoting the lattice constant. 1D models have previously been used in several works [43, 46, 52, 53, 67] to study the fundamental nature of solid-state HHG and turned out to be useful. Moreover, a 1D system has a strong electron-hole correlation [78], and thus, should be suitable for the investigation of electron-hole interaction (EHI). The set of the spin-restricted TDHF equations in the velocity gauge Eq. (2.42), for an electron orbital ψ_{bk_0} that *initially* lies in band b with crystal momentum k_0 in a 1D system, is given by

$$\begin{aligned} i\frac{\partial}{\partial t}\psi_{b,k_0}(x,t) &= \hat{h}(t)\psi_{b,k_0}(x,t) \\ &= \left[\frac{1}{2}\left(\frac{\nabla}{i} + A(t)\right)^2 + v_1(x) + \hat{w}[\rho(t)]\right]\psi_{b,k_0}(x,t), \end{aligned} \tag{5.1}$$

where $A(t) = -\int_{-\infty}^{t} \mathcal{E}(t')dt'$ denotes the vector potential of the electric field $\mathcal{E}(t)$, $v_1(x)$ the periodic potential from the crystal nuclei (2.15), $w[\rho(t)](x,x') = v_{\mathrm{H}}[\rho(t)](x)\delta(x-x') + v_{\mathrm{x}}[\rho(t)](x,x')$ the interelectronic operator composed of the Hartree operator (2.18), and the interelectronic exchange operator (2.19), respectively, and the density matrix $\rho(x,x',t)$ is given by

$$\rho(x,x',t) = 2\sum_{b\in \mathrm{VB},\ k_0} \psi_{b,k_0}(x,t)\,\psi^*_{b,k_0}(x',t). \tag{5.2}$$

The initial state of $\psi_{b,k_0}(x,t)$ is the self-consistent eigenstate $\phi_{b,k_0}(x)$ of the field-free Hartree-Fock Hamiltonian,

$$\hat{h}_0 = -\frac{\nabla^2}{2} + v_1(x) + \hat{w}[\rho_0], \tag{5.3}$$

where the ground state density matrix ρ_0 is given by

$$\rho_0(x,x') = 2\sum_{b,k_0} \phi_{b,k_0}(x)\phi^*_{b,k_0}(x'). \tag{5.4}$$

The field-induced current is obtained by Eq. (2.57) and (2.58).

We use a soft-Coulomb potential

$$v(x-x') = \frac{1}{\sqrt{(x-x')^2+1}} \tag{5.5}$$

for both electron-nucleus and electron-electron interactions. This soft-Coulomb potential for a 1D system can be obtained by considering a 1D quantum wire and averaging the three-dimensional Coulomb potential with the radial envelope functions [78], which has been used to discuss the linear response of semiconductor quantum wires [90, 91] as well as strong-field HHG and ionization of gas-phase molecules [92–94]. Using the soft-Coulomb potential Eq. (5.5), we have

$$v_1(x) = -\sum_I \frac{z_I}{\sqrt{(x-x_I)^2+1}}, \tag{5.6}$$

$$v_{\mathrm{H}}[\rho(t)](x) = \int dx' \frac{\rho(x',x',t)}{\sqrt{(x-x')^2+1}}, \tag{5.7}$$

$$v_{\mathrm{x}}[\rho(t)](x,x') = -\frac{1}{2}\frac{\rho(x,x',t)}{\sqrt{(x-x')^2+1}}, \tag{5.8}$$

where z_I and x_I represent the charge and position of a nucleus I, respectively.

Applying Bloch's theorem discussed in Ch. 2, we decompose the time-dependent orbital as $\psi_{b,k_0}(x,t) = \frac{1}{\sqrt{N_k}} e^{ik_0 x} u_{b,k_0}(x)$ and solve the EoM given by Eq. (2.44),

$$\begin{aligned} i\frac{\partial}{\partial t}u_{b,k_0}(x,t) = &\left[\frac{1}{2}\left(\frac{\nabla}{i} + k_0 + A(t)\right)^2 + v_1(x) + v_{\mathrm{H}}[\rho(t)](x)\right] u_{b,k_0}(x,t) \\ &+ \int_\Omega dx' v^{\Omega}_{\mathrm{x},k_0}[\rho(t)](x,x') u_{b,k_0}(x',t), \end{aligned} \tag{5.9}$$

where the density matrix $\rho(t)$, the Hartree operator $v_{\mathrm{H}}[\rho(t)](x)$, and the exchange operator $v^{\Omega}_{\mathrm{x},k}[\rho(t)](x,x')$

are given by,

$$\rho(x,x',t) = \frac{2}{N_k}\sum_{b\in \mathrm{VB},\ k_0} u_{b,k_0}(x,t)u^*_{b,k_0}(x',t) \tag{5.10}$$

$$v_{\mathrm{H}}[\rho(t)](x) = 2\sum_{b,k_0}\int_\Omega dx' |u_{b,k_0}(x',t)|^2 v_0^\Omega(x-x') \tag{5.11}$$

$$v^\Omega_{\mathrm{x},k}[\rho(t)](x,x') = -\sum_{b,k_0} u_{b,k_0}(x,t)u^*_{b,k_0}(x',t)v^\Omega_{k-k_0}(x-x'), \tag{5.12}$$

where

$$v_k^\Omega(x) = \frac{1}{N_k}\sum_T v(x+T)e^{-ik(x+T)} = \frac{1}{N_k}\sum_T \frac{e^{-ik(x+T)}}{\sqrt{(x-x'-T)^2+1}}, \tag{5.13}$$

with $T = -ma, -(m-1)a, \ldots, ma$ denoting the lattice translation vector.

5.1.2 Frozen TDHF theory

In parallel, we perform simulations without EHI using the *frozen* TDHF Hamiltonian $\hat{h}_f(t)$, whose interelectronic Coulomb and exchange operators are generated by static ground state orbitals,

$$i\frac{\partial}{\partial t}\psi^f_{b,k_0}(x,t) = \hat{h}_f(t)\psi^f_{b,k_0}(x,t) \tag{5.14}$$

$$= \left[\frac{1}{2}\left(\frac{\nabla}{i}+A(t)\right)^2 + v_1(x) + \hat{w}[\rho_0]\right]\psi^f_{b,k_0}(x,t), \tag{5.15}$$

where the frozen interelectronic operator $\hat{w}[\rho_0]$ is given by

$$w[\rho_0](x,x') = v_{\mathrm{H}}[\rho_0](x)\delta(x-x') + v_{\mathrm{x},A(t)}[\rho_0](x,x'). \tag{5.16}$$

The frozen exchange operator generated from the static ground state has a dependence on the vector potential $A(t)$ as,

$$v_{\mathrm{x},A(t)}[\rho_0](x,x') = e^{-iA(t)x}v_{\mathrm{x}}[\rho_0](x,x')e^{iA(t)x'}, \tag{5.17}$$

because it is a nonlocal potential (see the discussion in Sec. 2.2). This corresponds to the IEA discussed in the previous chapter Ch. 4, where each electron moves independently in the potential constructed by the ground state Bloch functions. I note that the *full* TDHF Hamiltonian can be written as

$$\hat{h}(t) = \hat{h}_f(t) + \hat{w}[\delta\rho(t)], \tag{5.18}$$

whose second term corresponds to EHI, with

$$\delta\rho(t) = \rho(t) - \rho_0. \tag{5.19}$$

Applying Bloch's theorem $\psi^f_{b,k_0}(x,t) = \frac{1}{\sqrt{N_k}}e^{ik_0x}u^f_{b,k_0}(x,t)$, we solve the EoM for $u^f_{b,k_0}(x,t)$ given by

$$i\frac{\partial}{\partial t}u^f_{b,k_0}(x,t) = \left[\frac{1}{2}\left(\frac{\nabla}{i}+k_0+A(t)\right)^2 + v_1(x) + v_{\mathrm{H}}[\rho_0](x)\right]u^f_{b,k_0}(x,t) + \int_\Omega dx' v^\Omega_{\mathrm{x},k_0+A(t)}[\rho_0](x,x')u^f_{b,k_0}(x',t). \tag{5.20}$$

Using the lattice periodic part of the initial Bloch function defined as

$$\phi_{b,k_0}(x) = \frac{1}{\sqrt{N_k}} e^{ik_0 x} u^0_{b,k_0}(x), \tag{5.21}$$

the ground-state density matrix, the Hartree operator and exchange operator are given by

$$\rho_0(x,x') = \frac{2}{N_k} \sum_{b\in \mathrm{VB},\ k_0} u^0_{b,k_0}(x) u^{0*}_{b,k_0}(x'), \tag{5.22}$$

$$v_{\mathrm{H}}[\rho_0](x) = 2\sum_{b,k_0} \int_\Omega dx' |u^0_{b,k_0}(x')|^2 v^\Omega_0(x-x'), \tag{5.23}$$

$$v_{\mathrm{x},k+A(t)}[\rho_0](x,x') = -\sum_{b,k_0} u^0_{b,k_0}(x) u^{0*}_{b,k_0}(x') v^\Omega_{k-k_0+A(t)}(x-x'). \tag{5.24}$$

As the frozen TDHF Hamiltonian contains a nonlocal operator, the current density $j(t)$ is given by Eq. (2.50),

$$j(t) = \frac{1}{N_k a} \langle \hat{p} + A(t) \rangle + j_{\mathrm{nl}}(t), \tag{5.25}$$

where the contribution from the nonlocal operator $v_{\mathrm{x},A(t)}[\rho_0]$ is obtained as

$$j_{\mathrm{nl}}(t) = \frac{4}{N_k a} \mathrm{Im} \sum_{b,k_0} \int_\Omega dx \int_\Omega dx' u^{f*}_{b,k_0}(x) x v^\Omega_{\mathrm{x},k_0+A(t)}[\rho_0](x,x') u^f_{b,k_0}(x',t). \tag{5.26}$$

The details of the derivation of $j_{\mathrm{nl}}(t)$ is given in Appendix E.

5.1.3 Simulation system and Convergence properties

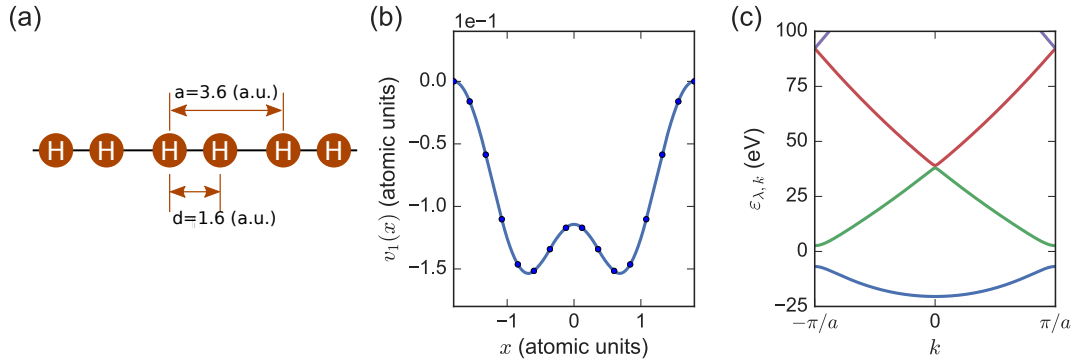

Figure 5.1: (a) Schematic illustration of the model 1D hydrogen chain. (b) The atomic potential $v_1(x)$ produced by the hydrogen atoms in a unit cell. (c) The band structure of this system obtained by the ITP method with the field-free TDHF Hamiltonian.

We consider a 1D model crystal along laser polarization. Specifically, our system is a 1D model hydrogen chain insulator with a lattice constant of $a = 3.6$, composed of a series of hydrogen dimers whose bond length $d = 1.6$ [Fig. 5.1(a)]. Figure 5.1(b) shows the nuclei potential in a unit cell. Figure 5.1(c) shows the band structure, the set of the energy eigenvalues $\varepsilon_{\lambda,k_0}$, with a gap energy of 9.5 eV. The lowest band is an initially fully occupied VB. We numerically integrate the TDHF equations (5.9) and its counterpart with the frozen TDHF Hamiltonian $\hat{h}_f(t)$ (5.15) for a laser field $\mathcal{E}(t) = \mathcal{E}_0 \sin^2(t/\tau)\sin(\omega t)$ with $\tau = 702.3$ (5 cycle), $\hbar\omega = 0.387$ (eV), where $\mathcal{E}_0$ denotes the field amplitude.

I show the convergence properties of the real-time TDHF simulation. Here, as we are interested in general aspects of harmonic spectra such as multiple-plateau structures and cutoff energy positions, we don't need a convergence in detail but in qualitative structures of harmonic spectra for several typical field strength. Figure 5.2 shows comparison of the harmonic spectra for several number of spatial grid points $N_{\rm grid}$ with one that is sufficiently converged ($N_{\rm grid} = 19$). We have a sufficient convergence with $N_{\rm grid} = 15$, which corresponds to the grid spacing $\Delta x = a/N_{\rm grid} = 0.24$.

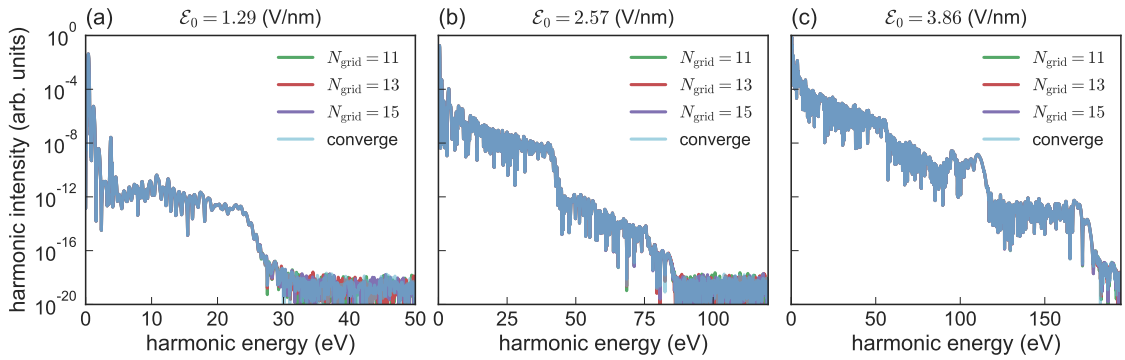

Figure 5.2: Harmonic spectra for (a) $\mathcal{E}_0 = 1.29$ V/nm, (b) $\mathcal{E}_0 = 2.57$ V/nm and (c) $\mathcal{E}_0 = 3.86$ V/nm with number of real-space grid $N_{\rm grid} = 11, 13, 15$ and $N_{\rm grid} = 19$ (labeled as convergence). In these simulations, we use $N_k = 201$ and $N_{\rm step} = 1 \times 10^5$.

We have also checked the convergence with respect to the number of temporal steps in a cycle (Fig. 5.3). From these results, we have a sufficient convergence with $N_{\rm step} = 10 \times 10^5$, or a temporal step size $\Delta t = 4.4 \times 10^{-3}$.

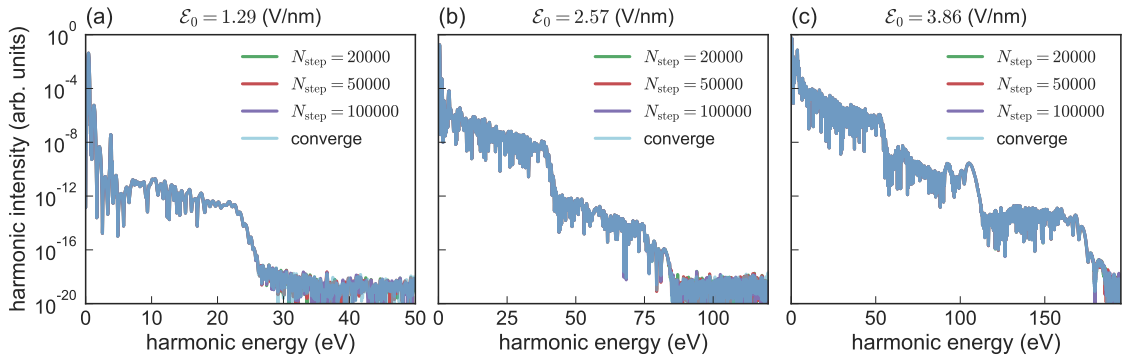

Figure 5.3: Harmonic spectra for (a) $\mathcal{E}_0 = 1.29$ V/nm, (b) $\mathcal{E}_0 = 2.57$ V/nm and (c) $\mathcal{E}_0 = 3.86$ V/nm with number of time steps in a cycle $N_{\rm step} = 2 \times 10^4, 5 \times 10^4, 1 \times 10^5$ and $N_{\rm step} = 2 \times 10^5$ (labeled as convergence). In these simulations, we use $N_k = 201$ and $N_{\rm grid} = 15$.

Figure 5.4 shows the convergence of harmonic spectra with respect to the number of k-points N_k. We have a sufficient convergence with $N_k = 201$.

We have also checked the convergence of the harmonic spectra in the frozen TDHF simulations (Fig. 5.5). As shown in Fig. 5.5, we have found that the harmonic spectra in the frozen simulations shows a good convergence for the same parameters required to converge the full TDHF calculation. Hence, we use the same parameters as the TDHF for the frozen TDHF simulations.

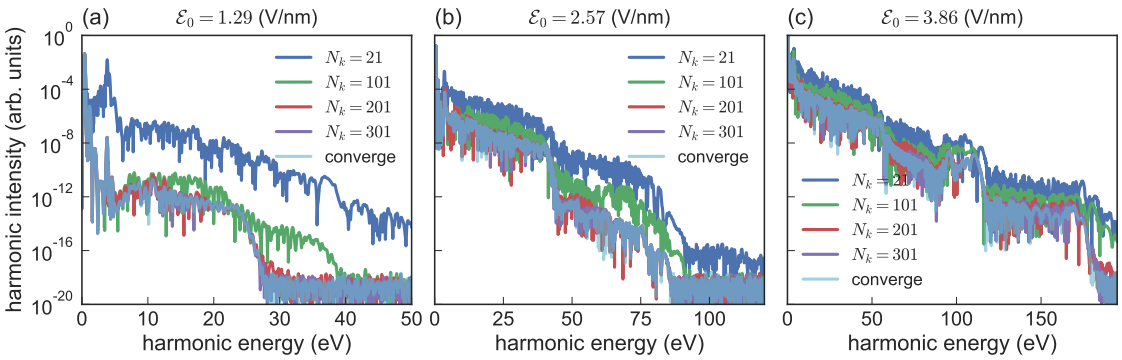

Figure 5.4: Harmonic spectra for (a) $\mathcal{E}_0 = 1.29\,\mathrm{V/nm}$, (b) $\mathcal{E}_0 = 2.57\,\mathrm{V/nm}$ and (c) $\mathcal{E}_0 = 3.86\,\mathrm{V/nm}$ with $N_k = 21, 101, 201, 301$ and $N_k = 401$ (labeled as convergence). In these simulations, we use $N_{\mathrm{grid}} = 15$ and $N_{\mathrm{step}} = 1 \times 10^5$.

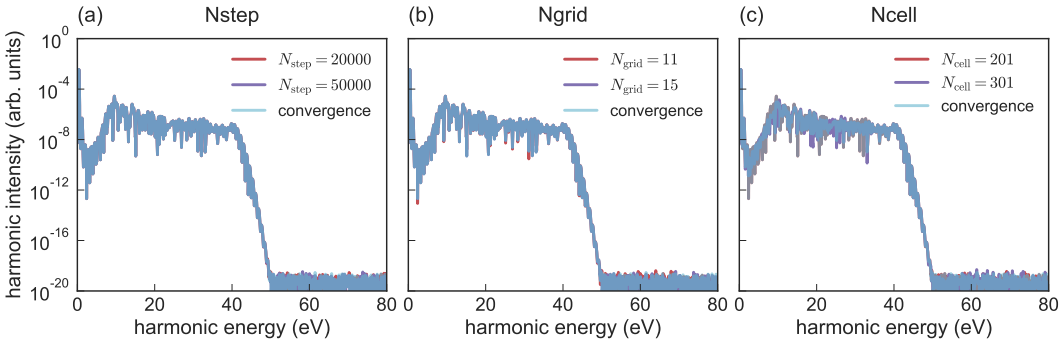

Figure 5.5: Harmonic spectra obtained from the frozen TDHF simulations for $\mathcal{E}_0 = 2.57\,\mathrm{V/nm}$. (a) Harmonic spectra with $N_{\mathrm{step}} = 20000, 50000$ and 200000 (labeled as convergence). (b) Harmonic spectra with $N_{\mathrm{grid}} = 11, 15$ and 19 (labeled as convergence). (c) Harmonic spectra with $N_{\mathrm{cell}} = 201, 301$ and 401 (labeled as convergence).

5.2 Simulation results and discussions

We show representative harmonic spectra for several field strength in Fig. 5.6. We first notice an exciton peak at 3.8 eV below the gap energy at low intensity [Fig. 5.6(a)], which indicates that the TDHF simulations capture EHI appropriately (see Appendix C for the exciton energy and linear response). Note that TDDFT at present cannot reproduce excitons, which is based on the simple ALDA in practical implementations [60]. While each of the harmonic spectra obtained by the frozen TDHF and the TDHF for $\mathcal{E}_0 = 1.06\,\mathrm{V/nm}$ [Fig. 5.6(a)] and for $\mathcal{E}_0 = 3.47\,\mathrm{V/nm}$ [Fig. 5.6(c)] have a similar structure as a whole, those for $\mathcal{E}_0 = 2.60\,\mathrm{V/nm}$ look qualitatively different. The spectrum from the TDHF has a clear additional plateau at 50-80 eV, whereas the frozen TDHF has only a single plateau.

In order to see this in more detail, we show harmonic spectra as functions of the field amplitude $\mathcal{E}_0$ and its corresponding A_{peak}, the maximum peak-to-valley amplitude of the vector potential $A(t)$ [see the inset of Fig. 5.10(a)] in Fig. 5.7. In the case of the *frozen* TDHF [Fig. 5.7(a)], i.e., within the IEA, the appearance of multiple plateaus at $A_{\mathrm{peak}} = \frac{\pi}{a} = 0.87$ and the cutoff positions can be understood on the basis of the solid-state momentum-space three-step model [50, 67, 68] presented in Ch. 4. Although details can be seen in § 4.3 for detail, it would be useful to summarize again the essential point of the model. A typical trajectory is depicted in Fig. 5.10(a). An electron initially in the VB undergoes intraband displacement and gets excited at the MBG $k = \pm\frac{\pi}{a}$ to the first CB, say, at $t = t_0$. The subsequent momentum displacement in the first CB is given by $A(t) - A(t_0)$, where $|A(t) - A(t_0)|$ is bounded by A_{peak}. Hence, if $A_{\mathrm{peak}} < \frac{\pi}{a}$, no excited electrons can reach the next MBG ($k = 0$), and they only oscillate in the first CB, which forms

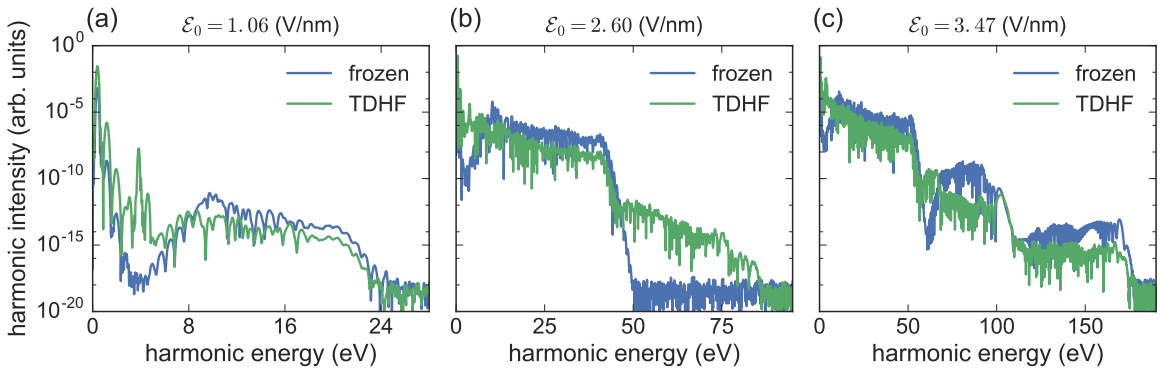

Figure 5.6: Harmonic spectra obtained from (blue) the frozen TDHF and (green) the TDHF simulations for (a) $\mathcal{E}_0 = 1.06$ V/nm, (b) $\mathcal{E}_0 = 2.60$ V/nm, and (c) $\mathcal{E}_0 = 3.47$ V/nm.

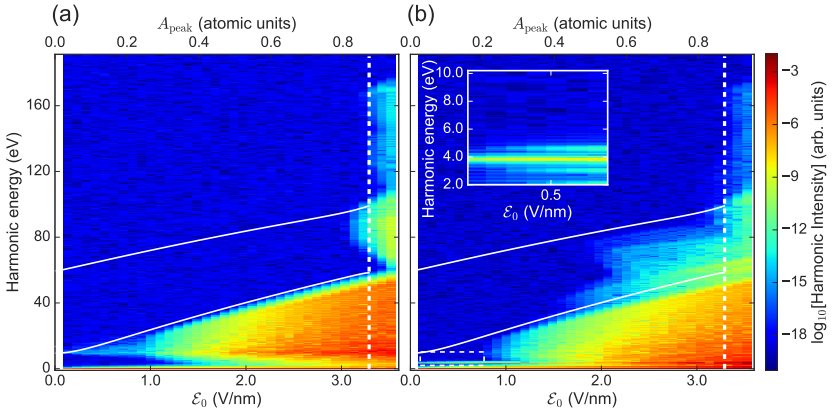

Figure 5.7: Harmonic spectra as functions of the field amplitude $\mathcal{E}_0$ (bottom axis) and corresponding A_{peak} (top axis) obtained from (a) frozen TDHF and (b) full TDHF simulations. The white dashed vertical lines denote $A_{\text{peak}} = \frac{\pi}{a} = 0.87$, which characterizes the position where the multiple plateaus appear according to the solid-state three-step model [67]. Two white solid lines are the energy differences between CBs and VB as function of A_{peak}, i.e., $\Delta\varepsilon_{10}(\frac{\pi}{a} - A_{\text{peak}})$ (lower) and $\Delta\varepsilon_{20}(A_{\text{peak}})$ (higher). Inset: a close-up of the low-field region represented by the dashed white line in (b).

a single plateau in the high-harmonic spectra. On the other hand, if $A_{\text{peak}} > \frac{\pi}{a}$, a part of electrons can reach the next MBG, be promoted to the second CB, and further climb up to higher and higher CBs by repeating the intraband displacement and interband tunneling, leading to the formation of multiple plateaus. The cutoff positions as well as time-frequency structure of HHG (see Fig. 5.11) can be deduced by tracing all the trajectories starting from different initial crystal momenta k_0. In Fig. 5.7(a) the second plateau appears slightly before $\frac{\pi}{a}$, because tunneling from the VB to CB takes place not only precisely at MBG but also in its vicinity.

Let us now turn on EHI and take a look at the full TDHF results shown in Fig. 5.7(b). At lower intensities up to about $=1.0$ V/nm, the exciton peak is dominantly seen [inset in Fig. 5.7(b)]. More remarkably, the second plateau already appears at $A_{\text{peak}} \sim 0.5$, much smaller than $\frac{\pi}{a}$. This is a striking manifestation of the EHI, which qualitatively alters HHG spectra.

One might suspect that the second-plateau appearance at much smaller field strength is caused by the enhanced exciton characteristics seen in 1D systems. In order to check that this qualitative change is not such a dimension specific effect, we also perform *weakened* TDHF simulation, using a weakened TDHF Hamiltonian

$$\hat{h}^{\alpha}_{\text{weak}}(t) = \hat{h}_f(t) + \alpha\hat{w}[\delta\rho(t)], \tag{5.27}$$

with $0 \leq \alpha \leq 1$. α is a parameter to control the strength of the electron-hole interaction[1]. Note that $\alpha = 0$ corresponds to the frozen TDHF Hamiltonian and $\alpha = 1$ to the full TDHF Hamiltonian.

Figure 5.8 shows the harmonic spectra as functions of the field amplitude $\mathcal{E}_0$ and corresponding A_{peak} obtained from the weakened TDHF simulations with $\alpha = 0.1$. While the exciton peak at lower field strength vanishes, the second plateau still appears at $A_{\text{peak}} \sim 0.5$. This result indicates that the early second-plateau appearance is not caused by peculiar excitonic influences in a 1D system, but is a universal nature of EHI in the TDHF Hamiltonian. We discuss its microscopic origin in the next section employing the Houston basis set.

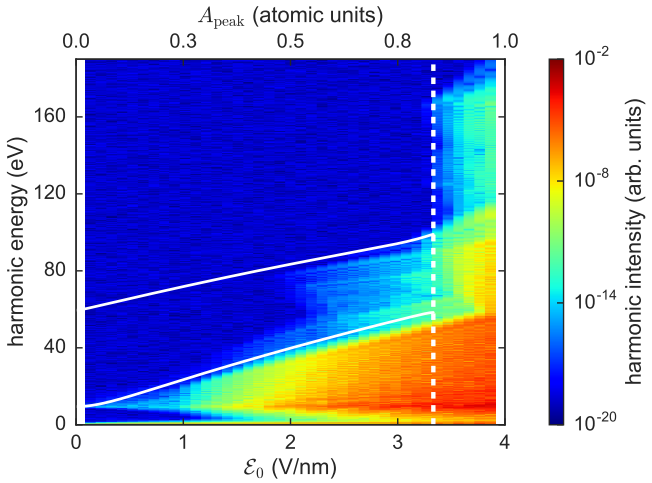

Figure 5.8: Same as Fig. 5.7(a) and (b), but from weakened TDHF simulations using $\hat{h}^{\alpha}_{\text{weak}}(t)$ with $\alpha = 0.1$.

5.3 Hauling-up effect

In order to reveal the underlying mechanism of the qualitative change in harmonic spectra, let us focus on the initial excitation process of a VB electron to the first CB by considering a two-band model

$$\psi_{b,k_0}(x,t) \approx \alpha^v_{k_0}(t) e^{-i\int_0^t \varepsilon_{v,k(t')}dt'} \tilde{\phi}_{v,k_0}(x,t) + \alpha^c_{k_0}(t) e^{-i\int_0^t \varepsilon_{c,k(t')}dt'} \tilde{\phi}_{c,k_0}(x,t), \tag{5.28}$$

where we expand the time-dependent electron orbital with Houston functions $\tilde{\phi}_{\lambda,k_0}(x,t)$ of the VB ($\lambda = v$) and the first CB ($\lambda = c$). A general discussion with multiple-band extension is given in Appendix F. It should be remembered that a Houston state $\tilde{\phi}_{\lambda,k_0}(x,t)$ is the instantaneous eigenstate of $\hat{h}_f(t)$ with eigenvalue $\varepsilon_{\lambda,k(t)}$,

$$\hat{h}_f(t)\tilde{\phi}_{\lambda,k_0}(x,t) = \varepsilon_{\lambda,k(t)}\tilde{\phi}_{\lambda,k}(x,t). \tag{5.29}$$

We assume that the excitation is small, that is, $\alpha^v_{k_0}(t) \approx 1$ and $\alpha^c_{k_0}(t) \ll 1$. Under this assumption, the EoM for CB complex amplitude is given by

$$i\frac{d}{dt}\alpha^c_{k_0}(t) \approx \alpha^v_{k_0}(t) e^{i\int_0^t \Delta\varepsilon_{cv}[k(t')]dt'} \left(\xi^{cv}_{k(t)}\mathcal{E}(t) + \langle\tilde{\phi}_{c,k_0}(t)|\,\hat{w}[\delta\rho(t)]\,|\tilde{\phi}_{v,k_0}(t)\rangle\right), \tag{5.30}$$

where $\xi^{\lambda\lambda'}_{k(t)} = i\,\langle u^0_{\lambda,k(t)}|\nabla_k u^0_{\lambda',k(t)}\rangle$, as given in Sec. 2.4. The matrix element of the interelectronic operator

[1]It should be remembered that the *full* TDHF Hamiltonian is given by $\hat{h}(t) = \hat{h}_f(t) + \hat{w}[\delta\rho(t)]$.

$\hat{w}[\delta\rho(t)]$ is composed of those of the Hartree and the exchange operator,

$$\begin{aligned}&\langle\tilde{\phi}_{c,k_0}(t)|\,\hat{w}[\delta\rho(t)]\,|\tilde{\phi}_{v,k_0}(t)\rangle\\&\quad=\langle\tilde{\phi}_{c,k_0}(t)|\,\hat{v}_{\mathrm{H}}[\delta\rho(t)]\,|\tilde{\phi}_{v,k_0}(t)\rangle+\langle\tilde{\phi}_{c,k_0}(t)|\,\hat{v}_{\mathrm{x}}[\delta\rho(t)]\,|\tilde{\phi}_{v,k_0}(t)\rangle\,.\end{aligned}\tag{5.31}$$

5.3.1 Coulomb and exchange matrix elements

It is useful to express the interelectronic Coulomb potential by spatial Fourier transform as,

$$v(x-x')=\sum_{G,q}v_{G+q}e^{i(G+q)(x-x')}.\tag{5.32}$$

Here $G=0,\pm\frac{2\pi}{a},\pm\frac{4\pi}{a}\ldots$ is the reciprocal lattice vector and $q\in[-\frac{\pi}{a},\frac{\pi}{a}]$ the crystal momentum within the BZ. For the soft Coulomb potential, v_k has an analytic form

$$v_k=\int dx\frac{e^{-ikx}}{\sqrt{x^2+1}}=2K_0(|k|),\tag{5.33}$$

where $K_n(k)$ is the n-th modified Bessel function of the second kind (Fig. 5.9).

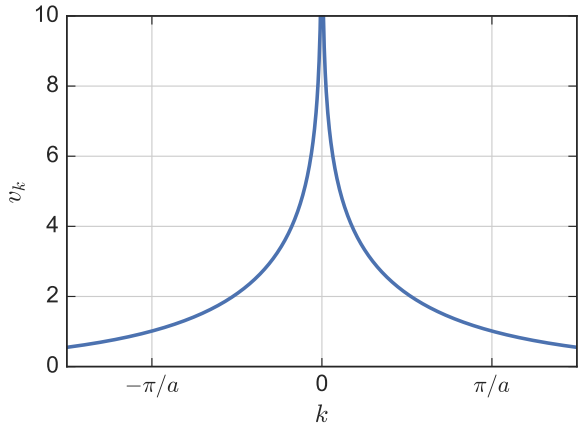

Figure 5.9: The Fourier transform of the soft Coulomb potential.

The Hartree term in Eq. (5.31) can be transformed as

$$\begin{aligned}&\langle\tilde{\phi}_{c,k_0}(t)|\,\hat{v}_{\mathrm{H}}[\delta\rho(t)]\,|\tilde{\phi}_{v,k_0}(t)\rangle\\&=\sum_{G\neq0}v_G\,\langle\tilde{\phi}_{c,k_0}(t)|\,e^{iGx}\,|\tilde{\phi}_{v,k_0}(t)\rangle\int dx'\delta\rho(x',x',t)e^{-iGx'},\end{aligned}\tag{5.34}$$

where we omit the term $G=0$ because $\int dx'\delta\rho(x',x',t)=0$. By substituting the Houston-basis expansion $\psi_{b,k_0}(x,t)=\sum_{\lambda=v,c}\alpha^{\lambda}_{k_0}(t)e^{-i\int_0^t\varepsilon_{\lambda,k(t')}dt'}\tilde{\phi}_{\lambda,k_0}(x,t)$ into the density matrix, we have

$$\begin{aligned}&\langle\tilde{\phi}_{c,k_0}(t)|\,\hat{v}_{\mathrm{H}}[\delta\rho(t)]\,|\tilde{\phi}_{v,k_0}(t)\rangle\\&=2\sum_{G\neq0}v_G\gamma^{c,v}_{k(t),k(t)}(G)\sum_{k'_0}\left(\sum_{\mu=v,c}\sum_{\nu=v,c}D^{\mu\nu}_{k'_0}(t)\gamma^{\nu,\mu}_{k'(t),k'(t)}(-G)-\gamma^{v,v}_{k'(t),k'(t)}(-G)\right),\end{aligned}\tag{5.35}$$

where we define

$$\gamma^{\lambda,\lambda'}_{k,k'}(G) = \langle u^0_{\lambda,k}|\, e^{iGx}\, |u^0_{\lambda',k'}\rangle = \int_\Omega dx u^{0*}_{\lambda,k}(x) e^{iGx} u^0_{\lambda',k'}(x), \tag{5.36}$$

and

$$D^{\lambda\lambda'}_{k_0}(t) = \alpha^{\lambda}_{k_0}(t)\alpha^{\lambda'*}_{k_0}(t) e^{-i\int_0^t \Delta\varepsilon_{\lambda\lambda'}[k(t')]dt'}. \tag{5.37}$$

$D^{\lambda\lambda'}_{k_0}(t)$ denotes the time-dependent interband polarization formed by an electron initially from k_0 between band λ and λ' at $k(t) = k_0 + A(t)$.

Similarly, the exchange term in Eq. (5.31) is transformed as

$$\begin{aligned}
&\langle \tilde{\phi}_{c,k_0}(t)|\, \hat{v}_{\mathrm{x}}[\delta\rho(t)]\, |\tilde{\phi}_{v,k_0}(t)\rangle \\
&= -\frac{1}{2}\sum_{G,q} v_{G+q} \iint dx dx' \tilde{\phi}^*_{c,k_0}(x,t)\delta\rho(x,x',t) e^{i(G+q)(x-x')} \tilde{\phi}_{v,k_0}(x',t) \\
&= -\sum_G \sum_{k'_0} v_{G+k_0-k'_0} \left(\sum_{\mu=v,c}\sum_{\nu=v,c} D^{\mu\nu}_{k'_0}(t)\gamma^{c,\mu}_{k(t),k'(t)}(G)\gamma^{\nu,v}_{k'(t),k(t)}(-G) - \gamma^{c,v}_{k(t),k'(t)}(G)\gamma^{v,v}_{k'(t),k(t)}(-G) \right).
\end{aligned} \tag{5.38}$$

5.3.2 Rotating wave approximation

The matrix elements of the Hartree (5.35) and the exchange (5.38) terms can be viewed as collections of oscillating polarization $D^{\lambda\lambda'}_{k'_0}(t)$ of other electrons at different crystal momentum that, once formed, may excite an electron at $k(t)$. Analogously to the rotating wave approximation [78], we take into account only the (most possibly) resonant terms that includes $D^{cv}_{k'_0}(t)$, which yields

$$\begin{aligned}
i\frac{d}{dt}\alpha^c_{k_0}(t) \approx \alpha^v_{k_0}(t) e^{i\int_0^t \Delta\varepsilon_{cv}[k(t')]dt'} \Bigg[&\xi^{cv}_{k(t)}\mathcal{E}(t) + 2\sum_{G\neq 0} v_G \gamma^{c,v}_{k(t),k(t)}(G) \sum_{k'_0} D^{cv}_{k'_0}(t)\gamma^{v,c}_{k'(t),k'(t)}(-G) \\
&- \sum_G \sum_{k'_0} v_{G+k_0-k'_0} D^{cv}_{k'_0}(t)\gamma^{c,c}_{k(t),k'(t)}(G)\gamma^{v,v}_{k'(t),k(t)}(-G) \Bigg].
\end{aligned} \tag{5.39}$$

The second term in Eq. (5.39) comes from the Hartree matrix elements (5.35) and the third from the exchange matrix elements (5.38), respectively.

5.3.3 Semiconductor-Bloch-equation-like treatment

From here, we follow the treatments of SBE [78, 95] to deduce a physical insight from Eq. (5.39). First, we ignore the Coulomb potential v_k outside the BZ, i.e., we assume $v_k = 0$ for $|k| > \frac{\pi}{a}$. Second, we assume that the lattice periodic part of Bloch functions is independent of k, i.e., $\phi_{\lambda,k}(x) = e^{ikx}u_{\lambda,k}(x) \approx e^{ikx}u_{\lambda,0}(x)$, which results in $\gamma^{\lambda\lambda'}_{k,k'}(0) = \langle u^0_{\lambda,k}|u^0_{\lambda',k'}\rangle \approx \delta_{\lambda\lambda'}$. Based on these assumptions, Eq. (5.39) can be simplified as

$$i\frac{d}{dt}\alpha^c_{k_0}(t) = \alpha^v_{k_0}(t) e^{i\int_0^t \Delta\varepsilon_{cv}[k(t')]dt'} \left[\mathcal{E}(t)\xi^{cv}_{k(t)} - \sum_{k'_0} v_{k_0-k'_0} D^{cv}_{k'_0}(t) \right]. \tag{5.40}$$

The first term in the right-hand side of Eq. (5.40) comes from the *frozen* TDHF Hamiltonian, and describes the independent-electron dynamics, depicted by the semiclassical trajectory analysis [67] pre-

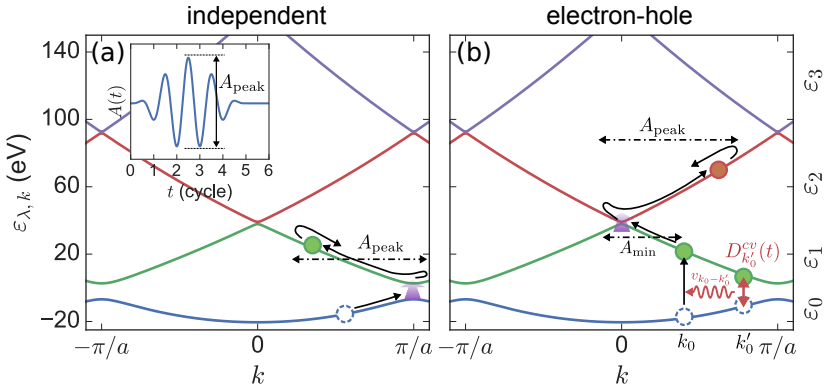

Figure 5.10: Pictorial representation of momentum-space electron dynamics (a) within the independent-electron approximation and (b) involving hauling-up excitation. The inset in (a) shows the waveform of the vector potential used in TDHF and *frozen* TDHF simulations and the definition of $A_{\rm peak}$. The single VB and first three CBs are shown for a 1D model hydrogen chain insulator (see text). The band index n is labeled as $0, 1, 2, \ldots$ from the bottom.

sented in Ch. 4. The second term, on the other hand, stems from EHI $\hat{w}[\delta\rho(t)]$ and indicates that interband or electron-hole polarization at a remote crystal momentum $k'(t) = k'_0 + A(t)$,

$$D^{cv}_{k'_0}(t) = \alpha^{c}_{k'_0}(t)\alpha^{v*}_{k'_0}(t)e^{-i\int_0^t \Delta\varepsilon_{cv}[k'(t')]dt'}, \tag{5.41}$$

can induce quasi-resonant excitation especially when $\Delta\varepsilon_{cv}[k(t)] \approx \Delta\varepsilon_{cv}[k'(t)]$. Therefore, even if a VB electron starting from k_0 dose not reach MBG through intraband displacement, it can be excited to the first CB once another electron initially at k'_0 reaches MBG and tunnels to the CB, connected via the Coulomb potential $v_{k_0-k'_0}$ [Fig. 5.10(b)]. It should be noticed that neither the first nor second terms directly change the crystal momentum, thus, the instantaneous crystal momentum is always given by $k(t) = k_0 + A(t)$, in whichever band the electron actually is.

5.3.4 Electron excitation from hauling-up effect

This *hauling-up* effect provides a shortcut for VB electrons to climb up to the second CB, which leads to the formation of the second plateau even if $A_{\rm peak} < \frac{\pi}{a}$. The electrons initially at $k_0 \in [-\max(A(t)), -\min(A(t))]$ pass by $k = 0$, i.e., MBG between the first and second CB. Thus, if these VB electrons are excited to the first CB via the hauling-up effect, then they can climb up to the second CB by tunneling at $k = 0$, eventually forming the second plateau via recombination with the VB hole. Note that they cannot reach MBG at $k = \pm\frac{\pi}{a}$ between the second and third CB. Therefore, the cutoff energy is expected to be given by $\varepsilon_{20}(A_{\rm peak})$. This prediction is in good agreement with the cutoff energy obtained from the TDHF simulation at $0.48 \lesssim A_{\rm peak} \leq \frac{\pi}{a} = 0.87$ [the upper white line in Fig. 5.7(b)].

Figure 5.11(a) and (b) show the time-frequency structure of HHG extracted by Gabor transformation from the TDHF and frozen TDHF simulations, respectively, for field amplitude $\mathcal{E}_0 = 2.60$ V/nm corresponding to $A_{\rm peak} = 0.69$. For the frozen TDHF case, we can well reproduce the spectrogram by drawing momentum-space semiclassical trajectories, assuming tunneling at MBG, intraband displacement, and photoemission on recombination with the VB hole [gray lines in Fig. 5.11(c)] [67]. The time-frequency structure from the full TDHF is significantly different, with photoemission above 60 eV, but can be reproduced if we additionally consider vertical excitation to the first CB from VB at arbitrary moments via the hauling-up [blue lines in Fig. 5.11(c)]. We see some discrepancy in the early stage of the pulse, which indeed supports our view that hauling-up becomes effective only after sufficient interband polarization

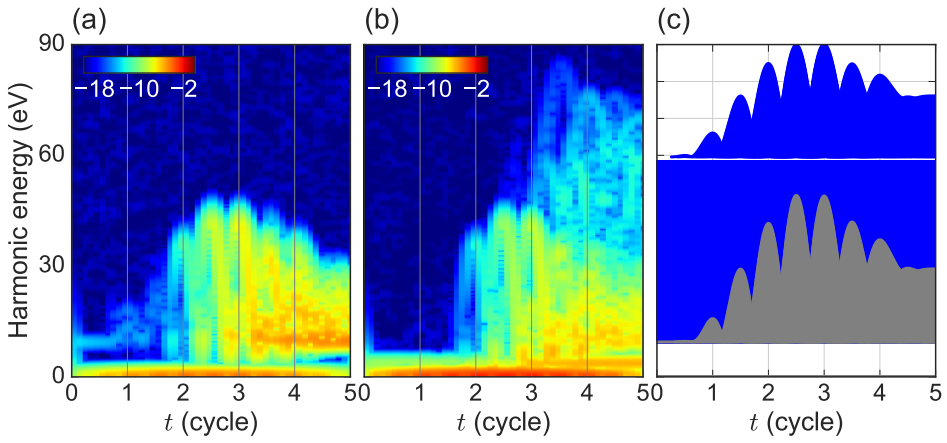

Figure 5.11: (a, b) Time frequency structure of HHG extracted by Gabor transform with a temporal window of its FWHM 1.8 fs, or 2.3 eV in energy, from (a) frozen TDHF and (b) full TDHF simulation results for $\mathcal{E}_0 = 2.60$ V/nm. (c) gray lines: electron trajectories that first tunnel from VB to the first CB band at the minimum band gap $k = \pm\frac{\pi}{a}$, drawn based on the solid-state three-step model [67]. Blue lines: trajectories involving promotion to the first CB via hauling-up excitation. The blank at ~ 60 eV, looking like a white line, reflects the energy gap between the first and second CB.

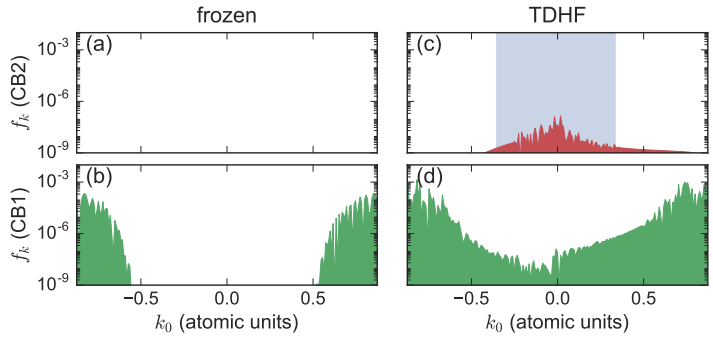

Figure 5.12: The final electron population f_k of the first (b, d) and second (a, c) CBs projected onto the ground state Bloch orbitals from (a, b) frozen TDHF and (c, d) full TDHF simulations for $\mathcal{E}_0 = 2.60$ V/nm. The shaded area in (c) represents the range $k_0 \in [-\max(A(t)), -\min(A(t))] = [-0.36, 0.33]$.

is formed at the MBG.

To further verify the hauling-up mechanism by EHI, we compare the final CB population f_k^λ obtained through projection onto the ground-state Bloch orbitals,

$$f_{k_0}^\lambda = 2|\langle\phi_{\lambda,k_0}|\psi_{b,k_0}(t = t_{\text{end}})\rangle|^2 \tag{5.42}$$

from the TDHF and frozen TDHF simulation results. Without EHI, only electrons starting from $k_0 \in [-\frac{\pi}{a}, -\frac{\pi}{a} - \min(A(t))] = [-0.87, -0.54]$ and $k_0 \in [\frac{\pi}{a} - \max(A(t)), \frac{\pi}{a}] = [0.51, 0.87]$ climb up to the first CB by tunneling at $k = \pm\frac{\pi}{a}$ [Fig. 5.12(a, b)]. Under the effect of EHI [Fig. 5.12(c, d)], on the other hand, electrons occupy a much broader range of k_0 in the first CB, and moreover, those initially at $k_0 \in [-\max(A(t)), -\min(A(t))] = [-0.36, 0.33]$ [the shaded area in Fig. 5.12(c)] are promoted to the second CB.

5.4 Conclusions

In summary, we have investigated the effects of electron-hole interaction on HHG from solid-state materials based on TDHF simulations for a 1D model system. We have found that, besides an exciton peak at low intensity, a second plateau appears at laser intensities much lower than expected from the independent electron approximation. Using the Houston-basis expansion and following the SBE-like treatments, we have identified it originating from the hauling-up effect due to EHI, where interband polarization, once created at and near an MBG, is capable of exciting electrons distant in the momentum space via the Coulomb potential. It allows those electrons that cannot reach the MBG by the intraband displacement to climb up from the VB to the first CB. This effect can be taken into account in the trajectory analysis to well reproduce the temporal structure of HHG extracted from the TDHF results. If we shift our eyes back to the gas-phase HHG, the influence of the Coulomb potential from the parent ion, neglected in the strong-field approximation [23], may somewhat correspond to that of EHI. However, it hardly affects qualitative features of harmonic spectra [96–98]. Our results suggest that solid-state HHG involves much more complicated mechanisms than its gas-phase counterpart, and, therefore, offers even richer information on ultrafast many-body correlation dynamics in solid materials.

6
Concluding Remarks

6.1 Overall summary

Studying the mechanism of HHG in solids is none other than the studying of the electron dynamics in solids under an intense electric field. Looking back at history, 50 years ago Keldysh discussed the cycle-averaged tunneling rate of electrons in solids under an intense laser field [99]. Today such strong-field excitation in solids is experimentally possible, and in particular, HHG from solid-state materials has offered exciting opportunities to look into the strong-field electron dynamics in solids. Understanding its nature will lead to not only future applications of solid-state HHG but also advances in future technologies such as petahertz optical current control and laser material processing. In this dissertation, we have theoretically approached this problem based on numerical simulation methods. Our goal is (i) to reveal the independent-electron dynamics in solids under an intense field underlying HHG, and (ii) to study the effects of electron-hole interactions in solids on HHG. Here, I summarize how we have achieved them.

(i) Independent-electron study on HHG in solids

As the study on HHG in solids is in its infancy, the underlying radiation mechanism is still under intensive discussions. Historically, HHG in solids was first discussed in terms of semiclassical carrier acceleration within a CB [13, 27, 32, 41, 53], often assuming a carrier creation at the Γ point and ignoring radiation due to electron-hole recombination. More recently, though, several authors have pointed out that the interband dynamics makes a dominant contribution to HHG above band gap energy. Based on this interband picture, Vampa *et al.* have proposed a real-space three-step model analogous to its gas-phase counterpart in the weak excitation limit [45]. Note that these previous models cannot treat the multiple-plateau appearance, which has been reported more recently.

Although these pioneering works have often considered a two-band model with a single VB and a single CB [13, 42, 45, 46], the importance of the effects of multiple bands has been recently pointed out by several authors [43, 53]. Wu *et al.* [43] have shown that the contributions from multiple bands can lead to the formation of multiple plateau structures, extending HHG to higher photon energies.

In Ch. 4, aiming at revealing essential electron dynamics, we have theoretically studied HHG from a 1D model crystal by numerically solving the time-dependent Schrödinger equation (TDSE) within the independent-electron approximation (IEA). By directly solving on a spatial grid, which enables us to include the contributions from all the bands, our simulations well reproduce unique features of solid-state HHG, such as the (quasi-)linear cutoff-energy scaling with the electric field strength [13, 27], and the sudden transition from single to multiple plateaus [29, 38] with clear cutoffs. Based on the simulation results, we have proposed a simple model that incorporates intraband displacement, interband tunneling, and recombination with the VB hole. A key parameter is the peak-to-valley amplitude A_{peak} of the pulse vector potential $A(t)$, which determines the crystal momentum displacement during a half cycle. When

the intraband acceleration allows electrons to reach the Brillouin zone (BZ) edge, repeated interband tunneling and intraband displacement can take place, which leads to a formation of multiple plateaus. Due to this stepwise process in the momentum space, it is predicted that the position of the highest cutoff can depend on not only the wavelength and field strength, but also pulse duration, which marks another difference from gas-phase HHG. Using our recipe, one can draw electron trajectories in the momentum space, from which one can deduce, for example, the time-frequency structure of HHG without elaborate quantum-mechanical calculations.

Our trajectory analysis can be viewed as a solid-state and momentum-space counterpart with a multi-band extension of the three-step model (TSM) in the gas-phase HHG. It provides a unified basis for understanding HHG in gas-phase and solid-state materials. This offers a clear physical insight into the coherent electron dynamics of independent-electron nature in solids driven by an intense electric field and serves as a benchmark to discuss the effects of electron correlation, relaxation, dephasing, impurity, distortion, etc., seen in real experiments.

(ii) Time-dependent Hartree-Fock study on HHG in solids

Can we treat the electrons in solids in a strong-field regime with the independent-electron picture, as often works well in gas-phase HHG? While most of the previous works [13, 27, 32–34, 37, 41, 42, 50, 55, 67, 68] have used the independent-electron approximation, the role of electron-hole interactions in solids in the strong-field regime is largely unexplored. Although the independent-electron picture has worked very well to describe the high-harmonic generation processes in atoms and molecules [21–23], its applicability in solids is questionable, as tunnel-excited electrons in solids moves through a sea of other spatially spread electrons. Garg *et al.* have recently suggested that electron-hole interaction affects harmonic yields from silicon dioxide using semiconductor-Bloch equations incorporating the interelectronic interaction [30]. This suggests that it is required to investigate the interplay between strong-field-driven individual electron dynamics and dynamical electron-hole interaction effects in ultrafast time-scale beyond the independent-electron picture.

In order to answer this question, in Ch. 5, we study the effects of electron-hole interaction (EHI) upon HHG in a 1D model crystal by numerically solving the time-dependent Hartree-Fock (TDHF) equations. Our study is a first application of TDHF methods to HHG in solid-state materials. We have found a qualitative change in harmonic spectra from what is obtained with the independent-electron simulations. In particular, a second plateau appears at much lower field strength than expected from the IEA trajectory analysis. Using the Houston basis expansion, we have revealed that the Coulomb interaction from an interband polarization created at the minimum band gap (MBG) mediates excitation of distant VB electrons, which we call *hauling-up effects*. In other words, this hauling-up process offers a shortcut route for VB electrons far from MBG to climb up to the first CB assisted by an electron-hole polarization formed at a different k-point. This mechanism is supported by the time-frequency structure of HHG and final band populations.

If we shift our eyes back to the gas-phase HHG, the influence of the Coulomb potential from the parent ion, neglected in the strong-field approximation [23], may somewhat correspond to that of EHI. However, it hardly affects qualitative features of harmonic spectra [96–98]. Our results suggest that the solid-state HHG mechanism involves much more complicated process than the gas-phase, and hence, may offer possible opportunities to reveal correlation in ultrafast electron dynamics in solids.

6.2 Outlook

(i) Polarization dependence of HHG in solids in terms of trajectory analysis

In Ch. 4, we have shown that, by drawing momentum-space electron trajectories across multiple bands, one can easily deduce many aspects of HHG in solids. The concept of this trajectory analysis can be extended to two- and three-dimensional momentum space of more realistic solid systems. In particular, it is of much interest to apply the momentum-space trajectory analysis to the HHG dependence on driving field polarization [35, 37] and ellipticity [36, 39]. You *et al.* have reported strong enhancement and suppression of harmonic yield from MgO crystal depending on field ellipticity [36]. They have argued that the enhancement is observed when classical electron real-space motion traverse across neighboring atomic sites in the crystal. It should be investigated in more detail in terms of the relationship between their real-space recollision picture and the momentum-space electron trajectories.

(ii) Trajectory analysis incorporating tunneling rate

In Ch. 4, we have discussed momentum-space electron motion incorporating intraband acceleration, interband tunneling excitation, and recollison with VB hole. In this present model, we assume that electrons can climb up to an upper band at any minimum gap point under any field strength. As seen here, this is a little oversimplified view. Let us consider a minimum gap point with *zero* gap energy — a free-electron limit. At this point, electrons seem to go up to the upper band freely, ... but, subsequently they must come back to the lower band as the oscillating field turns its sign, and none remain in the upper band. This would give a fundamental upper bound for the maximum energy that electrons can reach via the stepwise excitation. Oppositely, at a minimum gap point with a large gap energy, most electrons would undergo adiabatic intraband motion, with no excitation until a sufficiently high electric field is applied.

We can overcome these difficulties by incorporating the interband tunneling rate, expectedly depending on the band dispersion, dipole matrix element, and field strength. This is currently under intensive discussions in the field [11, 12, 41, 100–102].

(iii) Beyond Hartree-Fock: developing a multiconfiguration approach

Some authors have argued that dephasing of interband coherence plays an important role in HHG in solid-state materials [30, 42]. In particular, when interband dephasing is much faster than the relaxation of band population, the interband current is quickly suppressed and the intraband contribution remains as a dominant contribution. Currently, such effects have been theoretically taken into account as a phenomenological damping term, which has been assumed to be surprisingly short,on the order of ~ 1 fs [30, 42]. Such a short time scale, if possible, is considered to arise from scattering among densely excited carriers. In the field of laser material processing, such nonlinear electron dynamics are believed to cause an *avalanche process* [64], in which highly excited carriers cascadedly excite valence band electrons.

As we have discussed in Ch. 5 based on TDHF methods, a variety of probable effects in solids due to strong electron correlations make this field fascinating as well as complex. Describing electron scattering triggered by an intense electric field requires theoretical breakthrough beyond TDHF theory. This can be achieved by considering multiple Slater determinants. This *multiconfiguration* approach has been successful in describing many-electron correlated dynamics for gas-phase strong-field phenomena [51, 94, 103–105]. In gas-phase, in fact, several theoretical studies [94, 106] have recently pointed out that

many-body electron correlation can change HHG spectra qualitatively. Hence, the application of the multiconfiguration approach to solids will open a way to the first-principle description of many-body correlations in ultrafast electron dynamics in solids under intense field, and resulting phenomena, such as coherence dephasing, population relaxation, and avalanche excitation.

References

[1] E. Goulielmakis, M. Schultze, M. Hofstetter, V. S. Yakovlev, J. Gagnon, M. Uiberacker, A. L. Aquila, E. M. Gullikson, D. T. Attwood, R. Kienberger, F. Krausz, and U. Kleineberg, Science **320**, 1614 (2008).

[2] K. Zhao, Q. Zhang, M. Chini, Y. Wu, X. Wang, and Z. Chang, Opt. Lett. **37**, 3891 (2012).

[3] T. Gaumnitz, A. Jain, Y. Pertot, M. Huppert, I. Jordan, F. Ardana-Lamas, and H. J. Wörner, Opt. Express **25**, 27506 (2017).

[4] T. Popmintchev, M.-C. Chen, D. Popmintchev, P. Arpin, S. Brown, S. Ališauskas, G. Andriukaitis, T. Balčiunas, O. D. Mücke, A. Pugzlys, A. Baltuška, B. Shim, S. E. Schrauth, A. Gaeta, C. Hernández-García, L. Plaja, A. Becker, A. Jaron-Becker, M. M. Murnane, and H. C. Kapteyn, Science **336**, 1287 (2012).

[5] J. Itatani, J. Levesque, D. Zeidler, H. Niikura, H. Pépin, J. C. Kieffer, P. B. Corkum, and D. M. Villeneuve, Nature **432**, 867 (2004).

[6] M. F. Kling, C. Siedschlag, A. J. Verhoef, J. I. Khan, M. Schultze, T. Uphues, Y. Ni, M. Uiberacker, M. Drescher, F. Krausz, and M. J. J. Vrakking, Science **312**, 246 (2006).

[7] M. Uiberacker, T. Uphues, M. Schultze, A. J. Verhoef, V. Yakovlev, M. F. Kling, J. Rauschenberger, N. M. Kabachnik, H. Schroder, M. Lezius, K. L. Kompa, H.-G. Muller, M. J. J. Vrakking, S. Hendel, U. Kleineberg, U. Heinzmann, M. Drescher, and F. Krausz, Nature **446**, 627 (2007).

[8] A. L. Cavalieri, N. Muller, T. Uphues, V. S. Yakovlev, A. Baltuska, B. Horvath, B. Schmidt, L. Blumel, R. Holzwarth, S. Hendel, M. Drescher, U. Kleineberg, P. M. Echenique, R. Kienberger, F. Krausz, and U. Heinzmann, Nature **449**, 1029 (2007).

[9] O. Smirnova, Y. Mairesse, S. Patchkovskii, N. Dudovich, D. Villeneuve, P. Corkum, and M. Y. Ivanov, Nature **460**, 972 (2009).

[10] H. J. Wörner, J. B. Bertrand, D. V. Kartashov, P. B. Corkum, and D. M. Villeneuve, Nature **466**, 604 (2010).

[11] M. Schultze, E. M. Bothschafter, A. Sommer, S. Holzner, W. Schweinberger, M. Fiess, M. Hofstetter, R. Kienberger, V. Apalkov, V. S. Yakovlev, M. I. Stockman, and F. Krausz, Nature **493**, 75 (2013).

[12] M. Schultze, K. Ramasesha, C. Pemmaraju, S. Sato, D. Whitmore, A. Gandman, J. S. Prell, L. J. Borja, D. Prendergast, K. Yabana, D. M. Neumark, and S. R. Leone, Science **346**, 1348 (2014).

[13] S. Ghimire, A. D. DiChiara, E. Sistrunk, P. Agostini, L. F. DiMauro, and D. A. Reis, Nat. Phys. **7**, 138 (2011).

[14] P. Agostini, F. Fabre, G. Mainfray, G. Petite, and N. K. Rahman, Phys. Rev. Lett. **42**, 1127 (1979).

[15] T. J. McIlrath, P. H. Bucksbaum, R. R. Freeman, and M. Bashkansky, Phys. Rev. A **35**, 4611 (1987).

[16] P. Kruit, J. Kimman, H. G. Muller, and M. J. van der Wiel, Phys. Rev. A **28**, 248 (1983).

[17] C. J. Joachain, N. J. Kylstra, and R. M. Potvliege, *Atoms in Intense Laser Fields* (Cambridge University Press, 2011).

[18] M. Ammosov, N. B. Delone, and V. P. Krainov, Journal of Experimental and Theoretical Physics **64**, 1191 (1986).

[19] L. Landau and E. Lifshitz, *Quantum Mechanics*, Addison-Wesley series in advanced physics (Addison-Wesley, Reading, Mass., 1958).

[20] J. L. Krause, K. J. Schafer, and K. C. Kulander, Phys. Rev. Lett. **68**, 3535 (1992).

[21] P. B. Corkum, Phys. Rev. Lett. **71**, 1994 (1993).

[22] K. C. Kulander, K. J. Schafer, and J. L. Krause, "Dynamics of short-pulse excitation, ionization and harmonic conversion," in *Super-Intense Laser-Atom Physics* (Springer US, Boston, MA, 1993) pp. 95–110.

[23] M. Lewenstein, P. Balcou, M. Y. Ivanov, A. L'Huillier, and P. B. Corkum, Phys. Rev. A **49**, 2117 (1994).

[24] C.-G. Wahlström, J. Larsson, A. Persson, T. Starczewski, S. Svanberg, P. Salières, P. Balcou, and A. L'Huillier, Phys. Rev. A **48**, 4709 (1993).

[25] D. M. Volkov, Z. Phys. **94**, 250 (1935).

[26] D. M. Villeneuve, P. Hockett, M. J. J. Vrakking, and H. Niikura, Science **356**, 1150 (2017), http://science.sciencemag.org/content/356/6343/1150.full.pdf .

[27] T. T. Luu, M. Garg, S. Y. Kruchinin, a. Moulet, M. T. Hassan, and E. Goulielmakis, Nature **521**, 498 (2015).

[28] S. Han, H. Kim, Y. W. Kim, Y.-J. Kim, S. Kim, I.-Y. Park, and S.-W. Kim, Nat. Comm. **7**, 13105 (2016).

[29] G. Ndabashimiye, S. Ghimire, M. Wu, D. A. Browne, K. J. Schafer, M. B. Gaarde, and D. A. Reis, Nature **534**, 520 (2016).

[30] M. Garg, M. Zhan, T. T. Luu, H. Lakhotia, T. Klostermann, A. Guggenmos, and E. Goulielmakis, Nature **538**, 359 (2016).

[31] H. Kim, S. Han, Y. W. Kim, S. Kim, and S.-W. Kim, ACS Photonics **4**, 1627 (2017).

[32] O. Schubert, M. Hohenleutner, F. Langer, B. Urbanek, C. Lange, U. Huttner, D. Golde, T. Meier, M. Kira, S. W. Koch, and R. Huber, Nat. Photonics **8**, 119 (2014).

[33] G. Vampa, T. J. Hammond, N. Thiré, B. E. Schmidt, F. Légaré, C. R. McDonald, T. Brabec, and P. B. Corkum, Nature **522**, 462 (2015).

[34] M. Hohenleutner, F. Langer, O. Schubert, M. Knorr, U. Huttner, S. W. Koch, M. Kira, and R. Huber, Nature **523**, 572 (2015).

[35] H. Liu, Y. Li, Y. S. You, S. Ghimire, T. F. Heinz, and D. A. Reis, Nat. Phys. **13**, 262 (2017).

[36] Y. S. You, D. A. Reis, and S. Ghimire, Nat. Phys. **13**, 345 (2017).

[37] F. Langer, M. Hohenleutner, U. Huttner, S. Koch, M. Kira, and R. Huber, Nat. Photonics **11**, 227 (2017).

[38] Y. S. You, M. Wu, Y. Yin, A. Chew, X. Ren, S. Gholam-Mirzaei, D. A. Browne, M. Chini, Z. Chang, K. J. Schafer, M. B. Gaarde, and S. Ghimire, Opt. Lett. **42**, 1816 (2017).

[39] N. Yoshikawa, T. Tamaya, and K. Tanaka, Science **356**, 736 (2017).

[40] T. J. Hammond, S. Monchocé, C. Zhang, G. Vampa, D. Klug, A. Y. Naumov, D. M. Villeneuve, and P. B. Corkum, Nat Photon **11**, 594 (2017).

[41] P. G. Hawkins and M. Y. Ivanov, Phys. Rev. A **87**, 063842 (2013).

[42] G. Vampa, C. R. McDonald, G. Orlando, D. D. Klug, P. B. Corkum, and T. Brabec, Phys. Rev. Lett. **113**, 073901 (2014).

[43] M. Wu, S. Ghimire, D. A. Reis, K. J. Schafer, and M. B. Gaarde, Phys. Rev. A **91**, 043839 (2015).

[44] T. Otobe, Phys. Rev. B **94**, 235152 (2016).

[45] G. Vampa, C. R. McDonald, G. Orlando, P. B. Corkum, and T. Brabec, Phys. Rev. B **91**, 064302 (2015).

[46] T. Higuchi, M. I. Stockman, and P. Hommelhoff, Phys. Rev. Lett. **113**, 213901 (2014).

[47] J. Faist, F. Capasso, D. L. Sivco, C. Sirtori, A. L. Hutchinson, and A. Y. Cho, Science **264**, 553 (1994).

[48] B. S. Williams, Nat Photon **1**, 517 (2007).

[49] C. R. McDonald, G. Vampa, P. B. Corkum, and T. Brabec, Phys. Rev. A **92**, 033845 (2015).

[50] M. Wu, D. A. Browne, K. J. Schafer, and M. B. Gaarde, Phys. Rev. A **94**, 063403 (2016).

[51] K. L. Ishikawa and T. Sato, IEEE Journal of Selected Topics in Quantum Electronics **21**, 1 (2015).

[52] M. Korbman, S. Y. Kruchinin, and V. S. Yakovlev, New J. Phys. **15**, 013006 (2013).

[53] P. G. Hawkins, M. Y. Ivanov, and V. S. Yakovlev, Phys. Rev. A **91**, 013405 (2015).

[54] Z. Guan, X.-X. Zhou, and X.-B. Bian, Phys. Rev. A **93**, 033852 (2016).

[55] D. Golde, T. Meier, and S. W. Koch, Phys. Rev. B **77**, 075330 (2008).

[56] T. Otobe, J. Appl. Phys. **111**, 093112 (2012).

[57] N. Tancogne-Dejean, O. D. Mücke, F. X. Kärtner, and A. Rubio, Phys. Rev. Lett. **118**, 087403 (2017).

[58] W. V. Houston, Phys. Rev. **57**, 184 (1940).

[59] U. Huttner, M. Kira, and S. W. Koch, Laser & Photonics Reviews **11**, 1700049 (2017).

[60] G. Onida, L. Reining, and A. Rubio, Rev. Mod. Phys. **74**, 601 (2002).

[61] G. Vampa, T. J. Hammond, N. Thiré, B. E. Schmidt, F. Légaré, C. R. McDonald, T. Brabec, D. D. Klug, and P. B. Corkum, Phys. Rev. Lett. **115**, 193603 (2015).

[62] A. Schiffrin, T. Paasch-Colberg, N. Karpowicz, V. Apalkov, D. Gerster, S. Muhlbrandt, M. Korbman, J. Reichert, M. Schultze, S. Holzner, J. V. Barth, R. Kienberger, R. Ernstorfer, V. S. Yakovlev, M. I. Stockman, and F. Krausz, Nature **493**, 70 (2013).

[63] H. Mashiko, K. Oguri, T. Yamaguchi, A. Suda, and H. Gotoh, Nat Phys **12**, 741 (2016).

[64] P. Balling and J. Schou, Reports on Progress in Physics **76**, 036502 (2013).

[65] M. Lenzner, J. Krüger, S. Sartania, Z. Cheng, C. Spielmann, G. Mourou, W. Kautek, and F. Krausz, Phys. Rev. Lett. **80**, 4076 (1998).

[66] B. C. Stuart, M. D. Feit, S. Herman, A. M. Rubenchik, B. W. Shore, and M. D. Perry, Phys. Rev. B **53**, 1749 (1996).

[67] T. Ikemachi, Y. Shinohara, T. Sato, J. Yumoto, M. Kuwata-Gonokami, and K. L. Ishikawa, Phys. Rev. A **95**, 043416 (2017).

[68] T.-Y. Du and X.-B. Bian, Opt. Express **25**, 151 (2017).

[69] R. Leitsmann, W. G. Schmidt, P. H. Hahn, and F. Bechstedt, Phys. Rev. B **71**, 195209 (2005).

[70] C. Attaccalite, M. Grüning, and A. Marini, Phys. Rev. B **84**, 245110 (2011).

[71] J. B. Krieger and G. J. Iafrate, Phys. Rev. B **33**, 5494 (1986).

[72] A. D. Bandrauk, F. Fillion-Gourdeau, and E. Lorin, Journal of Physics B: Atomic, Molecular and Optical Physics **46**, 153001 (2013).

[73] K. Yabana, T. Sugiyama, Y. Shinohara, T. Otobe, and G. F. Bertsch, Phys. Rev. B **85**, 045134 (2012).

[74] J. Frenkel, *Wave Mechanics; Advanced General Theory* (Oxford, U.K.: Clarendon Press, 1934).

[75] P.-O. Löwdin and P. Mukherjee, Chemical Physics Letters **14**, 1 (1972).

[76] C. Kittel, *Quantum theory of solids*, 2nd ed. (Wiley, 1987) pp. 190–193.

[77] G. Grosso and G. P. Parravicini, *Solid State Physics*, 2nd ed. (Academic Press, Amsterdam, 2014).

[78] H. Haug and S. Koch, *Quantum Theory of the Optical and Electronic Properties of Semiconductors* (World Scientific, 2009).

[79] S. A. Sato and K. Yabana, Phys. Rev. B **89**, 224305 (2014).

[80] M. Frigo and S. G. Johnson, Proceedings of the IEEE **93**, 216 (2005), special issue on "Program Generation, Optimization, and Platform Adaptation".

[81] C. Kittel, *Introduction to Solid State Physics*, 8th ed. (Wiley, 2004) p. 197.

[82] N. Ashcroft and N. Mermin, *Solid state physics* (Brooks Cole, 1976) pp. 221–225.

[83] S. Ghimire, A. D. DiChiara, E. Sistrunk, G. Ndabashimiye, U. B. Szafruga, A. Mohammad, P. Agostini, L. F. DiMauro, and D. A. Reis, Phys. Rev. A **85**, 043836 (2012).

[84] K. L. Ishikawa, Phys. Rev. B **82**, 201402 (2010).

[85] K. L. Ishikawa, New J. Phys. **15**, 055021 (2013).

[86] P. Bowlan, E. Martinez-Moreno, K. Reimann, T. Elsaesser, and M. Woerner, Phys. Rev. B **89**, 041408 (2014).

[87] M. L. Klein and J. A. Venables, *Rare gas solids*, Vol. 1 (Academic Press, 1976).

[88] S. Baroni, G. Grosso, and G. P. Parravicini, Phys. Rev. B **29**, 2891 (1984).

[89] T. Ikemachi, Y. Shinohara, T. Sato, J. Yumoto, M. Kuwata-Gonokami, and K. L. Ishikawa, ArXiv e-prints (2017), arXiv:1709.08153 [physics.optics] .

[90] L. Bányai, I. Galbraith, C. Ell, and H. Haug, Phys. Rev. B **36**, 6099 (1987).

[91] T. Ogawa and T. Takagahara, Phys. Rev. B **43**, 14325 (1991).

[92] E. Lötstedt, T. Kato, and K. Yamanouchi, Phys. Rev. A **86**, 023401 (2012).

[93] R. Sawada, T. Sato, and K. L. Ishikawa, Phys. Rev. A **90**, 023404 (2014).

[94] I. Tikhomirov, T. Sato, and K. L. Ishikawa, Phys. Rev. Lett. **118**, 203202 (2017).

[95] M. Kira and S. Koch, *Semiconductor Quantum Optics* (Cambridge University Press, 2011).

[96] D. Shafir, B. Fabre, J. Higuet, H. Soifer, M. Dagan, D. Descamps, E. Mével, S. Petit, H. J. Wörner, B. Pons, N. Dudovich, and Y. Mairesse, Phys. Rev. Lett. **108**, 203001 (2012).

[97] A. Kamor, C. Chandre, T. Uzer, and F. Mauger, Phys. Rev. Lett. **112**, 133003 (2014).

[98] S. N. Pugliese, A. S. Simonsen, M. Førre, and J. P. Hansen, Phys. Rev. A **92**, 023424 (2015).

[99] L. Keldysh *et al.*, Sov. Phys. JETP **20**, 1307 (1965).

[100] P. A. Zhokhov and A. M. Zheltikov, Phys. Rev. Lett. **113**, 133903 (2014).

[101] G. Vampa and T. Brabec, Journal of Physics B: Atomic, Molecular and Optical Physics **50**, 083001 (2017).

[102] S. Y. Kruchinin, M. Korbman, and V. S. Yakovlev, Phys. Rev. B **87**, 115201 (2013).

[103] T. Sato and K. L. Ishikawa, Physical Review A **88**, 023402 (2013).

[104] T. Sato and K. L. Ishikawa, Physical Review A **91**, 023417 (2015).

[105] T. Sato, K. L. Ishikawa, I. Březinová, F. Lackner, S. Nagele, and J. Burgdörfer, Physical Review A **94**, 023405 (2016).

[106] A. N. Artemyev, L. S. Cederbaum, and P. V. Demekhin, Phys. Rev. A **95**, 033402 (2017).

[107] G. F. Gribakin and M. Y. Kuchiev, Phys. Rev. A **55**, 3760 (1997).

[108] M. Wegener, *Extreme Nonlinear Optics: An Introduction*, Advanced Texts in Physics (Springer Berlin Heidelberg, 2006)

A

Atomic Units

Atomic units (a.u.) are a system of natural units, where we have $m_e = e = \hbar = a_0 = 1$ with m_e, e, $\hbar$, and a_0 are electron mass, elementary charge, reduced Planck's constant, and hydrogen Bohr radius [17]. In atomic units, the speed of light $c = 137.036$ a.u. Typical units are given in Table A.I.

Table A.1: Atomic units

Quantity	**Unit**	**Physical significance**	**Value in SI units**
mass	m	electron mass	9.10938×10^{-31} kg
charge	e	absolute value of electron charge	1.60218×10^{-19} C
angular momentum	$\hbar$	reduced Planck's constant	1.05457×10^{-34} Js
length	a_0	Bohr radius of hydrogen atom	5.29177×10^{-11} m
energy	$\frac{e^2}{4\pi\epsilon_0 a_0}$	twice the binding energy of hydrogen atom	4.35974×10^{-18} J $= 27.2114$ eV
velocity	v_0	magnitude of electron velocity in hydrogen atom	2.18769×10^{6} ms^{-1}
time	$\frac{a_0}{v_0}$	time required for electron in hydrogen atom to travel one Bohr radius	2.41888×10^{-17} s
electric field	$\mathcal{E}_a = \frac{e}{4\pi\epsilon_0 a_0^2}$	electric field strength in hydrogen atom	5.14221×10^{11} Vm^{-1}
field intensity	$\frac{1}{2}\epsilon_0 c {\mathcal{E}_a}^2$	field intensity of electric field in hydrogen atom	3.50945×10^{16} W/cm^2

B

Saddle-Point Analysis for Tunneling Excitation of Solid Electrons

Here, I derive the formula for the excitation amplitude of VB electron initially located in VB b at crystal momentum k_0 to the CB c. Starting from the initial VB state at crystal momentum k_0, we consider a dynamics in which the electron passes by the MBG between the VB and the first CB at $k = 0$. We expand the time-dependent electron orbital $\psi_{b,k_0}(x,t)$ with the Hostoun functions $p\tilde{h}i_{\lambda,k_0}(x,t) = e^{-iA(t)x}\phi_{\lambda,k(t)}$,

$$\psi_{b,k_0}(x,t) = \sum_{\mu} a^{\mu}_{b,k_0}(t) e^{-i\int_0^t \varepsilon_{\mu,k(t')}dt'} \tilde{\phi}_{\mu,k_0}(x,t), \tag{B.1}$$

with $k(t) = k_0 + A(t)$. The initial probability amplitude is given by

$$a^{\lambda}_{b,k_0}(t=0) = \begin{cases} 1 & (\lambda = b) \\ 0 & (\lambda \neq b). \end{cases} \tag{B.2}$$

Assuming that the excitation to the upper CBs is small and the most dominant dynamics is the excitation to the first CB, we approximate the orbital as

$$\psi_{b,k_0}(x,t) \approx e^{-i\int_0^t \varepsilon_{b,k(t')}dt'} \tilde{\phi}_{b,k_0}(x,t) + a^{c}_{b,k_0}(t) e^{-i\int_0^t \varepsilon_{c,k(t')}dt'} \tilde{\phi}_{c,k_0}(x,t), \tag{B.3}$$

with $|a^{c}_{b,k_0}(t)| \ll 1$. The dynamics of $a^{c}_{b,k_0}(t)$ is governed by the equation of motion,

$$i\frac{\partial}{\partial t} a^{c}_{b,k_0}(t) = E(t)\xi_{cb}(k(t)) e^{i\int_0^t \Delta\varepsilon_{cb}(k(t'))dt'}, \tag{B.4}$$

or,

$$a^{c}_{b,k_0}(t) = \frac{1}{i}\int_0^t dt' E(t')\xi_{cb}(k(t')) e^{iS^{cb}_{k_0}(t')}, \tag{B.5}$$

where we define the classical action

$$S^{\lambda\lambda'}_{k_0}(t) = \int_0^t dt' \Delta\varepsilon_{\lambda\lambda'}(k(t')). \tag{B.6}$$

We note that $\xi_{cb}(k(t))$ is given by

$$\xi_{cb}(k(t)) = \frac{ip^{cb}_k}{\Delta\varepsilon_{cb}(k)} = \frac{ip^{cb}_k}{\frac{\partial}{\partial t} S^{cb}_{k_0}(t)}. \tag{B.7}$$

We evaluate the right-hand side of Eq. (B.5) based on the saddle-point approximation. According to

the saddle-point method, the major contribution comes from the saddle point $t' = t_s$ that satisfies

$$\frac{\partial}{\partial t'} S_{k_0}^{cb}(t')\big|_{t'=t_s} = 0 \Leftrightarrow \Delta\varepsilon_{cb}(k(t_s)) = 0. \tag{B.8}$$

We approximate $\Delta\varepsilon_{cb}(k)$ as a parabolic band around $k = 0$,

$$\Delta\varepsilon_{cb}(k) = \varepsilon_g + \frac{k^2}{2m_r}, \tag{B.9}$$

where m_r denotes the reduced mass, which can be approximated as [77]

$$m_r^{-1} = \frac{4(p_0^{cb})^2}{\varepsilon_g}. \tag{B.10}$$

Similarly to the Lewenstein model in gas-phase HHG [23], the saddle-point condition Eq. (B.8) cannot be satisfied with real value and we have to introduce a complex time. In classical approximation, where we set $\varepsilon_g = 0$, Eq. (B.8) can be solved as

$$k(t_d) = 0 \Leftrightarrow k_0 + A(t_d) = 0. \tag{B.11}$$

Let us assume that $t_s = t_d + \tau$. The imaginary part of t_s is usually interpreted as a tunneling time. Assuming that the field is sufficiently strong and the tunneling time is small, let us expand the left-hand side of Eq. (B.8) with τ,

$$\frac{\partial}{\partial t'} S_{k_0}^{cb}(t')\big|_{t'=t_s} = s_0 + s_1\tau + s_2\tau^2. \tag{B.12}$$

Taking into consideration that

$$\begin{aligned} k_0 + A(t_s) &= k_0 + A(t_d + \tau) \\ &= k_0 + A(t_d) + \left.\frac{\partial A(t)}{\partial t}\right|_{t=t_d} \tau \\ &= -E(t_d)\tau, \end{aligned} \tag{B.13}$$

and by comparing with Eq. (B.8,)we obtain

$$s_0 = \varepsilon_g \tag{B.14}$$

$$s_1 = 0 \tag{B.15}$$

$$s_2 = \frac{E(t_d)^2}{2m_r}. \tag{B.16}$$

Therefore, the saddle-point condition is satisfied with

$$\tau = \pm i\frac{\sqrt{2m_r\varepsilon_g}}{|E(t_d)|}, \tag{B.17}$$

or,

$$\tau = \pm i\frac{\sqrt{2}\varepsilon_g}{2|p_0^{cb}E(t_d)|}. \tag{B.18}$$

Although we have two solutions with positive and negative sign, we choose the positive one based on physical insight (the negative one corresponds to the divergent solution).

From Eq. (B.12),

$$\begin{aligned} S^{cb}_{k_0}(t_s) &= S^{cb}_{k_0}(t_d) + s_0\tau + \frac{1}{3}s_2\tau^3 \\ &= S^{cb}_{k_0}(t_d) + i\frac{\sqrt{2}}{3}\frac{\varepsilon_g^2}{|p_0^{cb}E(t_d)|} \qquad \text{(B.19)} \\ &= S^{cb}_{k_0}(t_d) + i\frac{\sqrt{2}}{3}\frac{\varepsilon_g}{|\xi_0^{cb}E(t_d)|}. \qquad \text{(B.20)} \end{aligned}$$

We also evaluate the second temporal derivative of the classical action $S^{cb}_{k_0}(t)$,

$$\begin{aligned} \frac{\partial^2}{\partial t'^2}\, S^{cb}_{k_0}(t')\big|_{t'=t_s} &= \frac{k(t_s)}{m_r}\dot{k}(t_s) \\ &= \frac{E(t_d)\tau}{m_r}E(t_s) \\ &\approx i2\sqrt{2}|p_0^{cb}E(t_d)|. \qquad \text{(B.21)} \end{aligned}$$

Thus, we obtain

$$S^{cb}_{k_0}(t') = S^{cb}_{k_0}(t_s) + i\sqrt{2}|p_0^{cb}E(t_d)|(t'-t_s)^2, \qquad \text{(B.22)}$$

$$\frac{\partial}{\partial t'}S^{cb}_{k_0}(t') = i2\sqrt{2}|p_0^{cb}E(t_d)|(t'-t_s), \qquad \text{(B.23)}$$

in the vicinity of $t' = t_s$.

Therefore, Eq. (B.5) can be evaluated as,

$$\begin{aligned} a^c_{b,k_0}(t) &= \frac{1}{i}\int_0^t dt' E(t')\xi_{cb}(k(t'))e^{iS^{cb}_{k_0}(t')} \\ &= \int_0^t dt' \frac{E(t')p^{cb}_{k(t')}}{\frac{\partial}{\partial t'}S^{cb}_{k_0}(t')}e^{iS^{cb}_{k_0}(t')} \\ &\approx \int_0^t dt' \frac{E(t_s)p^{cb}_{k(t_s)}}{i2\sqrt{2}|p_0^{cb}E(t_d)|(t'-t_s)}e^{i(S^{cb}_{k_0}(t_s)+i\sqrt{2}|p_0^{cb}E(t_d)|(t'-t_s)^2)} \\ &= e^{iS^{cb}_{k_0}(t_d)}e^{-\frac{\sqrt{2}\varepsilon_g}{3|\xi_0^{cb}E(t_d)|}}\frac{E(t_s)p^{cb}_{k(t_s)}}{i2\sqrt{2}|p_0^{cb}E(t_d)|}\int_0^t dt'\frac{e^{-\sqrt{2}|p_0^{cb}E(t_d)|(t'-t_s)^2}}{t'-t_s}. \qquad \text{(B.24)} \end{aligned}$$

Using a formula [17, 107],

$$\int dt \frac{e^{-\lambda f(t)}}{(t-t_s)^\nu} \xrightarrow[\lambda\to\infty]{} i^\nu \pi^{1/2}\frac{\Gamma(\nu/2)}{\Gamma(\nu)}\left[2\lambda f''(t_s)\right]^{(\nu+1)/2}, \qquad \text{(B.25)}$$

the integral in Eq. (B.24) can be evaluated as,

$$\int_0^t dt' \frac{e^{-\sqrt{2}|p_0^{cb}E(t_d)|(t'-t_s)^2}}{t'-t_s} = i\pi 4\sqrt{2}|p_0^{cb}E(t_d)|. \qquad \text{(B.26)}$$

Finally, we obtain

$$a^c_{b,k_0}(t) = 2\pi e^{iS^{cb}_{k_0}(t_d)} e^{-\frac{\sqrt{2}\varepsilon_g}{3|\xi^{cb}_0 E(t_d)|}} E(t_s) p^{cb}_{k(t_s)} \tag{B.27}$$

$$\approx 2\pi e^{iS^{cb}_{k_0}(t_d)} e^{-\frac{\sqrt{2}\varepsilon_g}{3|\xi^{cb}_0 E(t_d)|}} E(t_d) p^{cb}_{k(t_d)}. \tag{B.28}$$

C

Linear Response and Exciton in TDHF Theory

Field-induced current $\boldsymbol{j}(t)$ can be expanded in terms of applied electric field $\boldsymbol{E}(t)$ as, symbolically [108],

$$\boldsymbol{j}(t) = \sigma^{(1)}\boldsymbol{E}(t) + \sigma^{(2)}\boldsymbol{E}(t)^2 + \sigma^{(3)}\boldsymbol{E}(t)^3 + \cdots, \tag{C.1}$$

where $\sigma^{(n)}$ represents the n-th order optical conductivity. For sufficiently small field, the field-induced current can be expressed only within the linear term,

$$j_\alpha(t) = \sum_\beta \int_{-\infty}^{t} \sigma_{\alpha\beta}(t-t')E_\beta(t')dt', \tag{C.2}$$

where α, β denote the Cartesian indices. By taking a temporal Fourier transform, we obtain an equivalent expression

$$j_\alpha(\omega) = \sigma_{\alpha\beta}(\omega)E_\beta(\omega). \tag{C.3}$$

The linear response is characterized by the linear optical conductivity

$$\sigma_{\alpha\beta}(\omega) = \frac{j_\alpha(\omega)}{E_\beta(\omega)} = \frac{\int dt e^{i\omega t} j_\alpha(t)}{\int dt e^{i\omega t} E_\beta(t)}. \tag{C.4}$$

The linear optical conductivity is related to the dielectric function $\epsilon(\omega) = 1 + \frac{4\pi i}{\omega}\sigma(\omega)$, and thus its real part corresponds to absorption. Eq. (C.4) enables us to obtain the linear response of the system from real-time simulation with applying sufficiently weak electric field $\boldsymbol{E}(t)$. One of the convenient choices of $\boldsymbol{E}(t)$ is the impulsive field $\boldsymbol{E}(t) = \boldsymbol{E}_0\delta(t)$, which corresponds to the vector potential whose waveform is a step function $\boldsymbol{A}(t) = -\int^t dt' \boldsymbol{E}(t') = -\boldsymbol{E}_0\Theta(t)$.

We show the real part of the linear conductivity obtained from TDHF and frozen TDHF simulation for the model hydrogen chain presented in Ch. 5 in Fig. C.1. We see a sharp exciton peak at 3.8 eV well below the gap energy 9.5 eV.

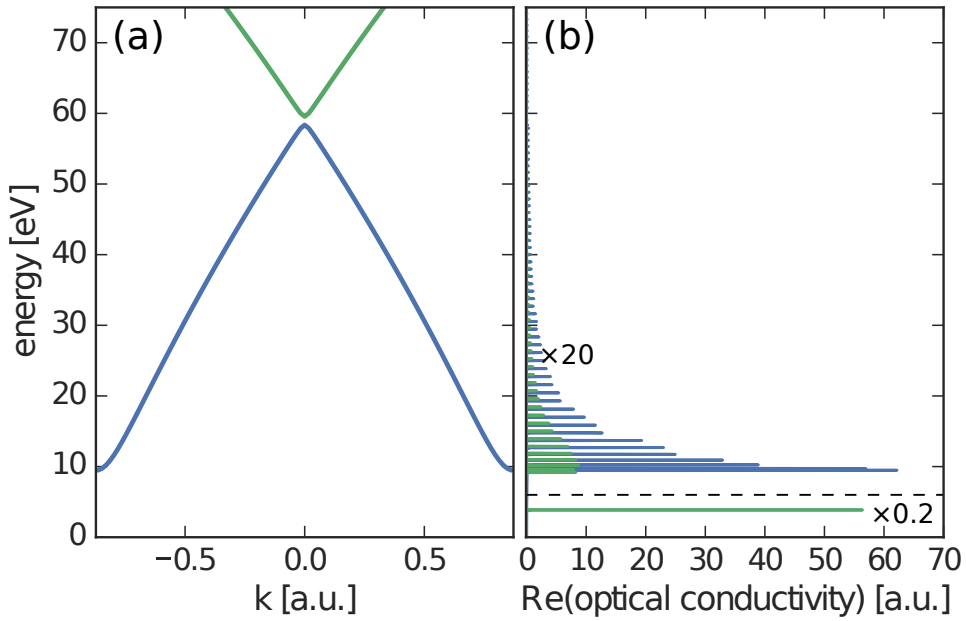

Figure C.1: The band structure of the model hydrogen chain and its linear response. (a) The conduction band energy difference from the valence band $\Delta\varepsilon_{mn}(k) = \varepsilon_{m,k} - \varepsilon_{n,k}$ ($m = 1, 2$ and $n = 0$). (b) The real part of the linear optical conductivity obtained from the real-time (green) TDHF and (blue) frozen TDHF simulations. As the TDHF conductivity has a strong exciton peak at 3.8 eV, its below-gap component (≤ 6 eV) is scaled by a factor of 0.2 while its above-gap component is magnified by a factor of 20.

D

Equivalence of TDHF Theory and Semiconductor Bloch Equation

Here I present the equivalence of the time-dependent Hartree-Fock (TDHF) theory and the semiconductor Bloch equation (SBE) by deriving SBE from TDHF theory. The TDHF Hamiltonian is given by

$$\hat{h}(t) = \hat{h}_0 + \hat{w}[\delta\rho] + \hat{v}_{\mathrm{l-m}}, \tag{D.1}$$

where

$$\hat{h}_0 = \frac{\hat{\boldsymbol{p}}^2}{2} + v_1(\boldsymbol{x}) + \hat{w}[\rho_0] \tag{D.2}$$

denotes the field-free HF Hamiltonian, $\hat{w}[\delta\rho]$ the dynamical contribution from the interelectronic Coulomb interactions, and $\hat{v}_{\mathrm{l-m}}$ the light-matter interaction Hamiltonian, i.e.,

$$\hat{v}_{\mathrm{l-m}} = \boldsymbol{x} \cdot \boldsymbol{E}(t), \tag{D.3}$$

in the length gauge, and

$$\hat{v}_{\mathrm{l-m}} = \hat{\boldsymbol{p}} \cdot \boldsymbol{A}(t) + \frac{1}{2}\boldsymbol{A}(t)^2, \tag{D.4}$$

in the velocity gauge. Here $\hat{w}[\rho]$ is composed of the Hartree term $\hat{v}_{\mathrm{H}}$ and the exchange term $\hat{v}_{\mathrm{F}}$,

$$w[\rho](\boldsymbol{x}, \boldsymbol{x}') = v_{\mathrm{H}}[\rho](\boldsymbol{x}, \boldsymbol{x}') + v_{\mathrm{F}}[\rho](\boldsymbol{x}, \boldsymbol{x}') \tag{D.5}$$

$$\begin{aligned} v_{\mathrm{H}}[\rho](\boldsymbol{x}, \boldsymbol{x}') &= \int d\boldsymbol{x}''\rho(\boldsymbol{x}'', \boldsymbol{x}'')v(\boldsymbol{x} - \boldsymbol{x}'')\delta(\boldsymbol{x} - \boldsymbol{x}') \\ &= \sum_{\boldsymbol{G},\boldsymbol{q}} v_{\boldsymbol{G}+\boldsymbol{q}} \int d\boldsymbol{x}''\rho(\boldsymbol{x}'', \boldsymbol{x}'')e^{i(\boldsymbol{G}+\boldsymbol{q})\cdot(\boldsymbol{x}-\boldsymbol{x}'')}\delta(\boldsymbol{x} - \boldsymbol{x}') \\ &= \sum_{\boldsymbol{G}} v_{\boldsymbol{G}} e^{i\boldsymbol{G}\cdot\boldsymbol{x}}\delta(\boldsymbol{x} - \boldsymbol{x}')\,\mathrm{Tr}[\rho e^{-i\boldsymbol{G}\cdot\boldsymbol{x}}] \end{aligned} \tag{D.6}$$

$$\begin{aligned} v_{\mathrm{F}}[\rho](\boldsymbol{x}, \boldsymbol{x}') &= -\frac{1}{2}\rho(\boldsymbol{x}, \boldsymbol{x}')v(\boldsymbol{x} - \boldsymbol{x}') \\ &= -\frac{1}{2}\sum_{\boldsymbol{G},\boldsymbol{q}} v_{\boldsymbol{G}+\boldsymbol{q}}\rho(\boldsymbol{x}, \boldsymbol{x}')e^{i(\boldsymbol{G}+\boldsymbol{q})\cdot(\boldsymbol{x}-\boldsymbol{x}')}, \end{aligned} \tag{D.7}$$

with $v_{\boldsymbol{k}}$ denoting the spatial Fourier transform of the Coulomb potential $v(\boldsymbol{x})$. The single electron density matrix is given by

$$\rho(t) = 2\sum_{b,\boldsymbol{k}} \psi_{b,\boldsymbol{k}}\psi^{\dagger}_{b,\boldsymbol{k}}, \tag{D.8}$$

where $\psi_{b,\boldsymbol{k}}(t)$ is the time-dependent orbital whose initial state is the Bloch state $\phi_{b,\boldsymbol{k}}$ with the eigenenergy $\varepsilon_{b,\boldsymbol{k}}$, i.e., $\hat{h}_0\phi_{b,\boldsymbol{k}} = \varepsilon_{b,\boldsymbol{k}}\phi_{b,\boldsymbol{k}}$.

Let us define the dynamical contribution of the density matrix as

$$\delta\rho(t) = \rho(t) - \rho_0, \tag{D.9}$$

where the initial density matrix ρ_0 is defined as

$$\rho_0 = 2\sum_{b,\boldsymbol{k}} \phi_{b,\boldsymbol{k}}\phi^\dagger_{b,\boldsymbol{k}} \tag{D.10}$$

in the length gauge, and

$$\rho_0 = 2\sum_{b,\boldsymbol{k}} e^{-i\boldsymbol{A}(t)\cdot\boldsymbol{x}}\phi_{b,\boldsymbol{k}}\phi^\dagger_{b,\boldsymbol{k}}e^{i\boldsymbol{A}(t)\cdot\boldsymbol{x}} \tag{D.11}$$

in the velocity gauge. The factors $e^{-i\boldsymbol{A}(t)\cdot\boldsymbol{x}}$ and $e^{i\boldsymbol{A}(t)\cdot\boldsymbol{x}}$ arises from the gauge transformation.

The relevant physical quantities here are the polarization

$$2p^{\lambda\lambda'}_{\boldsymbol{k}} = \rho^{\lambda\lambda'}_{\boldsymbol{k}} = \delta\rho^{\lambda\lambda'}_{\boldsymbol{k}} \quad (\lambda \neq \lambda') \tag{D.12}$$

and the population

$$2f^{\lambda}_{\boldsymbol{k}} = \rho^{\lambda\lambda}_{\boldsymbol{k}} = n^{\lambda}_{k} + \delta\rho^{\lambda\lambda}_{\boldsymbol{k}} = \begin{cases} 2 + \delta\rho^{\lambda\lambda}_{\boldsymbol{k}} & (\lambda \in \text{VB}) = 2 - 2f^{h_\lambda}_{\boldsymbol{k}} \\ \delta\rho^{\lambda\lambda}_{\boldsymbol{k}} & (\lambda \in \text{CB}) = 2f^{e_\lambda}_{\boldsymbol{k}}, \end{cases} \tag{D.13}$$

where $n^{\lambda}_{\boldsymbol{k}}$ denotes the initial occupation number of the band λ at the crystal momentum $\boldsymbol{k}$, namely, $n^{\lambda}_{\boldsymbol{k}} = 2$ if $\lambda \in$ VB and $n^{\lambda}_{\boldsymbol{k}} = 0$ of $\lambda \in$ CB. I note that the matrix element of the initial density matrix can be written as

$$\rho^{\lambda\lambda'}_{0,\boldsymbol{k}} = n^{\lambda}_{\boldsymbol{k}}\delta_{\lambda\lambda'}. \tag{D.14}$$

$f^{h_\lambda}_{\boldsymbol{k}}$ and $f^{e_{\lambda'}}_{\boldsymbol{k}}$ represents the population of hole in VB λ and of electron in CB λ', respectively. Here, we write the matrix element of a general operator $\hat{O}$ as

$$O^{\lambda\lambda'}_{\boldsymbol{k}} = \langle\phi_{\lambda,\boldsymbol{k}}|\,\hat{O}\,|\phi_{\lambda',\boldsymbol{k}}\rangle\,. \tag{D.15}$$

The dynamics of the density matrix is described by

$$i\frac{\partial}{\partial t}\hat{\rho} = [\hat{h}, \hat{\rho}]. \tag{D.16}$$

Equation (D.16) yields the coupled differential equations for $p^{\lambda\lambda'}_{\boldsymbol{k}}$ and $f^{\lambda}_{\boldsymbol{k}}$,

$$\begin{aligned} i\frac{\partial}{\partial t}\rho^{\lambda\lambda'}_{\boldsymbol{k}} &= \langle\phi_{\lambda,\boldsymbol{k}}|\,\rho\,|\phi_{\lambda',\boldsymbol{k}}\rangle \\ &= \sum_{\mu}(h^{\lambda\mu}_{\boldsymbol{k}}\rho^{\mu\lambda'}_{\boldsymbol{k}} - \rho^{\lambda\mu}_{\boldsymbol{k}}h^{\mu\lambda'}_{\boldsymbol{k}}) \\ &= \sum_{\mu}(h^{\lambda\mu}_{\boldsymbol{k}}\rho^{\mu\lambda'}_{0,\boldsymbol{k}} - \rho^{\lambda\mu}_{0,\boldsymbol{k}}h^{\mu\lambda'}_{\boldsymbol{k}}) + \sum_{\mu}(h^{\lambda\mu}_{\boldsymbol{k}}\delta\rho^{\mu\lambda'}_{\boldsymbol{k}} - \delta\rho^{\lambda\mu}_{\boldsymbol{k}}h^{\mu\lambda'}_{\boldsymbol{k}}). \end{aligned} \tag{D.17}$$

By solving Eq. (D.17), we obtain the equation of motion for $p^{\lambda\lambda'}_{\boldsymbol{k}}$ if we choose $\lambda \neq \lambda'$, and for $f^{\lambda}_{\boldsymbol{k}}$ if we choose $\lambda = \lambda'$.

The matrix element of the TDHF Hamiltonian is given by

$$h_{\boldsymbol{k}}^{\lambda\lambda'} = \varepsilon_{\lambda,\boldsymbol{k}}\delta_{\lambda\lambda'} + (v_{\mathrm{l-m}})_{\boldsymbol{k}}^{\lambda\lambda'} + w[\delta\rho]_{\boldsymbol{k}}^{\lambda\lambda'}. \tag{D.18}$$

The matrix elements of the Hartree term $\hat{v}_{\mathrm{H}}$ and the exchange term $\hat{v}_{\mathrm{F}}$ are obtained as below:

$$\begin{aligned} v_{\mathrm{H}}[\delta\rho]_{\boldsymbol{k}}^{\lambda\lambda'} &= \sum_{\boldsymbol{G}} v_{\boldsymbol{G}} \int d\boldsymbol{x}\phi_{\lambda,\boldsymbol{k}}^*(\boldsymbol{x})e^{i\boldsymbol{G}\cdot\boldsymbol{x}}\phi_{\lambda',\boldsymbol{k}}(\boldsymbol{x}) \operatorname{Tr}[\delta\rho e^{-i\boldsymbol{G}\cdot\boldsymbol{x}}] \\ &= \sum_{\boldsymbol{G}} v_{\boldsymbol{G}} \left\langle \phi_{\lambda,\boldsymbol{k}} \right| e^{i\boldsymbol{G}\cdot\boldsymbol{x}} \left| \phi_{\lambda',\boldsymbol{k}} \right\rangle \operatorname{Tr}[\delta\rho e^{-i\boldsymbol{G}\cdot\boldsymbol{x}}] \\ &= \sum_{\boldsymbol{G}} v_{\boldsymbol{G}}\gamma_{\boldsymbol{k},\boldsymbol{k}}^{\lambda,\lambda'}(\boldsymbol{G}) \operatorname{Tr}[\delta\rho e^{-i\boldsymbol{G}\cdot\boldsymbol{x}}], \end{aligned} \tag{D.19}$$

and

$$\begin{aligned} v_{\mathrm{F}}[\delta\rho]_{\boldsymbol{k}}^{\lambda\lambda'} &= -\frac{1}{2}\sum_{\boldsymbol{G},\boldsymbol{q}} v_{\boldsymbol{G}+\boldsymbol{q}} \int d\boldsymbol{x} \int d\boldsymbol{x}'\phi_{\lambda,\boldsymbol{k}}^*(\boldsymbol{x})\delta\rho(\boldsymbol{x},\boldsymbol{x}')e^{i(\boldsymbol{G}+\boldsymbol{q})\cdot(\boldsymbol{x}-\boldsymbol{x}')}\phi_{\lambda',\boldsymbol{k}}(\boldsymbol{x}') \\ &= -\frac{1}{2}\sum_{\boldsymbol{G},\boldsymbol{q}} v_{\boldsymbol{G}+\boldsymbol{q}} \int d\boldsymbol{x} \int d\boldsymbol{x}'\phi_{\lambda,\boldsymbol{k}}^*(\boldsymbol{x}) \sum_{\mu\nu\boldsymbol{k}'} \phi_{\mu,\boldsymbol{k}'}(\boldsymbol{x})\delta\rho_{\boldsymbol{k}'}^{\mu\nu}\phi_{\nu,\boldsymbol{k}'}^*(\boldsymbol{x}')e^{i(\boldsymbol{G}+\boldsymbol{q})\cdot(\boldsymbol{x}-\boldsymbol{x}')}\phi_{\lambda',\boldsymbol{k}}(\boldsymbol{x}') \\ &= -\frac{1}{2}\sum_{\boldsymbol{G},\boldsymbol{q}} v_{\boldsymbol{G}+\boldsymbol{q}} \sum_{\mu\nu\boldsymbol{k}'} \delta\rho_{\boldsymbol{k}'}^{\mu\nu} \left\langle \phi_{\lambda,\boldsymbol{k}} \right| e^{i(\boldsymbol{G}+\boldsymbol{q})\cdot\boldsymbol{x}} \left| \phi_{\mu,\boldsymbol{k}'} \right\rangle \left\langle \phi_{\nu,\boldsymbol{k}'} \right| e^{-i(\boldsymbol{G}+\boldsymbol{q})\cdot\boldsymbol{x}} \left| \phi_{\lambda',\boldsymbol{k}} \right\rangle \\ &= -\frac{1}{2}\sum_{\boldsymbol{G},\boldsymbol{q}} v_{\boldsymbol{G}+\boldsymbol{q}} \sum_{\mu\nu} \delta\rho_{\boldsymbol{k}-\boldsymbol{q}}^{\mu\nu} \left\langle \phi_{\lambda,\boldsymbol{k}} \right| e^{i(\boldsymbol{G}+\boldsymbol{q})\cdot\boldsymbol{x}} \left| \phi_{\mu,\boldsymbol{k}-\boldsymbol{q}} \right\rangle \left\langle \phi_{\nu,\boldsymbol{k}-\boldsymbol{q}} \right| e^{-i(\boldsymbol{G}+\boldsymbol{q})\cdot\boldsymbol{x}} \left| \phi_{\lambda',\boldsymbol{k}} \right\rangle \\ &= -\frac{1}{2}\sum_{\boldsymbol{G},\boldsymbol{q}} v_{\boldsymbol{G}+\boldsymbol{q}} \sum_{\mu\nu} \delta\rho_{\boldsymbol{k}-\boldsymbol{q}}^{\mu\nu}\gamma_{\boldsymbol{k},\boldsymbol{k}-\boldsymbol{q}}^{\lambda,\mu}(\boldsymbol{G})\gamma_{\boldsymbol{k},\boldsymbol{k}-\boldsymbol{q}}^{\lambda',\nu}(\boldsymbol{G})^*, \end{aligned} \tag{D.20}$$

where the overlap factor $\gamma_{\boldsymbol{k},\boldsymbol{k}'}^{\lambda,\lambda'}(\boldsymbol{G})$ is given by

$$\gamma_{\boldsymbol{k},\boldsymbol{k}'}^{\lambda,\lambda'}(\boldsymbol{G}) = \left\langle \phi_{\lambda,\boldsymbol{k}} \right| e^{i\boldsymbol{G}\cdot\boldsymbol{x}}e^{i(\boldsymbol{k}-\boldsymbol{k}')\cdot\boldsymbol{x}} \left| \phi_{\lambda',\boldsymbol{k}'} \right\rangle = \left\langle u_{\lambda,\boldsymbol{k}} \right| e^{i\boldsymbol{G}\cdot\boldsymbol{x}} \left| u_{\lambda',\boldsymbol{k}'} \right\rangle. \tag{D.21}$$

We introduce two approximations to proceed the calculation. First, we ignore the Coulomb potential outside the BZ, i.e., we assume

$$v_{\boldsymbol{G}+\boldsymbol{q}} \approx 0 \quad (\boldsymbol{G} \neq 0). \tag{D.22}$$

Second, we assume a homogeneous system, which is equivalent to assuming that the lattice periodic part of the Bloch function is independent of $\boldsymbol{k}$:

$$\phi_{\lambda,\boldsymbol{k}} = e^{i\boldsymbol{k}\cdot\boldsymbol{x}}u_{\lambda,\boldsymbol{k}} \approx e^{i\boldsymbol{k}\cdot\boldsymbol{x}}u_{\lambda,0}. \tag{D.23}$$

This simplifies the overlap factor when $\boldsymbol{G} = 0$,

$$\gamma_{\boldsymbol{k},\boldsymbol{k}'}^{\lambda,\lambda}(\boldsymbol{G} = 0) = \langle u_{\lambda,\boldsymbol{k}} | u_{\lambda',\boldsymbol{k}'} \rangle \approx \delta_{\lambda\lambda'}. \tag{D.24}$$

Inserting Eqs. (D.22) and (D.24) leads to

$$v_{\mathrm{H}}[\delta\rho]_{\boldsymbol{k}}^{\lambda\lambda'} \approx v_{\boldsymbol{G}=0}\gamma_{\boldsymbol{k},\boldsymbol{k}}^{\lambda,\lambda'}(0) \operatorname{Tr}[\delta\rho] = 0, \tag{D.25}$$

because $\mathrm{Tr}[\delta\rho] = 0$, and

$$v_{\mathrm{F}}[\delta\rho]^{\lambda\lambda'}_{\boldsymbol{k}} \approx -\frac{1}{2}\sum_{\boldsymbol{q}} v_{\boldsymbol{q}} \sum_{\mu\nu} \delta\rho^{\mu\nu}_{\boldsymbol{k}-\boldsymbol{q}} \gamma^{\lambda,\mu}_{\boldsymbol{k},\boldsymbol{k}-\boldsymbol{q}}(0) \gamma^{\lambda',\nu}_{\boldsymbol{k},\boldsymbol{k}-\boldsymbol{q}}(0)^* \approx -\frac{1}{2}\sum_{\boldsymbol{q}} v_{\boldsymbol{q}} \delta\rho^{\lambda\lambda'}_{\boldsymbol{k}-\boldsymbol{q}}. \tag{D.26}$$

Therefore, if we adopt the approximations above, the matrix element of the interelectronic operator $w[\delta\rho]^{\lambda\lambda'}_{\boldsymbol{k}}$ is given by

$$w[\delta\rho]^{\lambda\lambda'}_{\boldsymbol{k}} \approx -\frac{1}{2}\sum_{\boldsymbol{q}} v_{\boldsymbol{q}} \delta\rho^{\lambda\lambda'}_{\boldsymbol{k}-\boldsymbol{q}} \tag{D.27}$$

Inserting Eq.(D.18) into Eq. (D.17) yields

$$\begin{aligned} i\frac{\partial}{\partial t}\rho^{\lambda\lambda'}_{\boldsymbol{k}} = (\tilde{\varepsilon}_{\lambda,\boldsymbol{k}} - \tilde{\varepsilon}_{\lambda',\boldsymbol{k}})\rho^{\lambda\lambda'}_{\boldsymbol{k}} + (\rho^{\lambda'\lambda'}_{\boldsymbol{k}} - \rho^{\lambda\lambda}_{\boldsymbol{k}})\Omega^{\lambda\lambda'}_{\boldsymbol{k}} \\ + \sum_{\mu\neq\lambda,\lambda'} (\Omega^{\lambda\mu}_{\boldsymbol{k}}\rho^{\mu\lambda}_{\boldsymbol{k}} - \rho^{\lambda\mu}_{\boldsymbol{k}}\Omega^{\mu\lambda'}_{\boldsymbol{k}}), \end{aligned} \tag{D.28}$$

where we define the renormalized single-particle energy

$$\tilde{\varepsilon}_{\lambda,\boldsymbol{k}} = \varepsilon_{\lambda,\boldsymbol{k}} + (v_{\mathrm{l-m}})^{\lambda\lambda}_{\boldsymbol{k}} + w[\delta\rho]^{\lambda\lambda}_{\boldsymbol{k}}, \tag{D.29}$$

and the renormalized Rabi frequency

$$\Omega^{\lambda\lambda'}_{\boldsymbol{k}} = (v_{\mathrm{l-m}})^{\lambda\lambda'}_{\boldsymbol{k}} + w[\delta\rho]^{\lambda\lambda'}_{\boldsymbol{k}}. \tag{D.30}$$

Equation (D.28) is equivalent to the multi-band SBE,

$$\begin{aligned} i\frac{\partial}{\partial t}p^{\lambda\lambda'}_{\boldsymbol{k}} &= (\tilde{\varepsilon}_{\lambda,\boldsymbol{k}} - \tilde{\varepsilon}_{\lambda',\boldsymbol{k}})p^{\lambda\lambda'}_{\boldsymbol{k}} \\ &\quad + \Omega^{\lambda\lambda'}_{\boldsymbol{k}}(f^{\lambda}_{\boldsymbol{k}} - f^{\lambda'}_{\boldsymbol{k}}) + \sum_{\mu\neq\lambda,\lambda'} (p^{\lambda\mu}_{\boldsymbol{k}}\Omega^{\mu\lambda'}_{\boldsymbol{k}} - \Omega^{\lambda\mu}_{\boldsymbol{k}}p^{\mu\lambda'}_{\boldsymbol{k}}) \end{aligned} \tag{D.31}$$

$$i\frac{\partial}{\partial t}f^{\lambda}_{\boldsymbol{k}} = -\sum_{\mu\neq\lambda}(\Omega^{\lambda\mu}_{\boldsymbol{k}}p^{\mu\lambda}_{\boldsymbol{k}} - p^{\lambda\mu}_{\boldsymbol{k}}\Omega^{\mu\lambda}_{\boldsymbol{k}}). \tag{D.32}$$

E

Current Density from Nonlocal Exchange Operator in Frozen TDHF

Here I derive the current density Eq. (5.26) from the nonlocal exchange operator $v_{\mathrm{x},A(t)}[\rho_0]$ generated from the static ground state in the frozen TDHF theory. According to Eq. (2.50), the additional current density from a nonlocal operator v_{nl} is given by

$$j_{nl}(t) = \frac{1}{N_k a}\frac{1}{i}\left\langle [x, v_{\mathrm{nl}}] \right\rangle, \tag{E.1}$$

where $[\cdot,\cdot]$ denotes the commutator. Thus, the contribution from $v_{\mathrm{x},A(t)}[\rho_0]$ is given by

$$\begin{aligned} j_{\mathrm{nl}}(t) &= \frac{1}{N_k a}\frac{2}{i}\sum_{b,k_0}\left\langle \psi^f_{b,k_0}(t)\right| \left[x, v_{\mathrm{x},A(t)}[\rho_0]\right] \left|\psi^f_{b,k_0}(t)\right\rangle && \text{(E.2)}\\ &= \frac{1}{N_k a}\frac{2}{i}\sum_{b,k_0}\int dx \int dx' \psi^{f*}_{b,k_0}(x,t)\left(x v_{\mathrm{x},A(t)}[\rho_0](x,x') - v_{\mathrm{x},A(t)}[\rho_0](x,x')x'\right)\psi^f_{b,k_0}(x',t) && \text{(E.3)}\\ &= \frac{4}{N_k a}\sum_{b,k_0}\mathrm{Im}\left[\int dx \int dx' \psi^{f*}_{b,k_0}(x,t) x v_{\mathrm{x},A(t)}[\rho_0](x,x')\psi^f_{b,k_0}(x',t)\right], && \text{(E.4)} \end{aligned}$$

where $\psi^f_{b,k}(x,t) = \frac{1}{N_k}e^{ikx}u^f_{b,k}(x,t)$ is time-dependent orbitals under the frozen TDHF Hamiltonian. We decompose the orbitals into the plain wave and lattice periodic parts, and split the integral into each of the unit cells,

$$\begin{aligned} j_{\mathrm{nl}}(t) &= \frac{4}{N_k a}\sum_{b,k_0}\frac{1}{N_k}\mathrm{Im}\left[\int dx \int dx' u^{f*}_{b,k_0}(x,t) x e^{-ik_0 x} v_{\mathrm{x},A(t)}[\rho_0](x,x') e^{ik_0 x'} u^f_{b,k_0}(x',t)\right] && \text{(E.5)}\\ &= \frac{4}{N_k a}\sum_{b,k_0}\frac{1}{N_k}\mathrm{Im}\Bigg[\sum_T \int_\Omega dx u^{f*}_{b,k_0}(x+T,t)(x+T)\\ &\quad \times \sum_{T'}\int_\Omega dx' e^{-ik_0(x+T)} v_{\mathrm{x},A(t)}[\rho_0](x+T,x'+T') e^{ik_0(x'+T')} u^f_{b,k_0}(x'+T',t)\Bigg]. && \text{(E.6)} \end{aligned}$$

Let us take $T' \to T + T'$ using the periodic boundary conditions. Using the fact that

$$v_{\mathrm{x},A(t)}[\rho_0](x+T,x'+T) = v_{\mathrm{x},A(t)}[\rho_0](x,x'), \tag{E.7}$$

Equation (E.6) is transformed into

$$j_{\mathrm{nl}}(t) = \frac{4}{N_k a}\sum_{b,k_0}\frac{1}{N_k}\mathrm{Im}\Bigg[\sum_{T}\int_{\Omega} dx u^{f*}_{b,k_0}(x+T,t)(x+T) \sum_{T'}\int_{\Omega} dx' e^{-ik_0 x} v_{\mathrm{x},A(t)}[\rho_0](x,x'+T')e^{ik_0(x'+T')}u^{f}_{b,k_0}(x'+T',t)\Bigg] \tag{E.8}$$

$$= \frac{4}{N_k a}\sum_{b,k_0}\frac{1}{N_k}\mathrm{Im}\left[\sum_{T}\int_{\Omega} dx u^{f*}_{b,k_0}(x,t)(x+T)\int_{\Omega} dx' v^{\Omega}_{\mathrm{x},k_0+A(t)}[\rho_0](x,x')u^{f}_{b,k_0}(x',t)\right], \tag{E.9}$$

where $v^{\Omega}_{\mathrm{x},k}[\rho]$ is defined by Eq. (2.38),

$$v^{\Omega}_{\mathrm{x},k}[\rho(t)](x,x') = \sum_{T} e^{-ik\cdot x} v_{\mathrm{x}}(x,x'+T)e^{ik\cdot(x'+T)}. \tag{E.10}$$

As the term proportional to T in the right-hand side of Eq. (E.9) is canceled out by the counterpart with opposite sign, we have

$$j_{\mathrm{nl}}(t) = \frac{4}{N_k a}\sum_{b,k_0}\frac{1}{N_k}\mathrm{Im}\left[\sum_{T}\int_{\Omega} dx u^{f*}_{b,k_0}(x,t)x\int_{\Omega} dx' v^{\Omega}_{\mathrm{x},k_0+A(t)}[\rho_0](x,x')u^{f}_{b,k_0}(x',t)\right] \tag{E.11}$$

$$= \frac{4}{N_k a}\sum_{b,k_0}\mathrm{Im}\left[\int_{\Omega} dx u^{f*}_{b,k_0}(x,t)x\int_{\Omega} dx' v^{\Omega}_{\mathrm{x},k_0+A(t)}[\rho_0](x,x')u^{f}_{b,k_0}(x',t)\right], \tag{E.12}$$

the current density from the frozen exchange operator, given by Eq. (5.26).

F

TDHF Equation in Houston Basis

Here, we discuss general representation of TDHF equations in Houston basis. We expand the time-dependent orbital functions $\psi_{b,k_0}(x,t)$ with Houston states $\tilde{\phi}_{\lambda,k_0}(x,t) = e^{-iA(t)x}\phi_{\lambda,k(t)}(x)$ as

$$\psi_{b,k_0}(x,t) = \sum_{\mu} \alpha^{\mu}_{b,k_0}(t) e^{-i\int_0^t \varepsilon_{\mu,k(t')}dt'} \tilde{\phi}_{\mu,k_0}(x,t), \tag{F.1}$$

where $k(t) = k_0 + A(t)$. Substituting Eq. (F.1) into Eq. (5.18) yields the coupled equations for complex amplitudes $\alpha^{\lambda}_{bk_0}(t)$,

$$i\frac{d}{dt}\alpha^{\lambda}_{b,k_0}(t) = \sum_{\mu} \alpha^{\mu}_{b,k_0}(t) e^{i\int_0^t \Delta\varepsilon_{\lambda\mu}[k(t')]dt'} \left(\xi^{\lambda\mu}_{k(t)}\mathcal{E}(t) + \langle\tilde{\phi}_{\lambda,k_0}(t)|\,\hat{w}[\delta\rho(t)]\,|\tilde{\phi}_{\mu,k_0}(t)\rangle\right), \tag{F.2}$$

where $\xi^{\lambda\lambda'}_{k(t)} = i\,\langle u^0_{\lambda,k(t)}|\nabla_k u^0_{\lambda',k(t)}\rangle$.

The interelectronic operator $\hat{w}[\delta\rho(t)]$ is composed of the Coulomb and the exchange operator,

$$\begin{aligned}&\langle\tilde{\phi}_{\lambda,k_0}(t)|\,\hat{w}[\delta\rho(t)]\,|\tilde{\phi}_{\mu,k_0}(t)\rangle \\ &\quad= \langle\tilde{\phi}_{\lambda,k_0}(t)|\,\hat{v}_{\mathrm{C}}[\delta\rho(t)]\,|\tilde{\phi}_{\mu,k_0}(t)\rangle + \langle\tilde{\phi}_{\lambda,k_0}(t)|\,\hat{v}_{\mathrm{x}}[\delta\rho(t)]\,|\tilde{\phi}_{\mu,k_0}(t)\rangle\,.\end{aligned} \tag{F.3}$$

The Coulomb matrix element is given by

$$\begin{aligned}&\langle\tilde{\phi}_{\lambda,k_0}(t)|\,\hat{v}_{\mathrm{C}}[\delta\rho(t)]\,|\tilde{\phi}_{\mu,k_0}(t)\rangle \\ &= \sum_{G\neq 0} v_G\,\langle\tilde{\phi}_{\lambda,k_0}(t)|\,e^{iGx}\,|\tilde{\phi}_{\mu,k_0}(t)\rangle\int dx'\delta\rho(x',x',t)e^{-iGx'}, \\ &= 2\sum_{G\neq 0} v_G\gamma^{\lambda,\mu}_{k(t),k(t)}(G)\sum_{b',k'_0}\left(\sum_{\nu\eta} D^{\nu\eta}_{b',k'_0}(t)\gamma^{\eta,\nu}_{k'(t),k'(t)}(-G) - \gamma^{b',b'}_{k'(t),k'(t)}(-G)\right),\end{aligned} \tag{F.4}$$

where we define

$$\gamma^{\lambda,\lambda'}_{k,k'}(G) = \langle u^0_{\lambda,k}|\,e^{iGx}\,|u^0_{\lambda',k'}\rangle\,, \tag{F.5}$$

and

$$D^{\lambda\lambda'}_{b,k_0}(t) = \alpha^{lambda}_{b,k_0}(t)\alpha^{\lambda'*}_{b,k_0}(t)e^{-i\int_0^t \Delta\varepsilon_{\lambda\lambda'}[k(t')]dt'}. \tag{F.6}$$

v_k is the spatial Fourier component of interelectronic Coulomb potential,

$$v(x-x') = \sum_{G,q} v_{G+q}e^{i(G+q)(x-x')}. \tag{F.7}$$

The exchange matrix element is given by

$$\begin{aligned}
&\langle\tilde{\phi}_{\lambda,k_0}(t)|\,\hat{v}_{\mathrm{x}}[\delta\rho(t)]\,|\tilde{\phi}_{\mu,k_0}(t)\rangle \\
&= -\frac{1}{2}\sum_{G,q} v_{G+q}\iint dxdx'\tilde{\phi}^{*}_{\lambda,k_0}(x)\delta\rho(x,x')e^{i(G+q)(x-x')}\tilde{\phi}_{\mu,k_0}(x') \\
&= -\sum_{G}\sum_{b',k_0'} v_{G+k_0-k_0'}\left(\sum_{\nu\eta} D^{\nu\eta}_{b',k_0'}(t)\gamma^{\lambda,\nu}_{k(t),k'(t)}(G)\gamma^{\eta,\mu}_{k'(t),k(t)}(-G) - \gamma^{\lambda,b'}_{k(t),k'(t)}(G)\gamma^{b',\mu}_{k'(t),k(t)}(-G)\right). \quad \text{(F.8)}
\end{aligned}$$

Finally, substituting Eqs. (F.4) and (F.8) into Eq. (F.2) yields

$$\begin{aligned}
i\frac{d}{dt}\alpha^{\lambda}_{b,k_0}(t) = \sum_{\mu}\alpha^{\mu}_{b,k_0}(t)e^{i\int_0^t \Delta\varepsilon_{\lambda\mu}[k(t')]dt'}\Bigg[&\xi^{\lambda\mu}_{k(t)}\mathcal{E}(t) \\
&+ 2\sum_{G\neq 0} v_G\gamma^{\lambda,\mu}_{k(t),k(t)}(G)\sum_{b',k_0'}\left(\sum_{\nu\eta} D^{\nu\eta}_{b',k_0'}(t)\gamma^{\eta,\nu}_{k'(t),k'(t)}(-G) - \gamma^{b',b'}_{k'(t),k'(t)}(-G)\right) \\
&- \sum_{G}\sum_{b',k_0'} v_{G+k_0-k_0'}\left(\sum_{\nu\eta} D^{\nu\eta}_{b',k_0'}(t)\gamma^{\lambda,\nu}_{k(t),k'(t)}(G)\gamma^{\eta,\mu}_{k'(t),k(t)}(-G) - \gamma^{\lambda,b'}_{k(t),k'(t)}(G)\gamma^{b',\mu}_{k'(t),k(t)}(-G)\right)\Bigg]. \quad \text{(F.9)}
\end{aligned}$$

This is the most general form of TDHF equation in the Houston basis.